University of Tennessee, Knoxville

TRACE: Tennessee Research and Creative Exchange

Doctoral Dissertations

Graduate School

5-2008

Imaging by Detection of Infrared Photons Using Arrays of Uncooled Micromechanical Detectors

Dragoslav Grbovic
University of Tennessee - Knoxville

Follow this and additional works at: https://trace.tennessee.edu/utk_graddiss

Part of the Physics Commons

Recommended Citation

Grbovic, Dragoslav, "Imaging by Detection of Infrared Photons Using Arrays of Uncooled Micromechanical Detectors. " PhD diss., University of Tennessee, 2008.
https://trace.tennessee.edu/utk_graddiss/404

This Dissertation is brought to you for free and open access by the Graduate School at TRACE: Tennessee Research and Creative Exchange. It has been accepted for inclusion in Doctoral Dissertations by an authorized administrator of TRACE: Tennessee Research and Creative Exchange. For more information, please contact trace@utk.edu.

To the Graduate Council:

I am submitting herewith a dissertation written by Dragoslav Grbovic entitled "Imaging by Detection of Infrared Photons Using Arrays of Uncooled Micromechanical Detectors." I have examined the final electronic copy of this dissertation for form and content and recommend that it be accepted in partial fulfillment of the requirements for the degree of Doctor of Philosophy, with a major in Physics.

Hanno H. Weitering, Major Professor

We have read this dissertation and recommend its acceptance:

Panos G. Datskos, Adolfo G. Eguiluz, Adriana Moreo, Michael J. Sepaniak

Accepted for the Council:

Carolyn R. Hodges

Vice Provost and Dean of the Graduate School

(Original signatures are on file with official student records.)

To the Graduate Council:

I am submitting herewith a dissertation written by Dragoslav Grbovic entitled "Imaging by Detection of Infrared Photons Using Arrays of Uncooled Micromechanical Detectors." I have examined the final electronic copy of this dissertation for form and content and recommend that it be accepted in partial fulfillment of the requirements for the degree of Doctor of Philosophy, with a major in Physics.

Hanno H. Weitering

Major Professor

We have read this thesis
and recommend its acceptance:

Panos G. Datskos

Adolfo G. Eguiluz

Adriana Moreo

Michael J. Sepaniak

Accepted for the Council:

Carolyn R. Hodges

Vice Provost and
Dean of the Graduate School

(Original signatures are on file with official student records.)

Imaging by Detection of Infrared Photons Using Arrays of Uncooled Micromechanical Detectors

A Dissertation
Presented for the
Doctor of Philosophy
Degree
The University of Tennessee Knoxville

Dragoslav Grbovic
May 2008

Dedication

This dissertation is dedicated to Dragica and Milan Grbović for giving me the gift of life and being the source of limitless inspiration.

Acknowledgments

I am very fortunate that the list of people who I believe took part in my obtaining a Ph.D. is quite long.

I would like to thank Dr. Panos Datskos, my research advisor, for providing me with resources necessary to carry out this work as well as academic and personal guidance and support from the time I first met him as an undergraduate summer intern. I would also like to thank Nickolay Lavrik and Slobodan Rajić, members of the group at Oak Ridge National Laboratory where I carried all of my graduate research. They were the unlimited source of information necessary to carry out day-to-day tasks and I thank them for immeasurable patience with me many of my questions. Many thanks go to wonderful faculty and staff at the Department of Physics and Astronomy of University of Tennessee in Knoxville, especially the members of my Ph.D. committee, Hanno Weitering, Adolfo Eguiluz, Adriana Moreo and Michael Sepaniak.

I would like to thank staff at Cornell NanoScale Science and Technology Facility at Cornell University in Ithaca, NY where a part of my research has been carried out. Their help was of great importance for the completion of my dissertation.

It would be unfair not to thank faculty at Ramapo College of New Jersey, where I obtained my bachelor's degree in physics, for igniting the interest in physics and providing necessary encouragement for pursuing a graduate degree: Dr. Teodoro Halpern, for "tricking" me into taking physics as a major and, for the first time in my life, presenting physics in such a way that I was not afraid of it; Dr. Daniela Buna, for being persistent in emphasizing the importance of undergraduate research and providing the necessary help and encouragement for securing an undergraduate summer internship at University of Tennessee and Dr. Philip Anderson, for showing me how interesting and rewarding the applied physics can be.

The degree also came with a priceless perk. During my time in Knoxville, I have met wonderful people and made lifelong friends. I am so grateful that Whinkey and Jovan Ilic, Lana and Zoran Zivanovic, Maria Bezzhon and Irakli Garishvili, Doddie and Donny Hornbac, Maria Orechkina, Carrie Morris and Predrag Klašnja, Meagan Ayer and Paul Deiana Molnar and Maria and Fr. Michael Platanis are among those friends. There were there to share both joy and sorrow and made Knoxville feel like a second home.

However, the challenges of obtaining the Ph.D. and reaching the stage of graduate studies would be insurmountable without the support of family. My parents, Dragica and Milan Grbović, unfortunately did not live to share the joy of completion of my studies but were present in my hart every single day. I have been blessed with such amazing parents

who have provided me with guidance and great strength and keep doing so. I thank Mladen Grbović for being the best brother and keeping up with me all these years. I would also like to thank my stepmother Nada Filipović for being like a mother to us.

I thank my son, Milan Grbović, for unlimited smiles and making all the sacrifices worthwhile. I thank him for being an incredible baby, considerate and, with help from his grandparents, kind to allow his mom and dad to finish their studies. I thank Milan's grandparents, Divna and Dragan Pješivac and Nada Filipović for their support and help in raising Milan, as well as my brothers-in-law, Raško and Vlado Pješivac.

The greatest gratitude goes to Jelena Pjesivac-Grbović, my wife, for her endless support and inspiration she has provided. Her belief in me, stronger then my own, has kept me going. By her own example of tremendous courage, strength and unconditional love, she would dismiss any of my doubts, and for that I thank her deeply.

Finally, I am thankful to our Holy Father for giving me the opportunity and providing the necessary support to carry out this important task in my life.

Abstract

The objective of this dissertation was to investigate the possibility of uncooled infrared imaging using arrays of optically-probed micromechanical detectors. This approach offered simplified design, improved reliability and lower cost, while attaining the performance approaching that contemporary uncooled imagers. Micromechanical infrared detectors undergo deformation due to the bimetallic effect when they absorb infrared photons. The performance improvements were sought through changes in structural design such as modification and simplification of detector geometry as well as changes in the choice of materials. Detector arrays were designed, fabricated and subsequently integrated into the imaging system and relevant parameters, describing the sensitivity and signal-to-noise ratio, were characterized. The values of these parameters were compared to values published for other uncooled micromechanical detectors and commercial uncooled detectors. Several designs have been investigated. The first design was made of standard materials for this type of detectors - silicon nitride and gold. The design utilized changes in detector geometry such as reduction in size and featured an optical resonant cavity between the detector and the substrate on which arrays were built. This design provided decrease in levels of noise equivalent temperature difference (*NETD*) to as low as 500 mK. The *NETD* parameter limits the lowest temperature gradient on the imaged object that can be resolved by the imaging device. The second design used silicon dioxide and aluminum, materials not yet fully investigated. It featured a removed substrate beneath each detector in the array, to allow unobstructed transmission of incoming IR radiation and improve the thermal isolation of the detector. Second design also featured an amorphous silicon layer between silicon dioxide and aluminum layers, to serve as an optical resonant cavity. The *NETD* levels as low as 120 mK have been achieved. The only difference between the third and the second design was the modification of the geometry to minimize the noise. Successfully obtained thermal images and improved *NETD* values, approaching those of modern uncooled imagers (20 mK for commercial bolometer-based detectors), confirm the viability of this approach. With further improvements, this approach has a potential of becoming a low-cost alternative for uncooled infrared imaging.

Contents

Chapter Page

Chapter 1 ... 1
Introduction ... 1
1.1 Infrared Radiation ... 1
1.2 Infrared Detectors ... 2
1.3 Applications ... 3
1.4 Basic Principles ... 4
1.5 Transduction Mechanisms for Micromechanical Detectors ... 5
Chapter 2 ... 9
Figures of Merit ... 9
2.1 Responsivity ... 10
2.2 Noise Equivalent Power ... 11
2.3 Normalized Detectivity ... 11
2.4 Noise Equivalent Temperature Difference ... 12
2.5 Response Time ... 13
Chapter 3 ... 15
Theoretical Background for Micromechanical Infrared Detectors ... 15
3.1 Bimetallic Effect ... 16
3.2 Thermal Conductance ... 18
3.3 Microcantilever Responsivity ... 20
Chapter 4 ... 25
Noise Sources and Fundamental Limits They Impose ... 25
4.1 Temperature Fluctuation Noise ... 26
4.2 Background Fluctuation Noise ... 32
4.3 Thermo-Mechanical Noise ... 33
4.4 Readout Noise ... 37
4.4.1 Piezoresistive Readout ... 37
4.4.2 Capacitive Readout ... 40
4.4.3 Optical Readout ... 40
4.5 Total Noise ... 43
4.6 Summary ... 43
Chapter 5 ... 46
State of the Art ... 46

Chapter 6 55
Demonstration of Imaging System Using Optically-Probed Micromechanical Infrared Detectors 55
6.1 Fabrication 56
Comparison of the Model and Experimental Results 58
6.2 System Integration 61
Chapter 7 66
Design and Characterization of SiO_2 Substrate-Free Detector Arrays for IR and THz Imaging 66
7.1 Model 67
7.2 Implementation 73
7.3 Experiment and Results 75
7.4 Summary 83
Chapter 8 85
Implementation of SiO_2Substrate-Free Detector Arrays Featuring Built-In Optical Cavity for Enhanced Absorption of IR and THz Radiation 85
8.1 Model 85
8.1.1 Deformation-Magnification Detector 85
8.1.2 Self Leveling Detectors 92
8.1.3 Comparison of Two Designs 101
8.2 Implementation 102
8.3 Experiment and Results 105
8.4 Summary 111
Chapter 9 113
Implementation and Characterization of Integrated Imaging System 113
9.1 Imaging Using Arrays of Deformation-Magnification Structures 115
9.2 Imaging Using Arrays of Self-Leveling Structures 121
9.3 Summary 125
Chapter 10 127
Conclusion 127
Bibliography 130
Appendix 137
Appendix 138
Calculation of Δz for Multifold Infrared Detectors 138
Vita 141

List of Figures

Figure Page

Figure 1 Blackbody Radiation Distribution..2
Figure 2 Conceptual illustration of the main parts of an infrared detector..........................5
Figure 3 Illustration of an optical readout configuration...7
Figure 4 Illustration of the optically-probed array of micromechanical uncooled infrared detectors 8
Figure 5 Illustration of a micromechanical, infrared detector. 16
Figure 6 Deformation of the bimaterial structure due to temperature increase 17
Figure 7 Plots of calculated thermal conductances versus the length of thermal isolation region 19
Figure 8 Frequency spectrum of the detector discussed in [14]. 21
Figure 9 Measured response of a SiN_x detector discussed in [14]. 23
Figure 10 Spectral density of temperature fluctuation noise (rms values of temperature fluctuation)..27
Figure 11 Spectral densities of temperature-fluctuation and thermomechanical noise.....29
Figure 12 Temperature-fluctuation-noise-limited normalized detectivity D^* [54]...........30
Figure 13 Noise Equivalent Temperature Difference vs. thermal conductance [14] 31
Figure 14 Illustration of piezoresistive IR detector 38
Figure 15 Readout noise spectrum for piezoresistive cantilevers 39
Figure 16 Detector designed by Nikon 47
Figure 17 IR image reported by Nikon [30] 47
Figure 18 Bimaterial detector with comb-like structure 49
Figure 19 IR image reported by Zhao et al. [31] 49
Figure 20 Capacitive detector designed by Multispectral 50
Figure 21 Pneumatic Detector 50
Figure 22 Quartz-resonator IR detectors 51
Figure 23 Illustration of regular IR detector vs. substrate-free detector............................52
Figure 24 IR image reported by Guo et al. [50] 53
Figure 25 Illustration of SiN_x detector...56
Figure 26 Ion Micrograph of the portion of the fabricated 256×256 MEMS FPA 57
Figure 27 Microfabrication steps..58
Figure 28 Frequency spectrum of the micromechanical IR detector structures 59

Figure 29 Response of the SiN_x detector to laser excitation 60
Figure 30 Schematic illustration and photograph of components and arrangement used in the implemented prototype of a MEMS IR imager 62
Figure 31 Optical configuration of the integrated system 64
Figure 32 Two histograms of the pixels displaying targets with recorded backgrounds at different temperatures 64
Figure 33 Infrared images of human faces obtained using SiN_x detectors 65
Figure 34 Illustration of the geometry of the substrate-free detector design 69
Figure 35 Illustration of addition of individual bimaterial region's deformation angles for deformation-magnification structure 69
Figure 36 Illustration of the deformations of the structure in each of the first 6 modes of oscillation 70
Figure 37 Thermal analysis of substrate-free detectors 70
Figure 38 Process flow for the completely dry microfabrication of substrate-free detector arrays 74
Figure 39 Microscope photographs taken after microfabrication steps 76
Figure 40 Photograph of a completed wafer of substrate-free detector arrays 77
Figure 41 Microscope photograph and ion micrographs of completed SiO_2 substrate-free detector arrays 78
Figure 42 Schematic representation of the characterization system configuration 79
Figure 43 Frequency spectra of substrate-free detectors 80
Figure 44 Thermal response times for substrate-free detectors 82
Figure 45 Detector response to laser actuation with detector at atmospheric pressure 82
Figure 46 Thermal response times vs. pressure 83
Figure 47 Illustration of geometry of the deformation magnification, substrate-free design with built-in optical cavity 87
Figure 48 The reflection spectra calculated using generalied Rouard method[99] 88
Figure 49 Deformation of the deformation-magnification structure in each of the first 6 modes of oscillation 89
Figure 50 Thermal analyis of deformation-magnification detectors 90
Figure 51 Illustration of geometry of the substrate-free, self-leveling design with built-in optical cavity 93
Figure 52 Illustration of addition of individual bimaterial region's deformation angles for self-leveling structure 94
Figure 53 Deformations of the structure in each of the first 6 modes of oscillation for the self-leveling detector 96
Figure 54 Thermal analysis for a self-leveling detector 97
Figure 55 Comparison of responses of two detectors due to ambient temperature increase 100
Figure 56 Comparison of responses of two detectors due to absorber temperature increase 100
Figure 57 Process flow for completely dry microfabrication process of substrate-free detector arrays featuring built-in optical cavity 103
Figure 58 Microscope photographs obtained after microfabrication steps 104
Figure 59 Microscope photographs of released detectors 106

Figure 60 Ion micrograph at several magnifications showing the fabricated focal plane arrays....107
Figure 61 Frequency spectra of arrays of substrate-free detectors with optical cavity ...109
Figure 62 Thermal response times....110
Figure 63 Illustration of FPA angle adjustment 114
Figure 64 Thermal images of human hand and head with sun-glasses obtained using array of SiO_2 deformation-magnification detectors....115
Figure 65 Illustration of resistive heater used for parameter-measurements....117
Figure 66 NETD histograms for the array of SiO_2 deformation-magnification detectors measured at two different temperatures....118
Figure 67 Average light intensity versus temperature for CCD pixels corresponding to a single SiO_2 deformation-magnification detector 119
Figure 68 Thermal image of a soldering iron recorded with SiO_2 deformation-magnification FPA at atmospheric pressure....120
Figure 69 Thermal images of human hand and head with sun-glasses obtained using array of SiO_2 deformation-magnification detectors....122
Figure 70 NETD histograms for the array of SiO_2 self-leveling detectors measured at two different temperatures....123
Figure 71 Average light intensity versus temperature for CCD pixels corresponding to a single SiO_2 self-leveling detector 124
Figure 72 Thermal image of a soldering iron taken with deformation-magnification FPA at atmospheric pressure....126
Figure 73 Angles associated with bimaterial cantilever deformations....138
Figure 74 Deformation angles for multifold structure....139

List of Tables

Table Page

Table 1 Material properties....................18
Table 2 Mechanical parameters for micromechanical infrared detector 28
Table 3 Reported geometries and parameters for some micromechanical IR detectors currently in use 53
Table 4 Modeled resonant modes of the deformation-magnification structure....................68
Table 5 Summary and comparison of finite element model and experimental results for substrate-free deformation-magnification structure 84
Table 6 Modeled resonant modes of deformation-magnification structure with cavity....90
Table 7 Modeled resonant modes of the self-leveling structure with cavity....................95
Table 8 Summary and comparison of finite element model and experimental results for deformation-magnification and self-leveling structures with cavities 112
Table 9 Comparisson of experimentally evaluated parameters for detector alone and detector in the integrated system 125

Chapter 1

Introduction

1.1 Infrared Radiation

Infrared radiation (IR) is electromagnetic radiation with wavelengths between 0.7 μm and 100 μm. It extends from visible light to THz waves. Because fundamentally different phenomena can be observed within the IR region, four sub-bands are usually distinguished: near-IR (NIR), midwave-IR (MWIR), longwave-IR (LWIR) and very longwave-IR (VLWIR). Although somewhat different definitions exist in literature, wavelengths from 0.7 μm to 2.5 μm belong to NIR, from 2.5 μm to 8 μm belong to MWIR, from 8 μm to 14 μm belong to LWIR and wavelengths above 14 μm belong to VLWIR. The IR photon energies range from 1.77 eV for 0.7 μm photons to 0.0124 eV for the 100 μm photons.

Significance and practical applications of IR detectors are related to two distinct phenomena: emission of electromagnetic waves by all objects at T > 0 K and interaction of electromagnetic waves with vibrational modes of molecular bonds. Thermal imaging and molecular spectroscopy are, respectively, the two major fields that critically depend on the ability to detect the IR radiation.

According to the blackbody radiation principle, every object with non-zero temperature emits radiation composed of infrared photons of various wavelengths. The photon distribution by wavelength depends on object temperature. The distribution of photons emitted by a blackbody with respect to their wavelength is governed by the Planck Radiation Formula [1]:

$$u(\lambda)=\frac{8\pi ch}{\lambda^5}\frac{1}{e^{ch/\lambda k_B T}-1} \tag{1}$$

where $u(\lambda)d\lambda$ is the volume density within the spectral region between λ and $\lambda + d\lambda$ of photons of a given wavelength λ, k_B is Boltzmann's constant and T is the temperature of object emitting the radiation. As can be seen in Figure 1, each distribution curve has a peak. This means that for each temperature, photons of certain wavelength dominate the distribution. The wavelength of dominant photons is given by the Vien's law:

$$\lambda = \frac{2.9mm}{T(K)} \tag{2}$$

According to Equation 2, majority of photons emitted by objects near room temperature have wavelengths between 8 and 14 μm (300K distribution curve in Figure 1). Blackbody radiation principle allows detection and imaging objects by just receiving radiation they emit without requiring external illumination.

1.2 Infrared Detectors

Detection of infrared (IR) radiation is very important for a variety of activities in both commercial and defense areas. Infrared detectors are transducers which absorb IR radiation and produce a measurable output proportional to the absorbed energy. Low atmospheric absorption of photons with wavelengths in bands from 3 to 5 μm and 8 to 14 μm makes those bands particularly important [2, 3]. However, the high cost of IR detectors has limited their present use to primarily military applications. Recent advances in uncooled thermal detectors will make a number of commercial applications possible[4]. Infrared radiation detectors[5, 6] can be classified broadly as either quantum (electro-optic)[7] or thermal detectors, such as pyroelectric[8], thermoelectric and thermoresistive transducers (bolometers)[9-13], and microcantilever thermal detectors[3, 14-26].

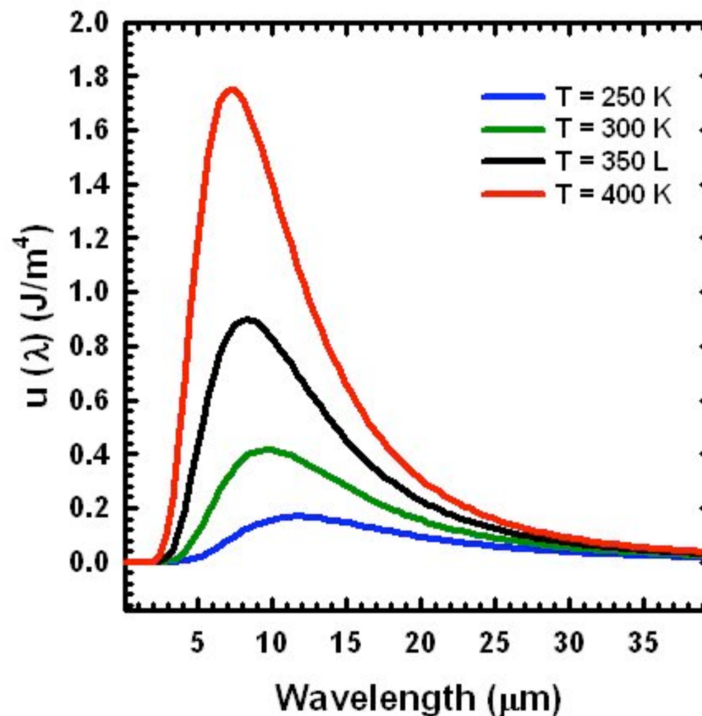

Figure 1 Blackbody Radiation Distribution
Distribution of energy density emitted by a blackbody at different temperatures

Quantum IR detectors are based on semiconductor materials with narrow bandgaps, $\varepsilon_g < hc/\lambda$ or metal–semiconductor structures (Schottky barriers) with appropriately small energy barriers, $\Delta\varepsilon < hc/\lambda$. One of the drawbacks of these detectors is that they have a cutoff wavelength above which they can not detect photons as those photons are unable to overcome the energy barrier. In addition the dark current, which contributes to the noise in these detectors, depends exponentially on temperature due to thermally generated charge carriers. This necessitates cooling of quantum IR detectors. The thermal resolution of cooled quantum IR detectors, however, can be very high, typically in the few mK range. On the other hand, thermal IR detectors are based on measuring the amount of heat produced in the detector upon the absorption of IR radiation and can operate at, or even above, room temperatures since thermal noise in thermal detectors varies as $\sqrt{T}$ [10, 27]. Since they can operate at or even slightly above room temperature they are often referred to as uncooled IR detectors.

The first type of uncooled IR detector was the bolometer. It converts the energy of incoming photons into heat, which in turn induces the change in the electrical resistance of the detector. A more recent type of uncooled IR detectors is a micromechanical transducer, which converts the energy of incoming photons into mechanical deformations by utilizing thermally sensitive bimaterial structures. This type of detector has emerged with advancements in micro-electromechanical systems (MEMS). Often, in literature, these detectors are referred to as MEMS uncooled detectors.

Individually fabricated IR detectors are used to measure IR radiation intensity and commonly referred to as spot detectors. Spot detectors are used primarily in infrared spectroscopy applications. Although spot detectors can be combined with scanning optical components in order to accomplish IR imaging [24], focal plane arrays (FPA) of IR detectors are increasingly the predominant type of IR detectors for imaging applications. One of the main advantages of micromechanical IR detectors is their excellent compatibility with large FPA formats.

Initial imaging applications utilized quantum IR detectors. By the end of the last century, large focal plane arrays of resistive bolometers and ferroelectric devices with 320 x 240 pixels were available[4]. The reported thermal resolution values for these FPAs are as low as 23 mK[28, 29]. In the last several years, micromechanical IR detector FPAs with up to 256 x 256 pixels have been reported[16, 30, 31] with measured thermal resolution of few hundred mk[16]. The challenge facing uncooled IR imagers is to achieve thermal resolution values of only a few mK (i.e. performance equivalent to that of best cooled photonic detectors) while reaching the resolution of high definition television[11].

1.3 Applications

The initial driving force for infrared imaging was the military. IR imaging was used for night-vision and search-and-rescue applications. Military was the main user of these systems due to their high cost. However, with advances in technology, the cost is decreasing and IR imaging systems are becoming available for non-military applications. Those include security, non-invasive medical diagnostics, automotive industry, industrial imaging etc. In a burning building, the view is often obstructed by smoke. Firemen

equipped with infrared imaging devices would be able to rescue people more quickly. In case of a sickness or an injury, the body temperature changes locally. Infrared imaging could provide a heat map of the affected region, without the need for invasive procedures. A large fraction of traffic accidents occurs due to poor visibility. In foggy or dark conditions, a driver is less likely to spot a pedestrian, bicyclist or a deer. Infrared cameras installed on vehicles can substantially supplement driver vision. Some high-end vehicles already feature IR cameras.

Another area of applications has recently become available owing to the fact that IR imaging technology in its longest wavelength range has much in common with THz imaging, also known as T-ray imaging[32-35]. THz radiation is defined as the electromagnetic radiation band between 0.3 THz and 3 THz. As discussed elsewhere[36], the recent growing demand for T-ray detectors is driven by the need for more accurate, yet less harmful screening techniques in transportation and other homeleand security applications [32, 34, 35]. Devices that utilize T-rays for imaging have many attractive features from this standpoint. Hence, micromechanical structures have been explored as both IR and T-ray detectors[37-40]. The advantage of micromechanical thermal detectors is that they can be optimized for longer wavelengths in the IR range and for the THz range by using geometric scaling of the detector elements in proportion to the wavelength. In principle, FPAs of micromechanical thermal detectors similar to the ones used for IR imaging are sensitive to THz radiation. However, the characteristic linear sizes of each sensing element should be increased to a few hundred microns in order to optimize their performance in the THz range. For all purposes of this dissertation, the discussion about IR detection applies to THz detection except where explicitly mentioned.

1.4 Basic Principles

The output of a thermal IR detector is proportional to the increase in detector temperature, which is, in turn, proportional to the amount of heat provided by the absorbed photons. Since micromechanical IR detectors fall in the category of thermal IR detectors, their basic operation has much in common with other types of uncooled IR detectors.

An illustration of a typical uncooled thermal detector is displayed in Figure 2. The design is usually such to allow arranging (tiling) them in a two-dimensional array to maximize the fill factor. The detector consists of an absorbing element of heat capacity C connected to a heat sink, which is usually the substrate at temperature T_s, via thermal connector of thermal conductance G[41]. The absorbing element converts the incident IR radiation into heat. Heat induced by the incident power P causes an increase in detector temperature at a rate $dT_b/dt = P/C$. The temperature approaches the limiting value $T_s + P/G$ with time constant

$$\tau_{th} = \frac{C}{G} \tag{3}$$

After the radiation is turned off, the detector's temperature relaxes back to T_s with the same time constant.

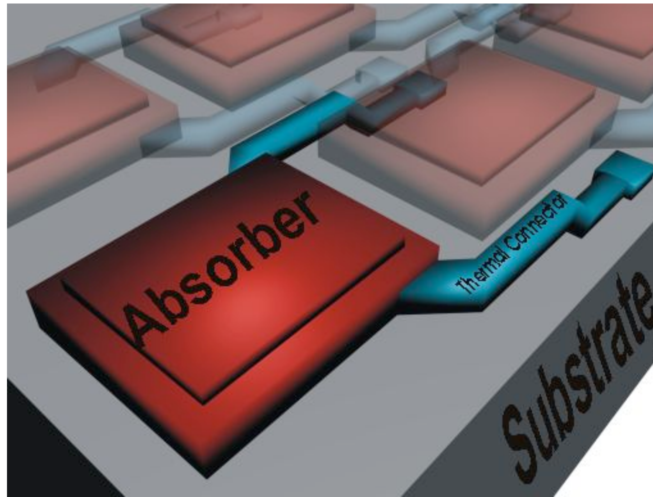

Figure 2 Conceptual illustration of the main parts of an infrared detector
The main parts of an IR detector are absorber, thermal connector and the substrate

The main parts of a typical infrared detector are an absorber, a supporting substrate/heat sink, and a thermal connector[41] (Figure 2). These components are required to meet certain criteria for the detector to work effectively. The absorber has to be large enough to adequately intercept the incoming IR flux. Absorber's has to have a low heat capacity in order to maximize the increase in temperature for a given absorbed energy as well as high absorption in the wavelength band of interest. Substrate has to have high heat capacity and large thermal conductivity in order to remain isothermal during operation. Thermal connector, linking the absorber and the heat sink, has to have low heat capacity and very low thermal conductance in order for the absorbed heat to be retained in the absorber sufficiently long to be detected. Equation 3, however, shows that there is a tradeoff between the requirement of fast response (low τ) and low thermal conductance.

1.5 Transduction Mechanisms for Micromechanical Detectors

This dissertation will focus on micromechanical infrared detectors. Micromechanical (MEMS) IR detectors are a subgroup of thermal IR, which utilize the effect of structural changes within the detector, which occurs when its temperature is changed. This structural change, proportional to the magnitude of temperature change, can manifest in the form of a shift in resonant frequency or a structural deformation and can be detected using various transduction mechanisms usually referred to as *readouts*. The readouts used to quantify the detector deformation demonstrated to date include the following: quartz micro-resonator[42], piezoresistive[22], capacitive[17], electron-tunneling[43], and optical[3, 16, 44].

Based on the type of readout utilized to quantify the deformation, micromechanical IR detectors are classified in different categories: a) *quartz micro-resonator*, where the

temperature change induces the shift in resonant frequency which is easily detected[42]; b) *piezoresistive micromechanical detector*, where the deformation is quantified by the change in the resistance of the detector[42]; c) *capacitive micromechanical detectors*, where the detector and the substrate form a capacitor whose capacitance changes with deformation of the detector due to change in capacitor-plate separation[45-47]; d) *pneumatic micromechanical detectors*[7] have a chamber , also known as the Golay cell, with enclosed air whose pressure changes with changes in temperature, deforming the membrane. Membrane motion is usually quantified by the changes in capacitance[7] or by electron tunneling[43, 48]; e) *optically-probed micromechanical detectors*, which gauge the deformation using the principle of cantilever readout similar to the readout utilized in Atomic Force Microscopy (AFM). In the AFM, the laser light is reflected off the tip of the cantilever and the cantilever deformation is detected by observing the motion of the reflected beam of light by a position sensitive detector.

Since bolometers have been developed earlier, methods for measuring the resistance change were the most convenient to use in early micromechanical infrared detectors[19, 22]. Another method of choice was to try measuring changes in capacitance[46]. Electrical connections for both of those readout techniques, however, required conductive links between the detector and the substrate. This meant higher thermal conductivity, which is not desired in most applications. The latest capacitive micromechanical detectors use materials with good thermal isolation[46]. Optical readout offers a good solution to this problem since it does not require electrical connections between the detector and the substrate. In this approach a single detector, or an array, is illuminated with visible light, which is reflected into either a position sensitive detector (such as a quad cell) or a charge coupled device CCD (such as the one used in conventional digital cameras). This type of readout allows good thermal isolation between detector and substrate.

In the case of quartz micro-resonators, the temperature change induces a shift in resonant frequency. The detector is connected to the circuitry monitoring the frequency. The frequency shift is proportional to the change in temperature.

In the case of pneumatic detectors, electron tunneling was utilized to quantify detector deformations.

In the case of piezoresistive readout, the temperature change induces deformation of a detector. Since one of the bimetallic layers is made of piezoresistive material, the resistivity of the material, and therefore the resistance of the whole detector, will change. The resistance change is proportional to the amount of deformation, which is proportional to the change in temperature. The detector is electrically connected to the bias voltage and change of resistance will induce a measurable change in current.

In case of a capacitive readout, the temperature change induces the deformation of the detector. Part of the detector, usually the absorbing element, acts as a movable plate of a variable capacitor[46]. The other capacitor plate is usually embedded into the substrate. Designs have been proposed featuring two parallel microcantilever structures, each representing a plate of a variable moving capacitor [45, 47]. When the detector is deforms, the distance between the capacitor plates changes, changing the capacitance. The detector is connected to the circuitry that measures the capacitance. The measured change will be proportional to the increase in detector temperature.

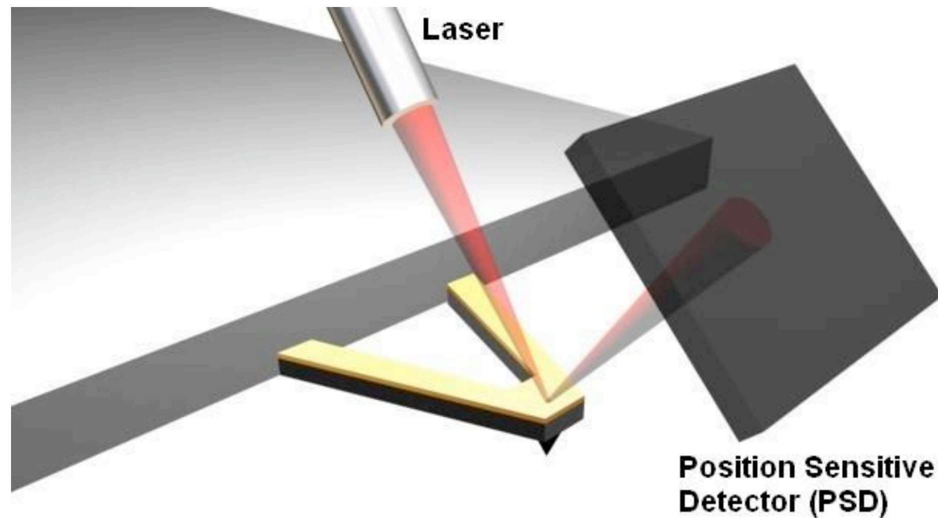

Figure 3 Illustration of an optical readout configuration
Readout configuration employed in the atomic force microscopy.

Optical readout is a common term used for two techniques. One technique is based on the approach developed for the atomic force microscopy (AFM) and is used for reading out single microcantilever detectors. The other technique probes multiple microcantilever detectors arranged in an array simultaneously. Figure 3 illustrates the configuration of single-detector optical readout. A laser beam is focused on the tip of the cantilever and reflected into the position sensitive detector (PSD). If the cantilever deflects, it will steer the reflected beam and the spot on the PSD will move. Based on the PSD output voltage, the exact displacement can be extracted down to sub-angstrom accuracy[49].

In a configuration for probing multiple detectors simultaneously, a light source illuminates the entire detector array. Figure 4 illustrates a simplified representation of the optical-detector-array readout. The light is reflected off the front (reflective) side of M × N array of detectors and is projected onto the CCD via *Lens 2*. IR radiation from the target being imaged is projected onto the backside of the array via IR lens, which is made out of IR-transmitting material such as Ge. Depending on the shape and temperature distribution of the target, the magnitude of deformation of individual detectors will differ corresponding to different temperatures on the target. The aperture will block a portion of light reflected off the deformed detectors and the amount of light reaching the corresponding CCD pixels will decrease. These changes in intensity will translate into areas of different brightness intensities on the reconstructed thermal image. The different brightness levels will corresponds to different temperatures on the imaged object. Based on the brightness of image pixels recorded by the CCD, the relative level of deformation of each corresponding detector can be determined.

In the case of both types of optical readout, the absorber of IR radiation, defined in Figure 2, also serves as a reflector of probing (visible) light. Further in the text, the terms absorber and reflector will be used interchangeably depending on the context of the description.

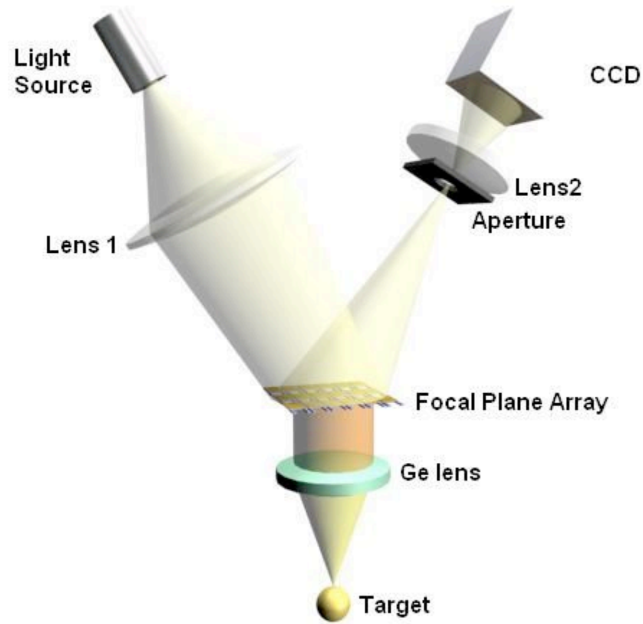

Figure 4 Illustration of the optically-probed array of micromechanical uncooled infrared detectors
The IR lens projects the incoming IR radiation from the target onto the focal plane array. The FPA is illuminated from the other side by a visible light and the reflection is focused onto the CCD.

In the last several years, optically-probed micromechanical (MEMS) uncooled infrared detectors and imagers have drawn substantially increased attention [4, 8, 15, 17, 23, 26, 31, 50-53]. Indeed, focal plane arrays (FPAs) of optically probed micromechanical detectors offer an attractive alternative to other, well-established, uncooled infrared detectors such as microbolometers. This is largely due to the significantly simpler microfabrication and, in turn, potential for high yield and low cost. It is worth noting that the need for on-chip electronics combined with exotic materials determines microfabrication complexity, high fabrication cost and low yield of microbolometer FPAs. Several groups have already demonstrated MEMS-based infrared imaging devices [4, 8, 15, 17, 23, 26, 31, 50-53] that address this challenge.

The goal of this dissertation is to demonstrate the possibility of improvements to micromechanical uncooled IR detectors to improve their performance in order to make them comparable to other contemporary uncooled IR imagers. To achieve this, we intend to analyze, combine and implement new ideas in detector geometry, choice of materials and modifications to the substrate.

Chapter 2

Figures of Merit

The definitions and analysis from *Detectors – Figures of Merit* chapter of Encyclopedia of Optical Engineering written by P.G. Datskos and N.V. Lavrik[54] are used in this chapter.

There exists a need to characterize and compare performance of different types of infrared detectors such as quantum detectors, bolometers and other types of thermal IR detectors. In the last several decades, a number of different figures of merit have been defined[10, 11, 27, 55-59]. Being a new and evolving field, the field of IR detectors uses the parameters and figures of merit that are evolving as well. New parameters are emerging while some become outdated. In this text, we discuss the figures of merit currently accepted and used by the IR community[55, 60].

Datskos and Lavrik remind that although the need for using figures of merit is driven by the desire to compare different detectors, it is important to keep in mind that different assumptions are sometimes made in defining and measuring these parameters. When evaluating the performance of various IR detectors, especially those utilizing uncooled thermal detectors, the parameters of major importance are 1) responsivity, R; 2) noise equivalent power (*NEP*); 3) normalized detectivity, D^*; 4) noise equivalent temperature difference (*NETD*); 5) minimum resolvable temperature difference (*MRTD*); and 6) response time τ[55, 57, 60]. The definitions of these parameters and their fundamental limits in the case of uncooled thermal IR detectors will be discussed in detail. There are a number of additional parameters that can be used for a more detailed and comprehensive characterization of IR detectors. These include linearity of response, cross-talk between detector elements in an FPA, dynamic range, and modulation transfer function (MTF). The linearity of response, cross-talk, and dynamic range are basic parameters amenable to a whole variety of analog devices and transducers, and their definitions are readily available from a number of sources[59, 61]. MTF is traditionally used in testing the performance of lenses, imaging systems, and their components and describes how the output contrast changes as a series of incrementally smaller features are imaged.[54, 61]

2.1 Responsivity

Responsivity R, which is applicable to all infrared detectors, describes the gain of the detector and is defined as the output signal (typically voltage or current) of the detector produced in response to a given incident radiant power falling on the detector[55, 57]. The responsivity is expressed as:

$$R_V = \frac{V_s}{P_0} \text{ or } R_I = \frac{I_s}{P_0} \tag{4}$$

where V_s is the output voltage (V), I_s is the output current (A), and P_0 is the radiant input power (W). If the definition of responsivity is expanded to include the frequency dependence and the wavelength (spectral) dependence [55], it is then referred to as the spectral responsivity, $R(\lambda, f)$. Datskos and Lavrik emphasize that in the case of quantum and thermal IR detectors very distinct factors define characteristic features of spectral responsivities. Quantum IR detectors exhibit a cut-off in the spectral responsivity above a certain characteristic wavelength that is related to the photon energy sufficient to generate additional charge carriers (free electrons or electron-hole pairs). Hence, $R(\lambda, f)$ has a long-wavelength cut-off defined by the bandgap energy of the semiconductor or the energy barrier at the metal-semiconductor interface used in the detector. In the case of thermal IR detectors, however, the far-IR range is readily accessible simply by using appropriate detector absorbing areas and materials with high-absorptivity (either direct or resonant absorption) in this region.[54]

A derivative of responsivity, known as blackbody responsivity $R(T, f)$, is defined as an additional parameter and includes the dependence of the detector output signal on the temperature, T, of the blackbody-type source.

The responsivity is a useful design parameter that describes levels of output signal caused by a given power of IR radiation coming from an object of a given temperature and emissivity. Although a good indicator of an IR detector performance, the responsivity does not describe the level of any intrinsic noise in the detector and, therefore, provides little or no information about detector's threshold sensitivity. This means that an IR detector characterized with high responsivity is not necessarily able to detect low-level IR radiation or to distinguish between different IR sources of nearly the same temperature. Datskos and Lavrik conclude that knowing the detector responsivity is important during the IR detection system design, while comparative evaluation of different detectors should rely on other figures of merit[54].

In the case of micromechanical IR detectors, which mechanically deform in response to the incoming IR power, it is natural to define the responsivity in terms of the mechanical response of the detector, i.e., displacement, z_s, per unit of absorbed power, P_0, in units of meters per watts, as

$$R_z = \frac{z_s}{P_0}. \tag{5a}$$

Similarly as before, a spectral responsivity $R_z(T, f)$ and a blackbody responsivity $R_z(\lambda, f)$ can be defined.

Lately, however, the level of deformation of micromechanical IR detectors is being described by the deformation angle of the reflector [50, 53]. Using the angle to quantify the deformation is convenient, especially for systems with optical readout. This is because, in most cases, optical readout is sensitive to the change of the angle of the reflector. In addition, the tip displacement can be deceptive since smaller relative deformation of a large structure yields larger tip deflection. Angle of deformation is, in a way, scaled to and is independent of the detector size. The parameter describing the angle of deflection per unit of temperature increase (discussed bellow) requires a responsivity defined in terms of the angle θ of the detector deflection per unit of absorbed power, P_0, in units of radians per watt.

$$R_\theta = \frac{\theta_s}{P_0} \tag{5b}$$

2.2 Noise Equivalent Power

Noise Equivalent Power, *NEP*, is defined as the incident radiant power that produces a signal equal to detector's root mean square (rms) noise[55, 57]. This parameter represents a convenient way to characterize the sensitivity of an IR detector. By this definition, *NEP* includes information about both gain and noise parameters of the detector and can be related to the detector responsivity, R_V, R_I, R_z or R_θ, and the rms detector noise [55]

$$NEP = \frac{V_N}{R_V} \text{ or } NEP = \frac{I_N}{R_I} \text{ or } NEP = \frac{z_N}{R_z} \text{ or } NEP = \frac{\theta_N}{R_\theta} \tag{6}$$

where V_N (I_N, z_N or θ_N) is the rms noise voltage (current, displacement or angle) measured within the whole operation bandwidth. As pointed out by Datskos and Lavrik, since *NEP* depends on *R*, it also depends on the photon wavelength as well as on the modulation frequency of the IR power and, therefore, can be regarded to as $NEP(\lambda, f)$. They further state that *NEP* can also be specified as a function of detector temperature, i.e., $NEP(T_D, f)$[55]. Frequency dependence of *NEP* is determined by the detector thermal response time, τ, and by the spectral density (i.e., frequency dependence) of the detector noise. It is important to note that even if the noise amplitude is frequency independent (white noise), the rms noise spectral density exhibits a square root dependence on the frequency. $NEP(\lambda, f)$ and $NEP(T_D, f)$ refer to a 1-Hz bandwidth and have units of W $Hz^{-1/2}$; *NEP* without specifying the frequency may have ambiguous interpretation. The units of *NEP* imply either a full operational bandwidth or a 1-Hz bandwidth[54].

2.3 Normalized Detectivity

Even though the *NEP* is sufficient for adequate evaluation and comparison of performance of individual (spot) IR detectors by predicting the minimum detectable power, its value is inversely proportional to the detector performance, i.e. its higher value implies lower quality. Therefore the need rose for a parameter that would be directly proportional to detector's performance. Starting with a parameter known as detectivity,

D, which is defined as the inverse value of NEP and taking into account the detector absorbing (active) area, A_d, and the signal bandwidth, B, one can define specific (or normalized) detectivity, D^*, as[55]

$$D^* = \frac{\sqrt{A_d B}}{NEP} \tag{7}$$

According to Equations 4, 5a, 5b and 6, normalized (or specific) detectivity D^* is the detector output signal-to-noise ratio at 1 W of input IR radiation normalized to a detector with a unit active area and a unit bandwidth. The units of D^* are in Jones; 1 Jones = 1 cm $Hz^{1/2}$ W^{-1}. Datskos and Lavrik note that the definition of specific detectivity, D^*, was originally proposed for quantum detectors, in which the noise power is always proportional to the detector area and noise signal (V_n or I_n) is proportional to the square root of the area. However, the noise in thermal IR detectors does not always obey this scaling trend. In fact, neither temperature fluctuations nor thermo-mechanical noise (see the next section) scales up with the detector area. Therefore, D^* should be very cautiously interpreted when applied to thermal IR detector. In fact, D^* tends to overestimate the performance of larger absorbing area thermal detectors and underestimates the performance of smaller ones. Normalized detectivity, D^*, (even in the case of quantum detectors), generally ignores the significance of smaller detector size for high-resolution FPAs[54].

2.4 Noise Equivalent Temperature Difference

Noise Equivalent Temperature Difference (*NETD*) is a parameter that describes the low-signal performance of thermal imaging systems and is more applicable to FPAs of IR detectors than to the individual detectors. Over the years, it has emerged as one of the most commonly used parameters for describing the performance of IR imagers. *NETD* is defined as the temperature of a target above (or below) the background temperature that produces an output signal equal to the rms detector noise[55, 57, 62]. *NETD* can be represented as a histogram of values for each individual detector element, or can be averaged for all detector elements in an array. Alternatively, NETD can be defined as the difference in temperature between two blackbodies, which corresponds to a signal-to-noise ratio of unity[57]. Image produced by an IR imager is a map of detected temperature variation across a scene or an object. Datskos and Lavrik note that the resulting images are also affected by the emissivity of the objects in the scene. Small values of *NETD* reflect the ability of an IR imager to distinguish slight temperature or emissivity differences of objects. Relationships for predicting *NETD* have been described elsewhere[10, 11, 55, 62]. *NETD* can also be determined experimentally for a given detector area, detector absorptivity, optics used, and output signal bandwidth[62] by

$$NETD = \frac{V_N}{V_S}(T_t - T_B) \text{ or} \tag{9a}$$

$$NETD = \frac{I_N}{I_S}(T_t - T_B) \text{ or} \tag{9b}$$

$$NETD = \frac{z_N}{z_S}(T_t - T_B) \tag{9c}$$

where V_N (I_N or z_N) is the voltage (current or deflection) rms noise, V_s (I_s or z_s) is the voltage (current or deflection) signal, T_t is the temperature of the blackbody target, and T_b is the background temperature. Datskos and Lavrik further emphasize that the *NETD* of optimized thermal IR detectors is limited by temperature fluctuation noise, while background fluctuation noise imposes an absolute theoretical limit on the *NETD* of any IR detector[54]. In Chapter 4, the factors affecting the temperature fluctuation noise, background fluctuation noise and thermo-mechanical noise will be discussed in more detail.

2.5 Response Time

IR detectors exhibit characteristic transient behavior when the input power changes abruptly, as in case of other sensors or transducers. A general definition of the *response time*, τ, for any sensor system is the time required for a transient output signal to reach 0.707 ($\sqrt{2}$) of its steady-state change. The expressions of the responsivity in the time and frequency domains are given by[61]

$$R(t) = R(t = \infty)\left[1 - e^{-\frac{t}{\tau}}\right] \tag{10}$$

$$R(f) = \frac{R_0}{\sqrt{1 + (2\pi f\tau)^2}} \tag{11}$$

respectively, where R_0 is the DC responsivity.

In the case of photo-electronic (quantum) detectors whose transduction of the absorbed IR energy into the output signal is based on photo-electronic processes, the intrinsic response time can be less than a nanosecond[63]. Even though the impedance of the electronic readout often limits their response times, the response times of complete imaging systems are still shorter then 1 ms [9], which is more then enough to meet the requirements of most real-time imaging applications. On the other hand, the overall response time in case of micromechanical detectors is directly related to their much longer intrinsic response times and not by the readout. High intrinsic response times (mostly in the range of 1 to 100 ms) are the consequence of the transduction mechanism which requires accumulation of heat in the detector active area. The response time of a thermal IR detector, τ_{th} (Equation 3), is calculated as the ratio of heat capacity of the detector to the effective thermal conductance between active area of the detector and its support structure (i.e. a heat sink).

Equation 3 is a convenient tool for predicting the response times of all types of thermal IR detectors, including micromechanical IR detectors. In Equation 3, the heat capacitance, C, is the total capacitance which combines the heat capacitances of each layer in the active area of the detector. The heat capacitance of each layer is calculated as a

product of the specific heat capacitance of the layer material and its mass. The thermal conductance, *G,* needs to include all of the heat loss mechanisms in the detector (i.e. conductive, convective and radiative losses).

Chapter 3

Theoretical Background for Micromechanical Infrared Detectors

The analysis from *Performance of Uncooled Microcantilever Thermal Detectors* article in Review of Scientific Instruments written by P.G. Datskos, N.V. Lavrik and S. Rajic[14] was used for this chapter.

Since most of the work done in the field of micromechanical uncooled IR detectors such as those with piezoresistive, capacitive and optical readouts is performed with bimaterial microcantilever detectors, for the this dissertation, only focuses on this type of detectors. Figure 5 displays a cartoon representation of a typical micromechanical IR detector. A micromechanical IR detector typically consists of the absorber or an active part, which undergoes deformation when the detector temperature changes, and two supporting beams (legs) that provide structural support for the absorber as well as thermally connect the absorber to the substrate. Most of the structure is usually made out of the same material taking advantage of already well-established microfabrication methods developed for Si-based microelectronics industry. Therefore the structures analyzed in literature are built mostly of microfabrication-friendly materials such as silicon or silicon nitride. Absorber is usually a bimaterial region and consists of the part of structure coated with certain material, usually a metal. Some designs [14, 30] separate the absorbing section of the detector into the deforming region and reflecting region. This separation is usually employed in optically-probed systems. As discussed above, legs are designed to provide optimal thermal isolation between the absorber and the heat sink, which in most cases is the substrate on which the detectors are fabricated.

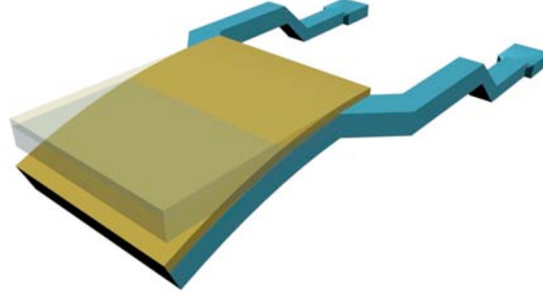

Figure 5 Illustration of a micromechanical, infrared detector.
Micromechanical uncooled infrared detector has bimaterial region and thermal isolation region. Bimaterial region serves as an absorber. Undeformed bimaterial region is shown as transparent whereas the detector is shown as deformed

3.1 Bimetallic Effect

When heated, the active part of the detector undergoes a deformation due to the bimetallic effect. This effect was first explained by Timoshenko[64], and it states that structure will deform when heated if it consists of two layers with materials of different coefficients of thermal expansion (Figure 6). This deformation occurs because two layers expand at different rates with the same temperature change. Deformations of microstructures are of the order of nanometers. Once readouts that quantify microstructure deflections reached sensitivities sufficient for measuring even sub-angstrom deflections[49], optically probed bimetallic structures became applicable to the IR detection.

The deflection, Δz, of the tip of a cantilever consisting of two material layers due to temperature increase of ΔT is given by[64, 65]

$$\Delta z = \frac{3l_b^2}{t_1 + t_2}\left[\frac{\left(1+\frac{t_1}{t_2}\right)^2}{3\left(1+\frac{t_1}{t_2}\right)^2 + \left(1+\frac{t_1}{t_2}\frac{E_1}{E_2}\right)\left(\frac{t_1^2}{t_2^2}+\frac{t_2}{t_1}\frac{E_2}{E_1}\right)}\right]\times(\alpha_1-\alpha_2)\Delta T \quad , \qquad \text{(12a)}$$

where l_b is the microcantilever bimaterial length, t_1 and t_2 are the thickness of the coating and the microcantilever substrate respectively, α_1 and α_2 are the thermal expansion coefficients of the coating and the microcantilever and E_1 and E_2 are the Young's moduli of the coating and the microcantilever. If n is defined as $n = t_1/t_2$ and $\Phi = E_1/E_2$ and $K = 4 + 6n + 4n^2 + \phi n^3 + 1/\phi n$ this expression can be simplified to:

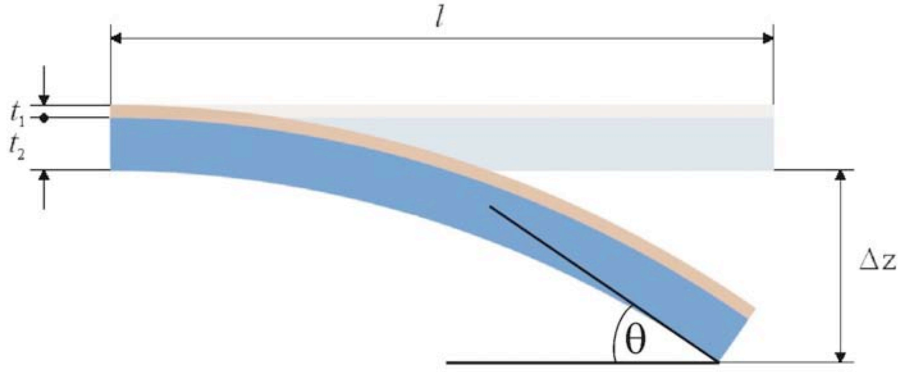

Figure 6 Deformation of the bimaterial structure due to temperature increase
This figure defines tip displacement, Δz, and deflection angle θ of a structure consisting of two layers. Structural layer, of thickness t_2, is shown in blue and metal coating, of thickness t_1, is shown in gold color.

$$\Delta z = 3(\alpha_1 - \alpha_2)\left(\frac{t_1 + t_2}{t_2^2 K}\right) \times l_b^2 \Delta T. \tag{12b}$$

Similarly, the angle of deformation $\Delta\theta$ is expressed as[50]:

$$\Delta\theta = 6(\alpha_1 - \alpha_2)\left(\frac{t_1 + t_2}{t_2^2 K}\right) \times l_b \Delta T. \tag{13}$$

It can be seen from Equations 12a, 12b and 13 that with optimized detector geometry and properly selected materials, Δz can be maximized. One would think that better deflection automatically improves sensitivity and responsivity of the detector. However, it will be shown that maximizing Δz alone does not necessarily improve the overall performance of the detector. Many parameters are interconnected and improving one of them might be hurting another. For example, increased cantilever length would improve Δz, but would at the same time increase the thermomechanical noise.

Typical dimensions of the whole detector range from a few tens to few hundred μm. Main structure thickness varies from few hundred nm to few μm. Taking that into account with the material properties of the SiN_x and Al (Table 1), the reported thermo-mechanical sensitivities, $\Delta z/\Delta T$, range from ~50 nm/K [15] to ~500 nm/K.

Once $\Delta z/\Delta T$ is defined, we need to consider the temperature increase, ΔT, of the detector due to photon absorption. As a first approximation, it can be assumed that the main heat loss mechanism is the conductance of the thermal isolation region (legs). In addition to heat dissipation through legs, the heat can be dissipated through convection of the surrounding gas as well as through radiation. However, the convection of the gas surrounding the detector is pressure dependent [66] and is minimized by operating most of the detectors at very low pressures. The conductance through radiation is negligible in comparison to the conductance of the thermal isolating region (legs). With these assumptions, the solution to the heat flow equation yields [11] :

Table 1 Material properties

	Young's Modulus E (x 10^6 Pa)	Expansion Coefficient α (x 10^{-6} K^{-1})	Thermal Conductivity g (W m^{-1} K^{-1})	Heat Capacity c (J kg^{-1} K^{-1})	Density ρ (x 10^{-3} kg m^{-3})
SiN_x	180	2.1	19	691	2400
Al	70	25	237	900	2200
Au	77	14.2	296	129	19300
SiO_2	68	0.4	1.4	703	2700
Si	100	2.7	130	750	2330

$$\Delta T = \frac{\eta P_0}{G\sqrt{1+\omega^2\tau^2}} \quad (14)$$

where P_0 is the radiant power falling on the cantilever, η is the absorbance (absorbed fraction) of the radiant power, G is the thermal conductance of the principal heat loss mechanism, ω is the angular frequency of modulation of the radiation, and τ is the thermal response time described by Equation 3.

3.2 Thermal Conductance

The value of the thermal conductance of the thermal isolation region, G_{legs}, is a product of thermal conductivity, g, of the microcantilever legs and their cross-sectional area divided by their length

$$G_{legs} = 2 \times \frac{g \cdot w_{leg} \cdot t_{leg}}{l_{leg}}, \quad (15)$$

where g is the thermal conductivity of the material constituting the legs. The factor of 2 comes from the fact that most geometries feature two identical legs as illustrated in Figure 2 and Figure 5. The term (w_{leg} t_{leg}) is the crossectional area of the legs. For microcantilever detectors with complex leg structure [14], the thermal conductance G_{legs} will have more complex expression.

The thermal conductance of the legs, however, is not the only path for energy dissipation. Figure 7 shows the thermal conductance as a function of the thermal isolation length calculated using the parameters listed in Table 1, assuming leg thermal isolation leg width w_{leg} of 1.5 μm and its thickness t_{leg} 0.6 μm. The dashed-dotted lines in Figure 7 represent the thermal conductance due only to conduction (legs). Most reported structures have the legs with thermal conductances of the order of ~ 10^{-7} W/K [14-16, 31]. From Figure 7 we can see that using SiO_2 as the base material of the cantilevers can provide structures with lower thermal conductance. This is also evident from the Table 1 which shows that SiO_2 has much lower thermal conductivity than SiN_x. The lower dashed and dotted line (G_{rad}) represents the radiative component of total conduction where the energy is dissipated by radiation. The radiative component is expressed as[54]

$$G_{rad} = 4\,(\varepsilon_{metal}+\varepsilon_{structure})\,A_d\,\sigma_T\,T^3, \quad (16)$$

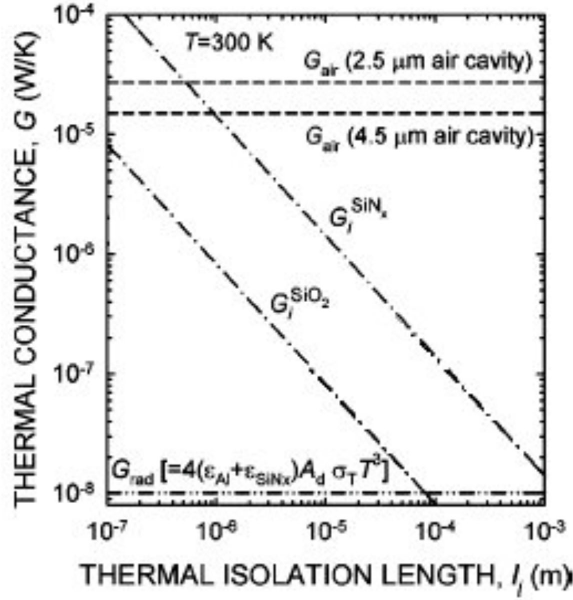

Figure 7 Plots of calculated thermal conductances versus the length of thermal isolation region

The dashed-dotted lines represent the conductance through legs only as a function of leg length. The upper horizontal lines represent the upper limit defined by the conductance through the air at atmospheric pressure. The lower horizontal lines represent the lower limit of thermal conductance which is defined by the radiative conductance

where $\varepsilon_{\text{metal}}$ and $\varepsilon_{\text{structure}}$ are emissivities of the metal coating in the absorbing element and the main material respectively, A_d is the area of the detector, σ_T is the Stephan-Boltzmann constant and T is the detector temperature. For most common SiN_x–based structure dimensions, conductance is of the order of ~10^{-7} W/K at room temperature when taking into account the detector area of the order of ~10^{-9} m^2 and the Stephan–Boltzmann constant, $\sigma_T = 5.67 \times 10^{-8}$ W^{-2} K^{-4}. This calculation also assumes that the emissivity of the metal and structural material side of the detector is, respectively, $\varepsilon_{\text{metal}} \sim 10^{-2}$ and $\varepsilon_{\text{structural}} \sim 10^{-1}$. Under ambient pressure and temperature, the thermal conductance through air is of the order of ~10^{-5} W/K[14] in the case of gaps between the detector and the substrate of several μm (see the two upper dashed line marked G_{air} in Figure 7). This value assumes thermal conductivity of air, at standard temperature and pressure, to be at 2.5×10^{-2} Wm^{-1} K^{-1} [12]. At temperatures of 200 K and 400 K, the thermal conductivity of air is 1.9×10^{-2} Wm^{-1} K^{-1} and 3.2×10^{-2} Wm^{-1} K^{-1}, respectively.

As discussed by Datskos et al. in [14], it is worth noting that uncooled IR detectors rely on both intrinsic photon absorption and resonant cavity effects in order to increase the overall photon absorption. Tuning the absorption maximum of the resonance cavity to a wavelength of 10 μm requires a 2.5 μm (for front end illumination) or 4.5 μm (for back end illumination) gap between the substrate and the microcantilever detector.

However, when the detector is positioned at these distances above the substrate in air, the convection limits its performance. Depending on the distance between the detector and the substrate, this may yield a thermal conductance larger than the thermal conductance through the legs of a typical microcantilever. Therefore, heat convection through air is likely to be a dominant heat dissipation mechanism when a microcantilever detector operates in an atmospheric environment and in close proximity to the substrate [14]. Djuric et al. discuss the dependence of the thermal conductance and *NETD* on pressure in detail [66]. In order for the assumption that the heat is dissipated through the legs only to be valid, the conductance through the other two mechanisms has to be negligible. In order to minimize the convection through the air surrounding the microcantilever detector, the detector needs to be placed in an environment with substantially reduced pressure, such as an evacuated package. The thermal conductance of micromechanical detectors, in their normal operating conditions, is usually of the order of 10^{-7} W/K.

Datskos et al. point out that the only frequency-dependent term in Equation 12a, 12b and 13 is ΔT, which involves the thermal time constant (Equation 14). As the modulation frequency increases, ΔT and the detector response remains constant as long as the product $\omega\tau$ is small compared to unity. At higher frequencies, ΔT begins to decrease, which causes the response to decrease [14]. This explains the observed roll-off in the response of the tested cantilever above ~60 Hz as shown in Figure 8 (curve A). The frequency at which the slope of the response changes on a log-log plot can be used to experimentally evaluate the response time as it occurs at frequency where the $\omega\tau$ product becomes equal to unity (Bode plot method). The response time can therefore be estimated as $1/f_c$, where f_c is the frequency at which the slope on the graph changes. The data shown in Figure 8 were recorded using a setup similar to the one described elsewhere [25]. It is important to emphasize that microcantilevers also exhibit mechanical resonances. The curve (B) in Figure 8 [14] shows that although the signal increases at the resonance, so does the noise. Operating detectors at their resonance frequency would, therefore, not provide a significant advantage for IR detection.

3.3 Microcantilever Responsivity

As mentioned in section 3.1, the responsivity, *R*, of an IR detector is defined as the output signal produced by the unit of incident radiant power. Datskos et al. have shown [19, 25] that the signal (relative response) of a microcantilever is linear with incident radiant power over a large range. Therefore, it is valid to determine an expression for responsivity that is independent of incident radiant power. Furthermore, the gain of the optical readout is anticipated to be independent of Δz in the case of relatively small cantilever deformations [14].

Since the microcantilever thermal detectors can be regarded as oscillators, and the incoming radiation can be regarded as non-DC, dynamic stimulus, the analysis for driven harmonic oscillators can be applied to cantilevers. Therefore, the responsivity, *R*, of a micromechanical infrared detector with rectangular bimaterial region Figure 6 can be calculated by using Equations 12a and 14 and regarding the cantilever as a driven harmonic oscillator:

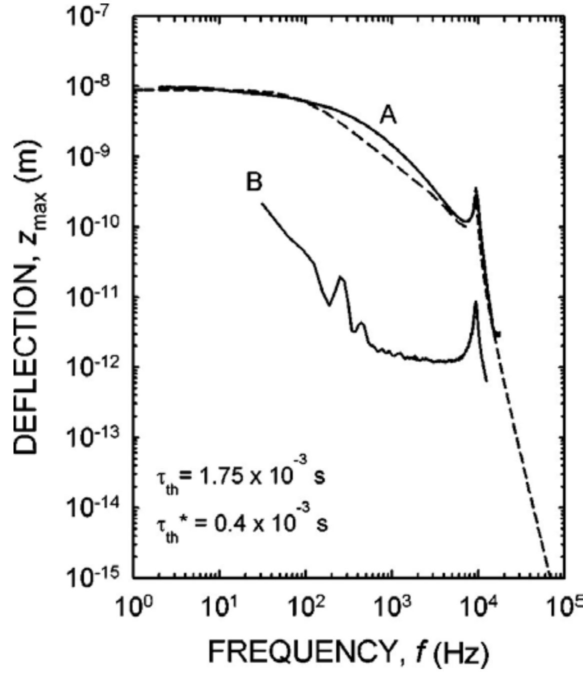

Figure 8 Frequency spectrum of the detector discussed in [14].
Plot A represents a response to external thermomechanical excitation while plot B represent spectrum due to ambient temperature fluctuations

$$R(\omega) = \frac{\Delta z}{P_0} = \eta \frac{3l_b^2}{(t_1 + t_2)} \left[\frac{\left(1 + \frac{t_1}{t_2}\right)^2}{3\left(1 + \frac{t_1}{t_2}\right)^2 + \left(1 + \frac{t_1}{t_2}\frac{E_1}{E_2}\right)\left(\frac{t_1^2}{t_2^2} + \frac{t_2}{t_1}\frac{E_2}{E_1}\right)} \right] \times (\alpha_1 - \alpha_2)$$

$$\times \frac{1}{G_T\sqrt{1+\omega^2\tau^2}\sqrt{\left(1-\frac{\omega^2}{\omega_0^2}\right)^2 + \frac{\omega^2}{\omega_0^2 Q^2}}} = \eta\left(\frac{\Delta z}{\Delta T}\right)\frac{1}{G_T}\frac{1}{\sqrt{\left(1-\frac{\omega^2}{\omega_0^2}\right)^2 + \frac{\omega^2}{\omega_0^2 Q^2}}} \quad (17a)$$

where ω is the angular frequency of modulation of the radiation, ω_0 is the resonance frequency of the cantilever, and Q is the quality factor. The units of R are meters (of deflection) per Watt (of incident power). Alternatively, using Equations 12b and 14 or Equations 13 and 14, we obtain respectively:

$$R(\omega)=\frac{\Delta z}{P_0}=3\eta(\alpha_1-\alpha_2)\left(\frac{t_1+t_2}{t_2^2K}\right)l_b^2\times\frac{1}{G_T\sqrt{1+\omega^2\tau^2}\sqrt{\left(1-\frac{\omega^2}{\omega_0^2}\right)^2+\frac{\omega^2}{\omega_0^2Q^2}}}$$

$$=\eta\left(\frac{\Delta z}{\Delta T}\right)\frac{1}{G_T}\frac{1}{\sqrt{\left(1-\frac{\omega^2}{\omega_0^2}\right)^2+\frac{\omega^2}{\omega_0^2Q^2}}} \qquad (17b)$$

and

$$R_\theta(\omega)=\frac{\Delta\theta}{P_0}=6\eta(\alpha_1-\alpha_2)\left(\frac{t_1+t_2}{t_2^2K}\right)l_b\times\frac{1}{G_T\sqrt{1+\omega^2\tau^2}\sqrt{\left(1-\frac{\omega^2}{\omega_0^2}\right)^2+\frac{\omega^2}{\omega_0^2Q^2}}}$$

$$=\eta\left(\frac{\Delta\theta}{\Delta T}\right)\frac{1}{G_T}\frac{1}{\sqrt{\left(1-\frac{\omega^2}{\omega_0^2}\right)^2+\frac{\omega^2}{\omega_0^2Q^2}}} \qquad (18)$$

If a function $\Omega(\omega)$ is defined to describe the normalized resonance curve, and is expressed as

$$\Omega(\omega)=\frac{1}{\sqrt{\left(1-\frac{\omega^2}{\omega_0^2}\right)^2+\frac{\omega^2}{\omega_0^2Q^2}}}, \qquad (19)$$

then the responsivity of a thermal detector can be expressed as $R(\omega) = R_0(\omega)\Omega(\omega)$ where $R_0(\omega)$ is responsivity at DC incoming radiation. Equations 17a, 17b and 18 also define other parameters commonly used, thermomechanical sensitivities defined as $\Delta z/\Delta T$ and $\Delta\theta/\Delta T$.

It is not trivial to obtain the value of the absorbance, η since it depends on a number of factors, such as material properties and detector geometry. Furthermore, as pointed out by Datskos et al. [14], it is possible to improve the absorption in the wavelength region of interest and hence increase the value of η by utilizing the resonant cavity effects. By designing a resonant optical cavity into the active (absorber) area, it is possible to maximize the infrared absorbance and, in turn, the thermally induced deformations of the detector. For simpler microcantilever designs, however, Datskos et al. offer the value of $\eta = 0.6$ as a reasonable assumption for most cases [14]. The R wavelength dependence has been shown to be closely related to the wavelength dependence of the absorbance bands of the detector structural material and/or the bands of the optical cavity designed to increase the photon absorption[14].

Figure 9 [14] shows the measured microcantilever responses as a function of wavelength of absorbed photons in the range of 2.5 μm to 14.5 μm. Solid line shows the detector spectral response normalized by the incident radiation power. The observed increased responsivity around 4 μm wavelength can be attributed to the effect of an optical resonance cavity formed by a 550 nm thick SiN_x film on an Al mirror. Dashed

curve in Figure 9 shows the independently measured absorptivity of a SiN_x membrane, which was used in the fabrication of the cantilever detector. The correlation between the two indicates that the higher detector responsivity in the region of 8 to 14 μm is mostly due to the intrinsic absorption of SiN_x.

It should be noted that Equation 17 defines the responsivity in terms of the magnitude of deflection of the detector, Δz, and, therefore, characterizes the micromechanical detector only. A total, system-level, responsivity should be expanded to also include the differential signal of the photocell used in the optical readout. The respective expression and the values obtained using this expression will be discussed later in the dissertation.

It is also useful to know the relationship between the deflection of a micromechanical infrared detector and the change in the temperature of the target, T_t. The change in target temperature will induce a corresponding change in the temperature of the detector. It is obvious that the imaging optics plays an important role in this and it should be included in the equation. Assuming the emissivity of the target $\varepsilon_T = 1$, the power incident on the micromechanical infrared detector is given by[14]:

$$P_0 = \tau_0 \frac{A_d}{4F^2}\left(\frac{dP}{dT}\right)_{\lambda_1-\lambda_2} T_t, \quad (19)$$

where A_d is the surface area of the detector, F is the focal ratio of the optics, τ_0 is the transmission of the optics, and $(dP/dT)_{\lambda 1-\lambda 2}$ is the slope of the function $P = f(T_t)$ where P is power radiated by a blackbody target within the spectral band from λ_1 to λ_2. Combining Equations 17 and 19, the change in microcantilever deflection can be expressed as

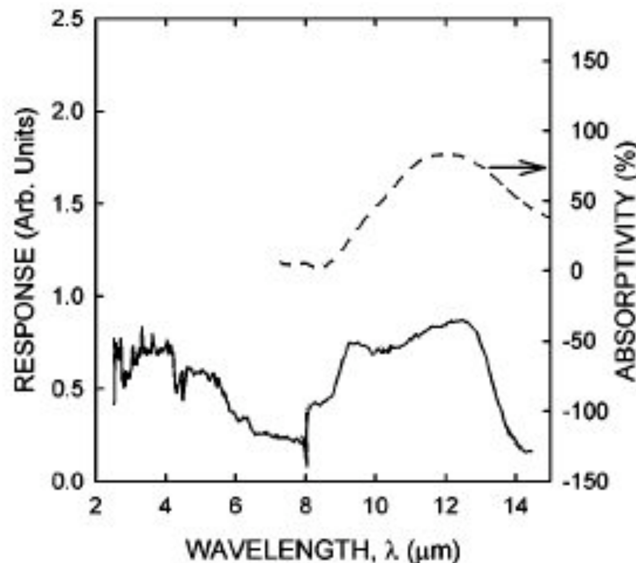

Figure 9 Measured response of a SiN_x detector discussed in [14].
Curve A represents the normalized response of a cantilever to infrared photons of different wavelengths. Curve B shows the absorbtivity of SiN_x in the wavelength range from 7 μm to 15 μm.

$$\Delta z = \tau_0 \frac{A_d}{4F^2} R(\omega) \left(\frac{dP}{dT} \right)_{\lambda_1 - \lambda_2} T_t \tag{20}$$

where R is the microcantilever responsivity. This expression shows the relation of changes in the microcantilever deflection to changes in the temperature of the target. For most reported structures, the above-defined Δz is of the order of few Å per 1 K temperature change of the target. If the ratio of temperature change of the detector to the temperature change of the target is obtained, it gives the *transfer function* [14, 31]. Transfer function can be obtained by combining Equations 14 (in static state) and 19 and is given by:

$$H = \frac{\eta \tau_0 A_d}{4F^2 G} \left(\frac{dP}{dT} \right)_{\lambda_1 - \lambda_2} . \tag{21}$$

The transfer function is usually of the order of inverse of a few hundred. That means that, in case of transfer function of 0.01, for each degree K change of temperature of the target, the temperature of the detector will change by 10 mK.

Chapter 4

Noise Sources and Fundamental Limits They Impose

The analysis from *Performance of Uncooled Microcantilever Thermal Detectors* article in Review of Scientific Instruments written by P.G. Datskos, N.V. Lavrik and S. Raijc [14] and The definitions and analysis from *Detectors – Figures of Merit* chapter of Encyclopedia of Optical Engineering written by P.G. Datskos and N.V. Lavrik [54] were used for writing this chapter.

This chapter analyzes the noise sources impacting the mechanical IR detectors and the extent of influence of those sources on detector performance. This analysis is needed in order to be able to compare the performance of uncooled mechanical IR detectors to that of cooled detectors and uncooled non-mechanical detectors. Noise in the micromechanical IR detectors can come from the detector itself, from the detector-environment interaction or from the readout. Microfabrication allows for batch fabrication of highly efficient transducers converting small temperature differences or heat fluxes into easily measurable output signals. While the reduced sizes and heat capacitances of thermal detectors improve the image resolution sensitivity, their usefulness as IR and THz detectors is governed by the influence of various noise sources. Detector's noise characteristics impose fundamental limitations to their performance. Limitations such as temperature fluctuation limited and background limited noise are applicable to all thermal IR and THz detector types and arise merely from the fact that all objects, depending on their thermal mass and degree of heat exchange with the environment, are subject to thermal fluctuations. These fluctuations, otherwise negligible in macroscopic object become significant noise source in case of highly thermally isolated microscopic detectors such as microbolometers or micromechanical thermal IR detectors.

Additional limitation, applicable to micromechanical IR and THz detectors only is spontaneous microscopic mechanical oscillation of suspended structures due to their

thermal energy ($k_B T$). For any of the potential readouts, these oscillations are indistinguishable from thermally-induced deformations and as such directly contribute to detector noise.

The fundamental limits to the performance of the micromechanical thermal detectors are intrinsic properties of the detectors and are, therefore, readout-independent. The fundamental performance limits are the background fluctuation limit and the temperature fluctuation limit. They arise from the fluctuations in the detector temperature that exist because of the dynamic nature of heat exchange between the detector and its environment. An ideal, noiseless, readout amplifies both the useful signal and the detector's intrinsic noise without distorting them or changing the signal-to-noise ratio. In practice, there are no ideal, noiseless readout methods; in best case, the readout decreases the inherent signal-to-noise ratio of the microcantilevers only minimally.

In order to obtain analytical expressions for noise limited figures of merit *NEP*, D^* and *NETD* we need to consider the expressions for those figures of merit defined above. From Equations 5a and 6, we obtain the expression for noise limited NEP_N

$$NEP_N = \frac{z_N}{\Delta z} P_0, \tag{22}$$

where z_N is the amplitude of deflections for particular noise mechanism and Δz is the amplitude of deflections due to signal. From Equations 7 and 22 we obtain the expression for noise limited normalized detectivity D^*_N

$$D_N^* = \frac{\Delta z}{z_N} \cdot \frac{\sqrt{A_d B}}{P_0}, \tag{23}$$

where $\Delta z / z_N$ is signal to noise ratio for particular noise mechanism. In order to obtain noise limited $NETD_N$, we will consider the signal-to-noise ratio, which can be obtained from Equation 20

$$\frac{\Delta z}{z_N} = \frac{\tau_0 A_d R(\omega) \left(\frac{dP}{dT} \right)_{\lambda_1 - \lambda_2}}{4F^2 z_N} T_t \tag{24}$$

If *NETD* is defined as the target temperature for which the signal to noise ratio equals unity and Equation 24 is used, the following expression is obtained

$$NETD_N = \frac{4F^2 z_N}{\tau_0 A_d R(\omega) \left(\frac{dP}{dT} \right)_{\lambda_1 - \lambda_2}} \tag{25}$$

The Equations 22, 23 and 25 are generalized expressions for noise limited *NEP*, D^* and *NETD* and take into account the tip displacement fluctuations resulting from contribution of different noise sources. These expressions are used in the subsequent sections to evaluate how different noise mechanisms influence the figures of merit.

4.1 Temperature Fluctuation Noise

All IR detectors that operate as transducers of incoming IR radiation into output signal are affected by temperature fluctuation noise due to continuous heat exchange at the

microscopic level (see Kruse [11, 57, 58]). In the case of micromechanical IR detectors, temperature fluctuation noise manifests itself as fluctuations of the detector tip displacement due to bimetallic effect. As discussed previously by Kruse [11, 57], the mean square magnitude of fluctuations in detector temperature can be derived from the fluctuation-dissipation theorem and is given by:

$$\left\langle \delta T^2 \right\rangle = \frac{k_B T^2}{C}, \tag{26}$$

where k_B is Boltzmann's constant and T is the temperature of the detector. The temperature fluctuation $\langle \delta T^2 \rangle$ of Equation 26 is the integration over all frequencies f, where $f = \omega/2\pi$. The frequency spectrum of temperature fluctuations is given by[11]

$$\left\langle \delta T_f^2 \right\rangle = \frac{4 k_B T^2 B}{G_T\left(1 + \omega^2 \tau^2\right)}, \tag{27}$$

where B is the measurements bandwidth and G_T is the total thermal conductance between the absorber and the environment. From Equation 27, it follows that the root mean square (rms) temperature fluctuation can be expressed as

$$\left\langle \delta T^2 \right\rangle^{1/2} = \frac{\sqrt{4 k_B B} T}{G_T^{1/2} \sqrt{1 + \omega^2 \tau^2}} \tag{28}$$

Figure 10 shows exemplary temperature fluctuation spectra calculated for a typical IR sensitive micromechanical detector using Equation 28.

It is important to note that the frequency dependence of temperature increase due to the useful signal (Equation 14) corresponds to the frequency dependence of temperature

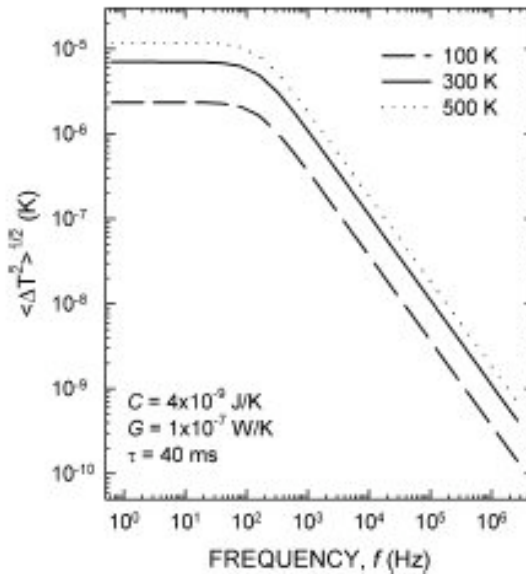

Figure 10 Spectral density of temperature fluctuation noise (rms values of temperature fluctuation)
The fluctuation amplitudes have been calculated using Equation 28 for three different temperatures

fluctuation due to the noise (Equation 28). Frequency dependence of fluctuations in displacement of the detector tip, *z,* due to temperature fluctuation noise is influenced by both the thermal and mechanical response of the detector. The expression for spontaneous fluctuations in displacement of the microcantilever caused by temperature fluctuations can be obtained from Equations 14, 17 and 28, where ΔT is substituted with $<\delta T^2>^{1/2}$

$$\left\langle \delta z_{TF}^2 \right\rangle^{1/2} = \frac{R(\omega) T \sqrt{4 k_B B G_T}}{\eta} \tag{29}$$

It can be seen from Equations 12a, 12b and 13 that, due to the linear dependence of Δz and ΔT, the signal-to-noise ratio, $\Delta z / <\delta z_{TF}{}^2>^{1/2}$, can be calculated as $\Delta T / <\delta T^2>^{1/2}$,

$$\frac{\Delta z}{\left\langle \delta z_{TF}^2 \right\rangle^{1/2}} = \frac{\eta P_0}{T \sqrt{4 k_B B G_T}} \tag{30}$$

As can be concluded from Equation 30, the total thermal conductance, G_T, defined as a sum of principal heat loss mechanisms, is the main design parameter affecting the ratio of the signal to temperature fluctuation noise in micromechanical infrared detectors In practice, the smallest total thermal conductance achievable is the radiative heat exchange between the detector and its surroundings.

It should also be noted that the signal-to-noise ratio as defined by Equation 30 is frequency-independent, even at $\omega\tau > 1$. Assuming the mechanical parameters provided in Table 2, the calculated spectral densities of spontaneous microcantilever fluctuations, $<\delta z_{TF}{}^2>^{1/2}$, due to temperature fluctuations in vacuum were plotted in Figure 11 (solid line marked TF).

Using the expressions for amplitude of fluctuations due to the temperature fluctuation noise $<\delta z_{TF}{}^2>^{1/2}$ (Equation 29) and corresponding signal to noise ratio $\Delta z / <\delta z_{TF}{}^2>^{1/2}$ (Equation 30), together with Equations 22, 23 and 25, we obtain the expressions for temperature fluctuation limited noise equivalent power NEP_{TF}

$$NEP_{TF} = \frac{T \sqrt{4 k_B B G_T}}{\eta}, \tag{31}$$

normalized detectivity D_{TF}^*

$$D_{TF}^* = \frac{\eta \sqrt{A_d B}}{T \sqrt{4 k_B B G_T}}, \tag{32}$$

and noise equivalent temperature difference $NETD_{TF}$

Table 2 Mechanical parameters for micromechanical infrared detector

	k (N/m)	m (kg)	Q	ω_0 (rad/s)	f_0 (Hz)
Air	0.01	4×10^{-12}	100	50265	7000
Vacuum	0.01	4×10^{-12}	500	56550	8000

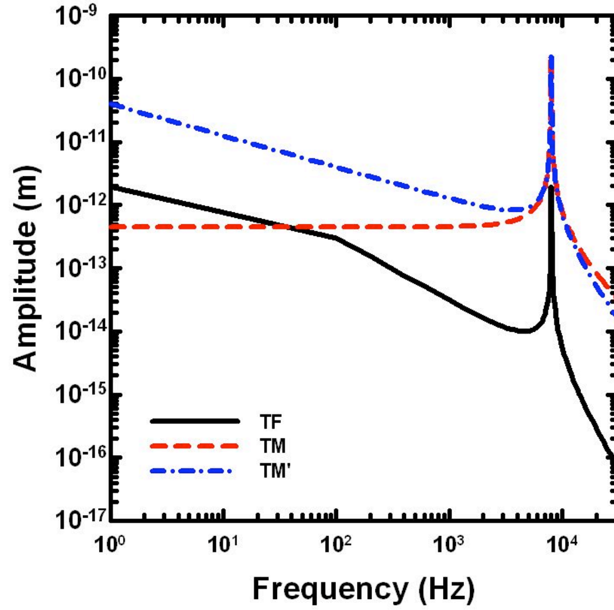

Figure 11 Spectral densities of temperature-fluctuation and thermomechanical noise

Solid line represents the spectral density if temperature-fluctuation noise. Dashed and dot-dashed lines represent the spectral densities calculated using the model of viscous damping and intrinsic friction mechanisms respectively. These plots have been obtained using Equations 29, 39 and 42.

$$NETD_{TF} = \frac{4F^2 T\sqrt{4k_B B G_T}}{\tau_0 \eta A_d \left(\frac{dP}{dT}\right)_{\lambda_1 - \lambda_2}}. \tag{33}$$

Figure 12 illustrates the dependence of D^*_{TF} on T and G_{T} plotted for different detector geometries. Figure 13 shows the plots of temperature fluctuation noise limit, $NETD_{\mathrm{TF}}$, for the detector analyzed in reference [14] calculated using Equation 33. Three plots correspond to three different detector temperatures 200, 300, and 400 K. The values of G_{rad} plotted in Figure 13 as vertical lines correspond to the conductance due to only radiative heat loss mechanism at three temperatures of 200, 300, and 400 K. These values of G_{rad} represent the ultimate thermal isolation limit (for the corresponding temperatures). Plots in both Figures 12b and 13 emphasize the importance of designing detectors with low thermal conductance G. However, in case of micromechanical detectors suspended over the substrate, conductance through the air G_{air} dominates the heat loss mechanism. As illustrated in Figure 13, values of thermal conductance close to the upper limit observed when operating at the atmospheric pressure, G_{air}, correspond to respectively high values of $NETD_{\mathrm{TF}}$. From Equations 14 and 27, it is apparent that one cannot separate the temperature fluctuation noise from the signal since both may have the same frequency components. Equation 29 might lead to thinking that the rms amplitude of oscillations in detector temperature could be minimized when operating at higher

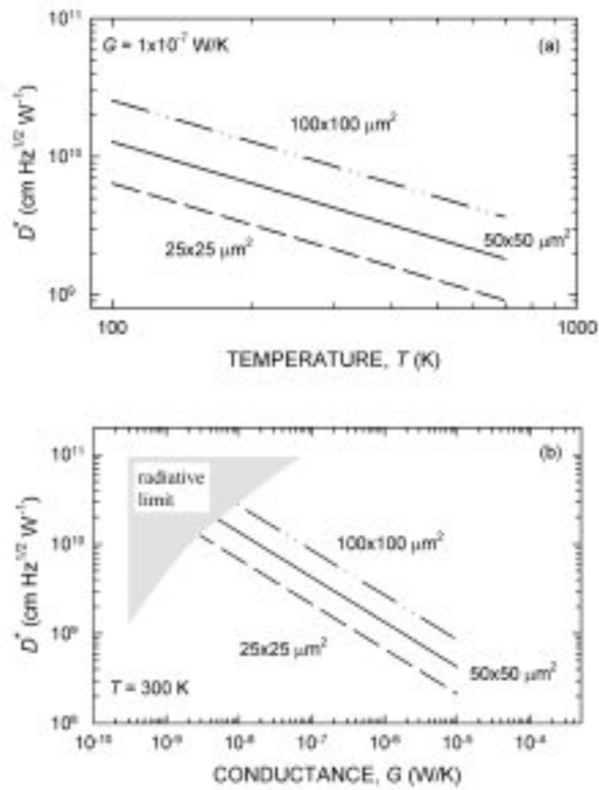

Figure 12 Temperature-fluctuation-noise-limited normalized detectivity D^* [54]

Two plots show D^* vs. temperature, T and conductance, G vs. temperature, T

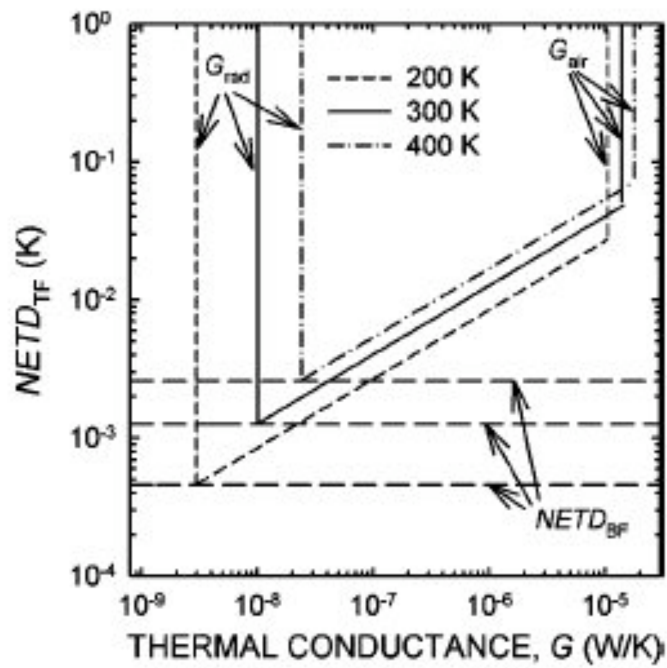

Figure 13 Noise Equivalent Temperature Difference vs. thermal conductance [14]

Calculated for three different temperatures: 200K, 300K and 400K

frequencies. However, consistently with the data experimentally observed by Datskos et al. in [14], and discussed earlier in Chapter 2, no improvement of the signal-to-noise ratio can be gained by operating at a microcantilever resonant frequency since both the noise and the signal peak at the resonance (see Figure 8)[15].

Equation 30 shows that it is crucial to minimize the heat exchange (minimize G_T) between the detector and the environment in order to minimize the temperature fluctuation noise and maximize the signal-to-noise ratio. If operating at atmospheric pressure, the dominant heat-loss mechanism is likely to be convection through the air. For this reason, traditional micromechanical IR detectors are kept at reduced pressure in an evacuated package.

Equation 33 further indicates that $NETD_{TF}$ can be improved with improved thermal isolation (lower G_T). It reaches its minimum for ideally isolated detectors, i.e. in case of purely radiative heat exchange. It may appear that the thermal isolation, i.e. decreasing the total thermal conductance, G_T also decreases the detector performance as it increases the magnitude of temperature fluctuations $<\delta T^2>^{1/2}$ i.e. noise, which is inversely proportional to $G_T^{1/2}$ (Equation 28). However, lower thermal conductance improves detector sensitivity $\Delta z/\Delta T$, which is inversely proportional to G_T, to even higher degree, hence improving the overall performance (Equation 17).

To offset the noise in micromechanical IR detectors originating from the ambient temperature fluctuations, techniques like "self-leveling" reported by Corbiel et al. [67] and Ishizuya et al.[30] and damping the mechanical energy by converting it into the AC current via the RC circuit formed by the detector's capacitance and damping resistor are developed [46].

4.2 Background Fluctuation Noise

Designing well thermally isolated detectors is the key for optimizing their performance. However, the degree of thermal isolation is always limited by the radiative heat exchange between the detector and its environment, since this type of heat dissipation cannot be prevented. As in case of other heat dissipation mechanisms, the temporal fluctuations in the radiative heat exchange cause temporal fluctuations in the detector temperature. Such fluctuations create the noise level commonly referred to as the background fluctuation noise. The background fluctuation limit, in the case of microcantilever thermal detectors, can be quantified in terms of microcantilever tip displacement, i.e. oscillations in z. Conventional uncooled detectors currently in use can only remotely approach the background fluctuation noise limit.

Since the background fluctuation noise can be regarded as the manifestation of temperature fluctuation noise when the radiative conductance is the principal heat loss mechanism, the expressions derived for NEP_{TF}, D^*_{TF} and $NETD_{TF}$ are still applicable. The only difference is that the total conductance G_T is replaced by the radiative heat conductance G_{rad}.

G_{rad} is obtained using the first derivative with respect to temperature of the Stephan-Boltzmann function.

$$G_{rad} = 4A\eta\sigma(T_B^3 + T_D^3)\,, \tag{34}$$

where T_B is the temperature of the background and T_D is the temperature of the detector. Using Equation 34, together with Equations 31, 32 and 33, we obtain the following expressions for NEP_{BF},

$$NEP_{BF} = \frac{\sqrt{16 k_B A_d B \sigma \left(T_B^5 + T_D^5\right)}}{\eta^{1/2}}, \qquad (35)$$

D^*_{BF}

$$D^*_{BF} = \frac{\eta^{1/2}}{\sqrt{16 k_B \sigma \left(T_B^5 + T_D^5\right)}} \qquad (36),$$

and $NETD_{BF}$

$$NETD_{BF} = \frac{4F^2 \sqrt{16 k_B B \sigma \left(T_B^5 + T_D^5\right)}}{\tau_0 \sqrt{A_d} \eta \left(\frac{dP}{dT}\right)_{\lambda_1 - \lambda_2}}. \qquad (37)$$

Background fluctuation noise is the bottom limit of noise as it cannot be affected by design optimization.

4.3 Thermo-Mechanical Noise

As discussed by Datskos et al., in addition to temperature fluctuation noise and background fluctuation noise, there exist noise sources unique to micromechanical IR detectors. A unique feature of micromechanical detectors is that, unlike other types of uncooled IR detectors, they are mechanical structures (oscillators) that can accumulate and store mechanical energy. When a micromechanical detector is in equilibrium in a thermal bath, there exists a continuous exchange of the mechanical energy accumulated in the detector and thermal energy of the environment. This exchange, governed by the fluctuation dissipation theorem [68, 69], results in spontaneous oscillation of the microcantilever so that the average mechanical energy per mode of cantilever oscillation is defined by thermal energy $k_B T$. Sarid [49] has described this noise source as ‘‘thermally induced lever noise.’’[14]

In the same work[14], Datskos et al. cite the analysis provided by Sarid [49] which involves the *Q*-factor of a vibrating microcantilever, its resonant frequency, ω_0 , and spring constant, *k*. While the *Q*-factor can be defined empirically as the ratio of the resonance frequency to the resonance peak width, Datskos et al. emphasize the importance of knowing the exact mechanisms of microcantilever damping for evaluation of the thermomechanical noise spectrum. They have therefore reviewed and compared work of several groups who have attempted to develop analytical models to describe thermo-mechanical noise and energy dissipation in nanomechanical and micromechanical resonators [70]. It is now known that the intrinsic losses in the microcantilever material such as viscoelastic losses [70] represent an important mechanism of the mechanical energu dissipation. These losses have been evaluated by Cleland and Roukes [70] who used the Zener model for anelastic solids [71-73]. Phonon scattering within the

micromechanical system due to defects within the solid or at the interface between the solid and vacuum has also been considered [14, 74].

Zener et al. demonstrated the effects of thermo-elastic internal friction in the late 1930's by measuring the frequency response spectrum of a copper reed over a wide frequency range[71-73]. It has been observed that the responses are adiabatic at high frequencies and isothermal at low frequencies. The measured internal friction was observed to be the highest at a frequency $f = (\pi/2)(D/w^2)$ where D is the thermal diffusivity and w is the reed width. It has been determined that the internal friction was related to the heat flow across the reed.

If we assume isotropic solid and diffusive thermal phonons, the interaction between the acoustic mode and the thermal phonon bath can be described by the coefficient of thermal expansion of the material. Thermo-elastic solid, when excited into motion, reaches a nonequilibrium state and the coupling of the strain field to the temperature field gives rise to an energy dissipation mechanism that allows the system to relax back to equilibrium [75]. Lifshitz and Roukes [75] investigated the thermo-elastic damping process as a dissipation mechanism in small scale resonators and concluded that the thermo-elastic damping is a significant source of dissipation down to the nanometer scale.

Yasumura et al. [76] have investigated the Q-factors in small-scale silicon and silicon nitride resonators whose thicknesses varied from a few μm to a few hundred nm. They have determined that the Q-factor decreased monotonically as thickness decreased and that the effect of thermoelastic dissipation became negligible. Houston *et al.* [77], however, found that, at room temperature, thermo-elastic dissipation becomes a significant loss mechanism.

Datskos et al. conclude that the evident discrepancy with the conclusion of Lifshitz and Roukes[75] can be explained by the fact that the thermo-elastic dissipation is frequency dependent[14]. For a microcantilever with thickness t, the frequency, f_{TE}, that maximizes thermo-elastic dissipation is given by[76]

$$f_{TE} = \frac{\pi}{2}\frac{g}{\rho C t^2}, \tag{38}$$

where g is the thermal conductivity of the material and ρ is the density. If the thickness of the microcantilever is varied while keeping the length constant, the resonant frequency will shift. This shift in frequency that would, in turn, maximize the thermo-elastic dissipation[77] and, therefore, the ratio t/l will become significant to the point it has to be taken into account. In fact, increasing resonance frequency of the microcantilever by decreasing its the length, causes the thermo-elastic dissipation to be shifted in a frequency region dominated by other processes (phonon–phonon limit) [77].

Datskos et al. point to the work of White and Pohl [78] who have measured the low-temperature internal friction of thin a-SiO_2 films with thicknesses ranging from 0.75 to 1000 nm in attempt to determine whether the spectral distribution of the low energy excitations, believed to exist in all amorphous solids, is caused by strong interactions between defects. Their findings indicated that the low temperature internal friction of these films is nearly identical to that of bulk a-SiO_2 and they concluded that interactions limited to distances less than 0.75 nm can be viewed as intermolecular forces [14].

Sarid's thermo-mechanical model assumes viscous nature of the damping in microcantilever oscillations[49]. The assumption of predominantly viscous damping is valid for microcantilevers operating in air or water and, therefore, justified for micromechanical structures utilized as probes in scanning probe microscopy. In the case of a microcantilever operating in a viscous medium, such as air or water, the damping force is proportional to the linear velocity of microcantilever. The resulting noise spectrum can be expressed as[79]

$$\left\langle \delta z_{TM}^2 \right\rangle^{1/2} = \sqrt{\frac{4k_B TB}{Qk} \frac{\omega_0^3}{\left(\omega_0^2 - \omega^2\right)^2 + \frac{\omega^2 \omega_0^2}{Q^2}}} \tag{39}$$

According to the Equation 39, the noise density is frequency-independent for the frequencies well below the mechanical resonance frequency, ω_0 (i.e. $\omega << \omega_0$). At these frequencies, the rms of the microcantilever tip displacement due to thermo-mechanical noise is given by[49]

$$\left\langle \delta z_{TM}^2 \right\rangle^{1/2} = \sqrt{\frac{4k_B TB}{Qk\omega_0}}, \tag{40}$$

However, at the resonance (i.e., $\omega = \omega_0$) [49],

$$\left\langle \delta z_{TM}^2 \right\rangle^{1/2} = \sqrt{\frac{4k_B TBQ}{k\omega_0}}. \tag{41}$$

Equation 39 is commonly used to estimate thermo-mechanical noise limits of a micromechanical IR detector[3, 31, 80].

Since micromechanical IR and THz detectors usually operate in vacuum (at pressures below 10 mTorr) one should consider the dependence of both Q and ω_0 on pressure. In fact, Q typically changes from about 10–20 in air to 100 and above in vacuum. Figure 11 shows the spectral density of thermomechanical noise (plot TM). These plots have been obtained using Equation 39 and mechanical properties in Table 2.

As emphasized in [14], the higher Q-factors of microcantilevers operating in vacuum are defined mostly by the mechanisms of intrinsic friction and inelastic damping[79, 81] in the microcantilever material. In the same work, Datskos et al. list a variety of mechanisms which include thermo-elastic dissipation, motion of defects, and phonon–phonon scattering[74, 82] as sources of internal friction. They, however, proceed to stating that while the internal friction is a bulk effect, surface effects may dominate in nanometer thick structures.[78] Therefore, they question the accuracy of the model of thermomechanical noise based on the assumption of viscous damping in the case of microcantilevers with microscopic dimensions, such as those used as IR detectors [79, 81].

Therefore, Datskos et al. offer an alternative model provided by Majorana *et al.*[79] who investigated an alternative model of thermo-mechanical noise that accounts for internal friction processes rather than viscous damping. In this model, the thermo-mechanical noise spectrum is expressed as [79, 81]:

$$\left\langle \delta z_{TM'}^{2} \right\rangle^{1/2} = \sqrt{\frac{4k_B TB}{Qk\omega} \frac{\omega_0^4}{\left(\omega_0^2 - \omega^2\right)^2 + \frac{\omega_0^4}{Q^2}}} \tag{42}$$

It can be seen from Equation 42 that the thermo-mechanical noise density follows a $1/f^{1/2}$ dependence below the resonant frequency when the damping is due to intrinsic friction processes. This is also apparent in Figure 11, (plot TM') which is plotted using Equation 42 and mechanical detector properties from Table 2. The analysis of Equations 39 and 42 shows that, regardless of the dissipation mechanism, the off-resonance thermomechanical noise is lower in the case of microcantilevers with a higher Q-factor and higher k. It should be emphasized that, while predictions based on Equation 39 are often reported in the literature [3, 80, 82], the noise density calculated according to the two alternative models may substantially differ from each other at low frequencies [69, 79, 81]. Furthermore, the intrinsic friction model predicts the noise at low frequencies to be independent of the microcantilever resonant frequency assuming fixed stiffness, k. By contrast, the viscous damping model predicts that the low frequency noise of a microcantilever detector can be decreased by increasing its resonance frequency, even without changing its stiffness. Therefore, it is critical to know the actual mechanisms of mechanical dissipation in the microcantilever detector for analyzing thermo-mechanical noise of a micromechanical detector in the frequency range relevant to real-time IR imaging[14].

The expression for the rms amplitude of tip displacement Equation 40 (in case of viscous damping), along with Equations 17, 22, 23 and 25 can be used to obtain the thermo-mechanical noise limited values of *NEP*, D^* and *NETD*. NEP_{TM} becomes:

$$NEP_{TM} = \frac{1}{R(\omega)} \sqrt{\frac{4k_B TB}{Qk\omega_0}}, \tag{43}$$

D^*_{TM} becomes:

$$D_{TM}^{*} = R(\omega) \sqrt{\frac{Qk\omega_0 A_d}{4k_B T}}, \tag{44}$$

and $NETD_{TM}$ becomes:

$$NETD_{TM} = \frac{4F^2}{\tau_0 A_d R(\omega) \left(\frac{dP}{dT}\right)_{\lambda_1 - \lambda_2}} \sqrt{\frac{4k_B TB}{Qk\omega_0}}. \tag{45}$$

Using the alternative model (Equation 42) that takes the damping caused by intrinsic friction into account, the frequency-dependent rms noise can be predicted. This frequency dependence, somewhat complicates the estimate of the corresponding $NETD_{TM}$. In addition to a measurements bandwidth, an assumption should be made with respect to the frequency. Off resonance, the value of $NEP_{TM'}$ becomes:

$$NEP_{TM'} = \frac{1}{R(\omega)} \sqrt{\frac{4k_B TB}{Qk\omega}} \tag{46}$$

$D^*_{TM'}$ becomes:

$$D^*_{TM'} = R(\omega)\sqrt{\frac{Qk\omega A_d}{4k_B T}} \tag{47}$$

and $NETD_{TM'}$ becomes:

$$NETD_{TM'} = \frac{4F^2}{\tau_0 A_d R(\omega)\left(\frac{dP}{dT}\right)_{\lambda_1-\lambda_2}}\sqrt{\frac{4k_B TB}{Qk\omega}} \tag{48}$$

In practice, it is very important to determine which of the two thermomechanical noise models applies to a particular type of micromechanical thermal detector. Nevertheless, despite the differences, both models agree on the importance of having stiffer microcantilevers (higher k) and higher Q-factors.

Figure 11 displays the cantilever noise spectra. Noise originating from both temperature fluctuation (solid lines) and thermo-mechanical noise (dashed lines) is included. The graph features theoretical predictions for both alternative ways of calculating thermo-mechanical noise. Those include assuming the viscous damping (dotted line) and assuming the energy is lost due to internal friction processes (dashed line).

4.4 Readout Noise

A portion of the total noise can be attributed to the readout used to quantify the deformations of the mechanical infrared detectors. Some of the readouts implemented include piezoresistive readout, capacitive readout and optical readout (both using the photodetector and CCD).

4.4.1 Piezoresistive Readout

The following analysis will consider a simple, rectangular, bimaterial piezoresistive detector with geometry as defined in [83] (Figure 14). A piezoresistive IR detector measures thermally induced stress in the structure. Through piezoresistive effect, the stress is converted to change in detector resistance ΔR, which is in turn, converted to voltage signal through a Wheatstone bridge. The two main noise sources in piezoresistive readout are Johnson Noise and Hooge (or flicker) Noise. Johnson noise is caused by the random motion of mobile carriers in resistive materials at finite temperature T. It is independent of frequency and depends only on the temperature and resistance of the piezoresistive element. The voltage fluctuations are given by:

$$\left\langle \delta v_{JN}^2 \right\rangle = 4k_B TRB \tag{49}$$

where T is the temperature of the detector, R is the resistance of the detector and B is the bandwith. At low frequencies, Hooge noise is dominant and it follows $1/f$ dependence.

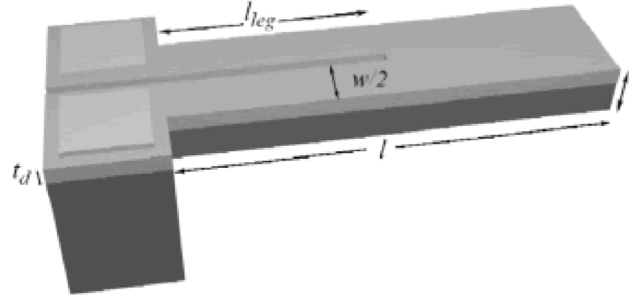

Figure 14 Illustration of piezoresistive IR detector

Two electrodes are connected to two separated deformable legs so that the current path goes through them. When the legs deform due to temperature increase, the resistance will change and the change can be detected by monitoring the current

The source of it is currently still not fully understood. However, empirical formula derived by Hooge [84] indicates that

$$\left\langle \delta v_{HN}^2 \right\rangle = \frac{\alpha V^2 B}{Nf} \tag{50}$$

where α is Hooge's factor which is not constant but a dimension-independent parameter ranging from 10^{-7} to 10^{-3}[84], V is the bias voltage of the piezoresistive element, and N is the number of carriers.

Harley et al. plotted a typical piezoresistive cantilever readout noise spectrum, which is displayed in Figure 15. It is apparent that lower frequencies follow the 1/f dependence of Hooge's noise and asymptotically approaching the constant Johnson noise at higher frequencies.

In order to utilize the above-defined formulas for noise limited figures of merit, the displacements of detector's tip equivalent to above defined noise fluctuations need to be defined. Hansen et al. [85] and Harley et al.[83] define a transfer function of a piezoresistive detector S_{PD} which relates the tip displacement Δz to the voltage signal Δv_{PD} generated by the piezoresistive detector such that $\Delta v_{PD} = S_{PD}\,\Delta z$. The transfer function is given by

$$S_{PD} = \frac{6k\pi_{eff} V (l - \frac{l_{leg}}{2})}{wt^2}, \tag{51}$$

where k is the spring constant of the detector, π_{eff} is the effective piezoresistive coefficient, V is the voltage across the detector, l is the detector total length and l_{leg} is the length of the piezoresistive legs of the detector, w is the detector width and t is its thickness.

Using the Equations 49, 50 and 51, the following expressions are obtained:

$$\left\langle \delta z_{JN}^2 \right\rangle = \frac{1}{S_{PD}} \left\langle \delta v_{JN}^2 \right\rangle = \frac{2wt^2 k_B TRB}{3k\pi_{eff} V \left(l - \frac{l_{leg}}{2} \right)} \tag{52}$$

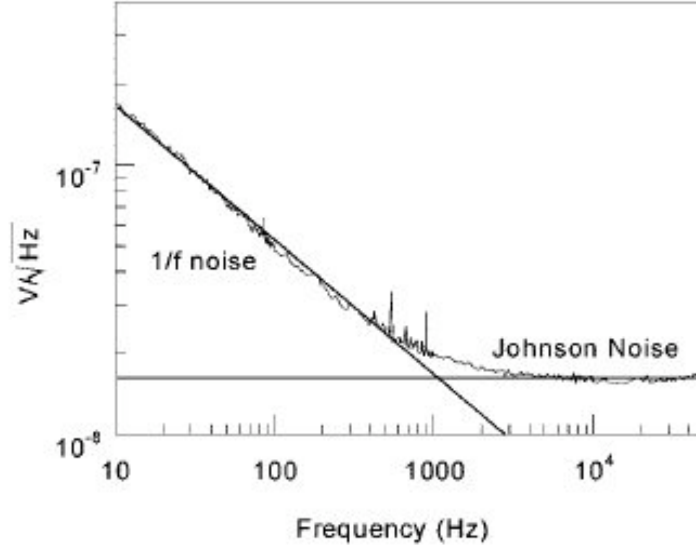

Figure 15 Readout noise spectrum for piezoresistive cantilevers

and

$$\left\langle \delta z_{HN}^2 \right\rangle = \frac{1}{S_{PD}} \left\langle \delta v_{HN}^2 \right\rangle = \frac{wt^2 \alpha VB}{6k\pi_{eff} Nf\left(l - \frac{l_{leg}}{2}\right)} \tag{53}$$

From here, using the Equations 17, 22, 23 and 25, can obtain piezoresistive readout noise-limited *NEP*, *D** and *NETD*. We will derive expressions for both Johnson noise and Hooge noise, having in mind that the former will be dominant at higher frequencies and latter at lower frequencies.

In case of Johnson noise, the following expressions define

$$NEP_{JN} = \frac{1}{R(\omega)} \sqrt{\frac{2wt^2 k_B TRB}{3k\pi_{eff} V\left(l - \frac{l_{leg}}{2}\right)}}, \tag{54}$$

$$D_{JN}^* = R(\omega) \sqrt{\frac{3k\pi_{eff} Vl\left(l - \frac{l_{leg}}{2}\right)}{2t^2 k_B TR}} \tag{55}$$

and

$$NETD_{JN} = \frac{4F^2}{\tau_0 R(\omega)\left(\frac{dP}{dT}\right)_{\lambda_1 - \lambda_2}} \sqrt{\frac{2t^2 k_B TRB}{3k\pi_{eff} V\left(l - \frac{l_{leg}}{2}\right) wl^2}} \tag{56}$$

where A_d has been approximated by lw.

In the case of Hooge noise, the following expressions define

$$NEP_{HN} = \frac{1}{R(\omega)}\sqrt{\frac{wt^2 \alpha VB}{6k\pi_{eff} Nf\left(l - \frac{l_{leg}}{2}\right)}}, \tag{57}$$

$$D^*_{HN} = R(\omega)\sqrt{\frac{6k\pi_{eff} Nfl\left(l - \frac{l_{leg}}{2}\right)}{t^2 \alpha V}} \tag{58}$$

and

$$NETD_{HN} = \frac{4F^2}{\tau_0 R(\omega)\left(\frac{dP}{dT}\right)_{\lambda_1 - \lambda_2}} \sqrt{\frac{t^2 \alpha VB}{6k\pi_{eff} Nfwl^2\left(l - \frac{l_{leg}}{2}\right)}}. \tag{59}$$

4.4.2 Capacitive Readout

Capacitive readout utilizes the change of capacitance of detectors due to their deformation. When detector's temperature increases, the detector will be deformed due to the bimetallic effect, as the other types of micromechanical infrared detectors. Since a part of the detector is at the same time one of the capacitor's plates, this deformation will change the distance between the plates, inducing the change in capacitance. This capacitance change will be detectable and proportional to the temperature change [46, 86].

The main sources of noise in capacitive readout are the Johnson's noise, Hooge (flicker) noise and the noise due to the leakage current of the diode in the biasing circuit and $k_B T/C$ noise in the charge integration capacitors [46, 86].

4.4.3 Optical Readout

As mentioned in Chapter 1, the term *optical readout* refers to two different configuration. One configuration is the optical cantilever readout identical to the one utilized in Atomic Force Microscopy [49] and is the most suitable for single (spot) detectors. Second configuration is the optical readout using charge-coupled device (CCD) utilized for simultaneously probing deflections of multiple detectors in two-dimensional arrays and is mostly suitable for infrared imaging. We will address some of the noise issues for both of them.

4.4.3.1 PSD Readout

In this approach, a laser beam is focused on a microcantilever tip. This configuration is very similar to that employed in the atomic force microscope[49]. The reflected beam deflects in accordance to microcantilever bending. The magnitude of microcantilever deformation (bending) can be quantified by directing the reflected spot onto a PSD that

consists of two photodiodes: PD_1 and PD_2. Datskos et al. provided an extensive analysis of the noise introduced into the system which uses this type of readout[14]. They have considered displacement, Δz, of the bimaterial microcantilever tip with length l due to thermal IR radiation incident upon it. The additional input parameters for this calculation include the probing laser beam power, P_l and the distance between the microcantilever and the photodetector L. Microcantilever deflection causes redistribution of the laser beam power incident upon each of the two photodiodes. If a square (i.e., non-Gaussian) spatial distribution of power within the laser beam is assumed, the difference between the power of light fallen upon each of the two halves of the photocell can be approximated as [49]

$$\Delta P_l = P_l \frac{4L}{ld} \Delta z \tag{60}$$

where d is the diameter of the light spot projected on the photocell. This difference in illuminations of the two photodiodes leads to a difference, Δi, between photo-currents of the two halves of the photocell, [49]

$$\Delta i = \gamma P_l \frac{4L}{ld} \Delta z \tag{61}$$

where γ is the photocell responsivity in A/W. Equation 61 shows that the gain of the optical read-out is proportional to the laser power, P_l , as well as the geometric factor of the photo cell $\beta = 4L/l$, and inversely proportional to the diameter, d, of the light spot projected on the photocell. A differential amplifier is connected to the two halves of the bi-cell[14]. The amplifier produces the output current, i_S, proportional to Δz,[49]

$$i_S = \gamma P_l \frac{4L}{ld} \Delta z = \frac{4\gamma L P_l}{ld} P_0 R \tag{62}$$

Therefore, the thermal infrared power P_0 falling on the microcantilever can be obtained indirectly by measuring the photocurrent i_S, if the photocell responsivity γ, the distance L, the laser power P_l, the microcantilever length l, the diameter of the light spot projected on the photocell d and of the microcantilever responsivity R are known. If the responsivity, R, is determined independently using a calibrated source, the incident infrared power, P_0, is

$$P_0 = \frac{i_S ld}{4\gamma L P_l R} \tag{63}$$

Datskos et al. define the total responsivity of the optically-probed micromechanical IR detector as the current measured at the output of the differential photocell divided by the incident infrared radiation power: $R_{ol} = i_S / P_0$. The relationship between R_{ol} and R is then given by[14]

$$R_{ol} = \frac{\gamma P_l \beta}{d} R \tag{64}$$

Equation 64 shows the dependence of the total responsivity R_{ol} on the optical readout parameters.

Datskos et al. emphasize that optical readout can inevitably add to the inherent noise of the micromechanical detector, although the added noise can be very small. Sarid[49]

identified five main sources of noise in an optical readout detector system. The noise sources are (i) optical pathlength drift, (ii) Johnson noise in the photodetector, (iii) laser phase noise, and (iv) shot noise in the photodetector due to the statistical nature of the rate of arrival of the laser photons at the photodetector. Moreover, microcantilever deflections both in response to the measured IR radiation and temperature fluctuation or thermo-mechanical noise are amplified by the optical read out by a factor of β. According to Sarid,[49] low frequency components of laser phase noise are reduced greatly at the differential amplifier due to good common mode rejection. Similarly, optical pathlength changes are an insignificant noise source since they do not affect the differential signal in the direction perpendicular to the laser beam. Therefore, the most important mechanisms of noise introduced by the optical readout are the Johnson noise and the photodetector shot noise[14].

Johnson noise always exists in electrically resistive materials. The mean square noise current $\langle i_{JN}^2 \rangle$ from each photodetector is[49]

$$\left\langle i_{JN}^2 \right\rangle = \frac{4k_B TB}{R} \tag{65}$$

where R is the photodetector resistance. The differential amplifier effectively doubles the noise by adding in quadrature the mean square noise from the two photocells. Sarid,[49] however, states that the Johnson noise contribution is much smaller as compared to photodetector shot noise. Photodetector shot noise is sometimes referred to as the light-source shot-noise, since it reflects an intrinsic feature of any light. Photonic shot noise is related to the statistical nature of the rate of arrival at the photodetectors of the laser photons. This phenomenon is well-established and is manifested as fluctuation of the current output in the photodetector[49]

$$\left\langle \delta i_{SN}^2 \right\rangle = q\gamma BP_l \tag{66}$$

where $\langle \delta i_{SN}^2 \rangle$ is the mean square fluctuation of photo-current in the differential photodetector due to photonic shot noise and q is the charge of an electron. Using the relationship between a photodetector output current and a microcantilever tip displacement given by Equation 62 along with the amplitude of noise oscillations given by Equation 66, the rms displacement of the microcantilever tip which would output the amplitude of noise equivalent to the amplitude of noise provided by the shot noise can be expressed as:

$$\left\langle \delta z_{SN}^2 \right\rangle^{1/2} = \frac{d}{\beta}\sqrt{\frac{qB}{\gamma P_l}} \tag{67}$$

Equation 67 shows the dependence of rms tip displacement (due to photon shot noise) on the optical readout parameters.

Using the Equations 22, 23 and 25, we obtain the values of NEP_{SN}, D^*_{SN} and $NETD_{SN}$. NEP_{SN} becomes:

$$NEP_{SN} = \frac{d}{\beta R(\omega)}\sqrt{\frac{qB}{\gamma P_l}}, \tag{68}$$

D^*_{SN} becomes:

$$D^*_{SN} = \frac{\beta R(\omega)}{d}\sqrt{\frac{\gamma P_l A_d}{q}}, \quad (69)$$

and $NETD_{SN}$ becomes:

$$NETD_{SN} = \frac{4F^2 d}{\tau_0 A_d \beta R(\omega)\left(\frac{dP}{dT}\right)_{\lambda_1-\lambda_2}}\sqrt{\frac{qB}{\gamma P_l}} \quad (70)$$

4.4.3.2 CCD Readout

Due to many different readout configurations, it is hard to define a comprehensive theory for calculating the noise contribution by the readout. Noise in this configuration can originate from both the illumination source and the CCD[31]. Illumination source adds noise through fluctuation in the light intensity. It can be minimized using the stabilization feedback techniques. The noise from the CCD can originate from the dark current and from digitization of the CCD output voltage. For example, an 8 bit CCD will have an error of the order of 1/256 = 0.004. The lowest limit of CCD shot noise in the detection process is equal to $1/N^{-1/2}$ where N is the full well capacity of CCD pixels[31].

4.5 Total Noise

Since the Noise Equivalent Temperature difference is the most commonly used parameter in infrared imaging community, it is useful to define a single parameter that would most properly describe the performance (i.e. noise) of the detection or imaging system as a whole. Considering all the fundamental noise sources described above, we obtain a generalized expression for the total noise equivalent temperature difference, $NETD_T$:

$$NETD_T = \frac{4F^2\sqrt{\langle\delta z^2_{TF}\rangle + \langle\delta z^2_{BF}\rangle + \langle\delta z^2_{TM}\rangle + \langle\delta z^2_{RO}\rangle}}{\eta\tau_0 A_d\left(\frac{dP}{dT}\right)_{\lambda_1-\lambda_2} R(\omega)} = \sqrt{NETD^2_{TF} + NETD^2_{BF} + NETD^2_{TM} + NETD^2_{RO}} \quad (71)$$

Total noise equivalent power, NEP_T can be obtained as:

$$NEP_N = \frac{\sqrt{\langle\delta z^2_{TF}\rangle + \langle\delta z^2_{BF}\rangle + \langle\delta z^2_{TM}\rangle + \langle\delta z^2_{RO}\rangle}}{\Delta z} P_0 = \sqrt{NEP^2_{TF} + NEP^2_{BF} + NEP^2_{TM} + NEP^2_{RO}} \quad (72)$$

While the total normalized detectivity D^* can be extracted from NEP_T using the Equation 7.

RO in Equations 71 and 72 stands for the "optical-readout". In order to obtain the *NETD* value for the microcantilever thermal detector we should consider the contribution to *NETD* of all the terms in Equation 71. In order to evaluate Equation 71, appropriate values of the parameters need to be chosen.

4.6 Summary

Figures of merit allow us to assess, quantify, and compare the performance of various IR detectors, especially focal plane arrays (FPAs). A number of parameters (figures of

merits) have been introduced over the years and are used to characterize different types of IR detectors. Although some figures of merit are more informative than others, the explicit and implicit assumptions made should always be kept in mind. As the uncooled thermal detectors develop, defining parameters that are both applicable to thermal detectors and consistent with parameters used to describe cooled photon detectors becomes a challenge[54]. In the previous part of this dissertation, a detailed analysis of figures of merit that apply to a class of micromechanical uncooled thermal detectors has been provided. Those were the noise equivalent power, *NEP*, normalized detectivity, *D** and noise equivalent temperature difference, *NETD*. These parameters will be used and refered to in the following chapters.

We have shown that the detector intrinsic noise often limits the performance of uncooled IR systems. All thermal IR detectors are subject to spontaneous temperature fluctuations resulting from the fundamental mechanisms of heat exchange and dissipation. These heat exchange and dissipation mechanisms impose two important fundamental limits to thermal IR detector performance, commonly referred to as the background fluctuation noise limit and the temperature fluctuation noise limit. In addition, micromechanical IR detectors exhibit spontaneous oscillations in a wide range of frequencies well below their fundamental resonance frequency due to a combination of their nonzero thermal energy and intrinsic mechanical losses. Although these fundamental limits are readout-independent, they do depend on several detector properties. In addition to these kinds of noises, that are characteristic of all mechanical infrared detectors, noise specific for different readout mechanisms needs to be taken into account.

The performance of a thermal IR detector can reach the absolute theoretical limit when the detector is so isolated from its surrounding thermally that the radiation exchange between the detector and its surrounding becomes the dominant heat loss mechanism. Although it is possible to almost infinitely reduce the thermal conductance between the detector and the environment, this would also have a negative impact on the thermal response time, which is inversely proportional to the thermal conductance. Thermal IR detector optimization therefore inevitably involves a tradeoff between an acceptable time-constant and their sensitivity. Since the thermal response time is directly proportional to the heat capacity, the limitations of this tradeoff can be eliminated in part by reducing the heat capacity of the detector.

By observing the variables in the expressions for noise-limited parameters, since the *NETD* has become the most widely used parameter for comparing detector performance, it is apparent that improvements to the detector performance and bringing them closer to current commercial (microbolometer-based) uncooled detectors can be achieved by modifying the detector geometry and types of materials. Changing the detector geometry can influence the detector area, its spring constant, thermal conductance, resonant frequency. These parameters along with others such as the absorption coefficient can also be influenced by changing the types of materials used. This dissertation will attempt to analyze the possibilities for changes to detector geometries and choice of materials to favorably influence the overall detector performance. The improved performance will be

compared to the performance parameters of commercial uncooled imagers and detectors in order to investigate the viability of using MEMS based IR detectors commercially. If the performance comparable to conventional uncooled imagers is achieved, this will prove the viability of the approach and allow capitalizing on many of MEMS-based IR detectors advantages. The advantages are numerous and include simplified microfabrication process, improved robustness and reliability, higher yield and ultimately significantly reduced cost of a final product.

Chapter 5

State of the Art

In this section we analyze performance of several different uncooled micromechanical IR detectors. We provide a simplified illustration of their design along with reported values for figures of merit and images where they were available. Since there is still no real convention defining generally required figures of merit, not all publications reported the same figures of merit. Also, theoretically predicted *NETD* is the total *NETD* calculated for the optimal case. Some authors have also experimentally measured total *NETD* and those have been included values where available. Detector size usually refers to the size of the reflector/absorber (Figure 2).

The design reported by Ishizuya from Nikon Corporation [30], shown in Figure 16, employs the "self-leveling" design which minimizes detector spontaneous oscillations due to temperature fluctuations. Each of its legs contains two bimaterial sections. The section closer to the absorber is the one that provides deflection due to the incoming IR radiation. The bimaterial section closer to the anchoring points provides deflection for cancellation of temperature fluctuation effects. Bimaterial regions are of the same length, and in case of changes in the ambient temperature both the sensing bimaterial region and the noise-canceling bimaterial region will deflect by the same magnitude. This will, in present configuration, cancel the effect of ambient temperature fluctuations and deflections of the sensing bimaterial region. This detector also features a reflector designed to provide improved reflection of the readout light as well as an optical resonant cavity within the detector, rather then between the detector and the substrate. Detector size is 55 x 55 μm and it is used in a 160 x 120 focal plane array. It is made of 300 nm thick SiN_x with 300 nm thick Al coating in bimaterial regions. Reported sensitivity for this structure is about 2.8 mV/K. Image obtained using array of these detectors is shown in Figure 17.

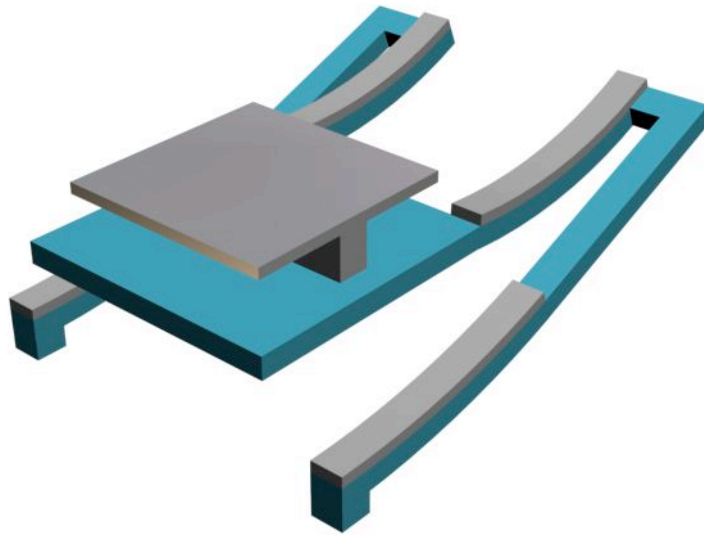

Figure 16 Detector designed by Nikon
This detector features multiple bimaterial regions for the purpose of temperature-fluctuation minimization mechanism as well as a flat reflector on top serving both for reflection and to form an optical resonant cavity.

Figure 17 IR image reported by Nikon [30]

The design reported by Zhao et al. [31], displayed in Figure 18, features a comb-like bimaterial detector. Comb-shaped pattern of protrusions is present on both bimaterial absorber and the thermally isolating legs. The detectors are tiled in such a way that fingers form head on each detector form inter-digitated pattern with non-movable fingers on the legs of adjacent detector. The readout is based on the principle of deformable diffraction grating. As in all optical readouts of FPAs, the read-out light illuminates the array. When the absorber moves, diffraction pattern of the reflected light changes proportionally to the vertical displacement between absorber and legs of adjacent detectors. Reflected light passes through the first of the two lenses, which performs a spatial Fourier transform. The light subsequently passes through the pinhole where only the zeroth order of the diffraction is passed through and finally through the second of the two lenses that performs inverse Fourier transform reconstructing the whole array based only on the first order diffraction. The detector is 100 x 200 μm in size. It is made of 1 μm thick SiN_x with a 500 nm Au layer on top of that forming bimetallic structure. Reported thermomechanical sensitivity for this structure is about 110 nm/K, response time τ is 80 ms, predicted *NETD* is 6.6 mK while the experimentally measured *NETD* was 2-5 K. 8-bit camera has been used in the readout. Image obtained using this array is displayed in Figure 19.

Micromechanical detector with a capacitive readout, developed by Multispectral Imaging, Inc., is a multi-layer structure whose layers include SiO_2 and SiON as well as layer with an aluminum alloy layer on the bottom of the bimaterial portion of the legs [46]. In his configuration, the absorber will deflect upward with the increase in temperature. Figure 20 shows the simplified illustration of this configuration. The deformation induces a measurable capacitance change proportional to the magnitude of temperature increase. Sections of the legs closer to the anchoring points are thermally isolating. For electrical connection to the substrate electronics, the whole detector has been covered with a very thin layer of TiN. The structure is a multi-layer thin film stack with a vacuum gap to create a quarter wavelength optical cavity. The achieved IR absorption is from 80 to 100% for different deflections. The fabricated 160 x 120 arrays had 50 μm pitch. These detectors have predicted response time τ of 9.8 ms and predicted total NETD of 18 mK.

The pneumatic detector with a tunneling readout is the infrared sensor reported by Kenny[43]. It is a shallow structure displayed in Figure 21 containing a gas trapped and sealed inside a chamber between two SiN_x membranes. When the incident radiation is absorbed by a porous SiN_x membrane in the middle of the chamber, the temperature of the membrane increases, increasing the temperature of the gas. The gas temperature-increase causes the rise in pressure of the gas inside the chamber, causing the gas to expand, pushing the membranes outward. This deformation will change the distance between the electrode on the membrane and the tip. As in the Scanning Tunneling Microscope (STM), when there is a voltage bias between the tip and the membrane, the tunneling current depends exponentially on the distance between the two. The dimensions of a gas volume are 1.7 mm x 1.7 mm x 0.4 mm. The membranes are made of SiN_x and are 700 nm thick. One of the membranes, the one facing the tip, is coated with 200 nm thick Au layer and connected to the bias voltage electrode (Figure 20). The reported signal to noise ratio of this detector is $27/Hz^{-1/2}$ and reported *NEP* is

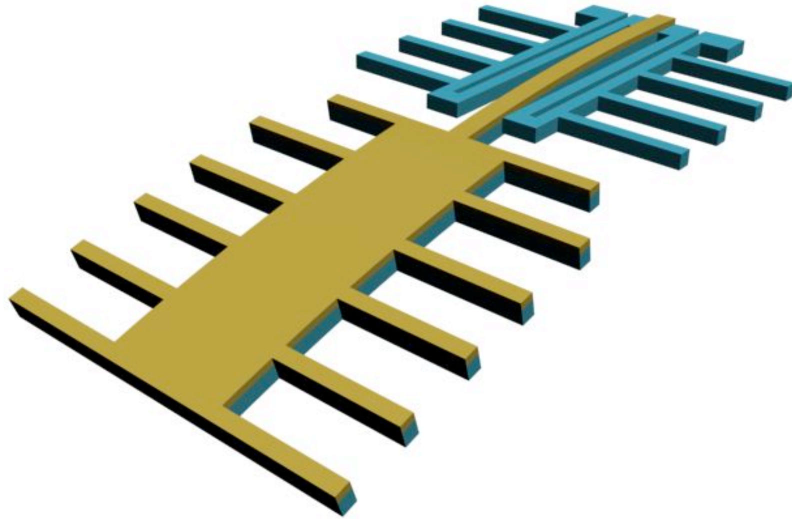

Figure 18 Bimaterial detector with comb-like structure
Inter-digitted fingers of the detector help change the interference pattern used to reconstruct the image

Figure 19 IR image reported by Zhao et al. [31]

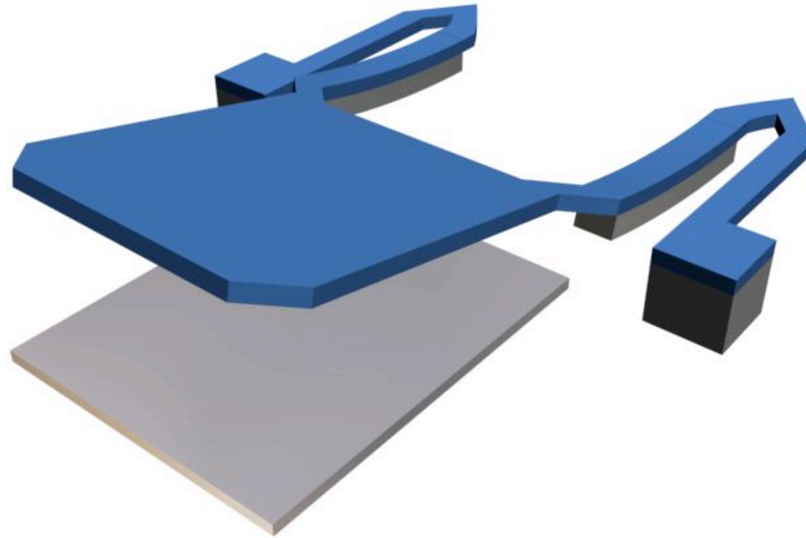

Figure 20 Capacitive detector designed by Multispectral
Bimaterial regions feature aluminum on the backside of the legs. The absorber serves as a moveable plate of a variable capacitor.

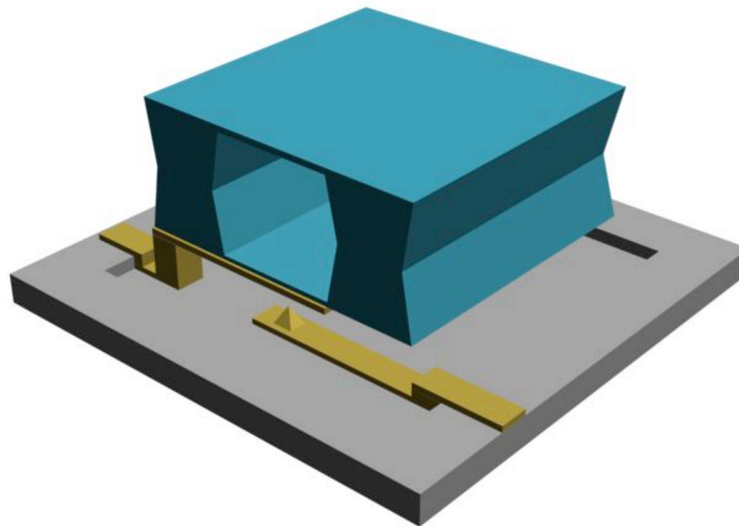

Figure 21 Pneumatic Detector
Incoming infrared radiation is absorbed by a porous membrane inside the gas chamber. The absorbed energy heats the gas and the pressure increases pushing the membranes outward. The membrane deformation is quantified by a tunneling readout. The readout is conceptually similar to the one used in scanning tunneling microscope.

3×10^{-10} W/Hz$^{-1/2}$. Using the Equation 19, where P_0 is assumed to be *NEP*, T_t becomes the calculated *NETD*. *NETD* calculated in such way assuming τ_0 and F to be 1 and 30 Hz bandwidth, is estimated to be 0.868 mK. It should be noted however, as mentioned before, that this detector has a very large area so a low *NETD* value is expected, but to completely characterize the detector, other parameters, such as normalized detectivity, are needed. However, the value is provided for comparison.

The quartz resonator IR detectors have been proposed by Vig et al. [42]. Its operation is based on the property of quartz resonators to change their resonant frequency as their temperature changes. One of the possible designs, where the resonator is connected to the substrate by four micro-bridges, for better thermal isolation, is illustrated in Figure 22. Quartz is, itself, a good absorber in the IR band. Palik [87] has calculated the average absorption of 17% in the 8-14 μm wavelength band. However, for increased absorption, detectors are coated by an IR absorbing material and sometimes even coated on the back-side to create a resonant optical cavity. These detectors are very sensitive, resistant to noise and can operate at temperatures ranging from -55 ˚C to +85 ˚C. However, packaging issues, high power consumption and crosstalk in arrays make it hard for imaging implementations. They can, however, be used in spot detectors [88]. For the 1.8 GHz nominal frequency detector made of 90 μm x 90 μm of 900 nm thick quartz, coated with 17 nm Au thin film and connected to the substrate by 25 mm bridges, predicted τ is 10 ms and total NETD is 8.3 mK.

The design of most of the uncooled micromechanical infrared detectors discussed above (except for quartz detectors and detectors fabricated by Multispectral) is such that the radiation passes through the substrate (usually silicon wafer) in order to reach the detector (Figure 23a).

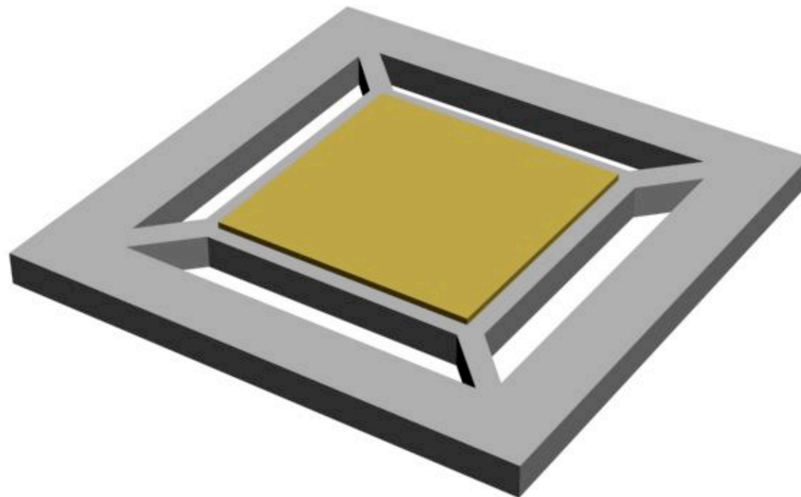

Figure 22 Quartz-resonator IR detectors
These detectors experience frequency shift when their temperature changes.

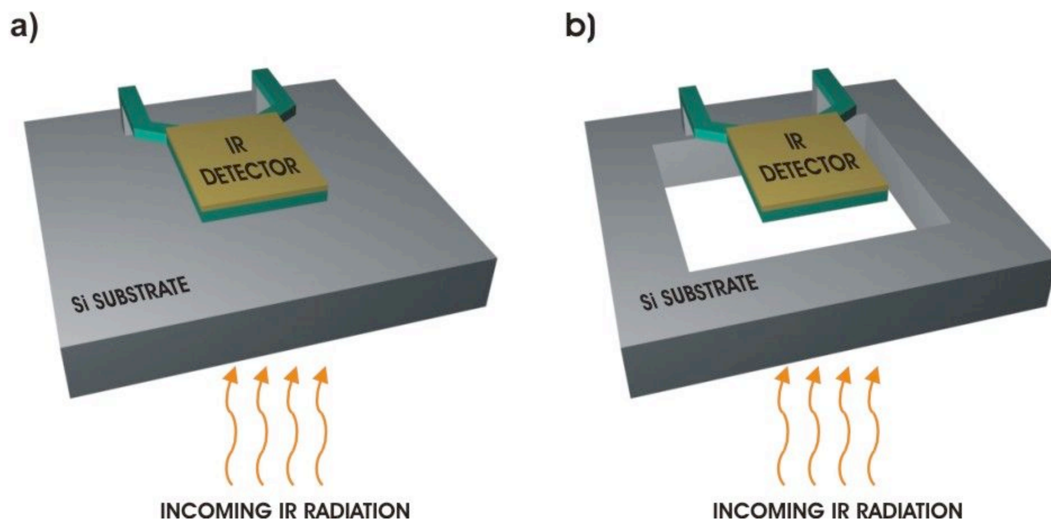

Figure 23 Illustration of regular IR detector vs. substrate-free detector
a) A significant portion of the incoming radiation is reflected and/or absorbed by the substrate in contemporary detectors. b) When the substrate is removed underneath the detector, the unobstructed path is created between the incoming radiation and the detector.

The latest improvement in the design of the uncooled micromechanical IR detectors came from work of groups from University of Science and Technology of China and Institute of Microelectronics at Chineese Academy of Sciences. Their idea is illustrated in Figure 23b. Using a microfabrication process of etching, the substrate underneath of the detector is removed allowing the incoming radiation to reach the detector via an unobstructed path [50, 53, 89]. Such design brought several improvements. It improved the amount of the incoming radiation reaching the detector and therefore made the arrays more sensitive by eliminating the reflection and absorption by the substrate as well as the need for anti-reflective coating. In addition, it removed the shortest pathway for heat loss, which was through convection of the air between the detector and the substrate, significantly improving the thermal isolation of the detector. Dong et al. were able to obtain images of hot objects without placing the detector array in an evacuated package [89]. The arrays reported by Guo et al. were 100 x 100 arrays. The size of each detector was 200 μm x 200 μm and consisted of 2 μm structural SiNx layer with a film of 200 nm of Au in bimaterial sections of the detector. They have fabricated two types of detectors. Ones that maximize the responsivity and others that minimimize the noise using the concept of self-leveling used by Nikon and by Corbeil et al.[30, 67]. The reported sensitivities (in deg/K) were 1.47 x 10^{-3} deg/K and 9.7 x 10^{-4} deg/K respectively. Corresponding reported total *NETD*s were 0.7 K for both types of detectors. An image of a human hand is provided in Figure 24.

The values reported for these detectors are summarized in Table 3.

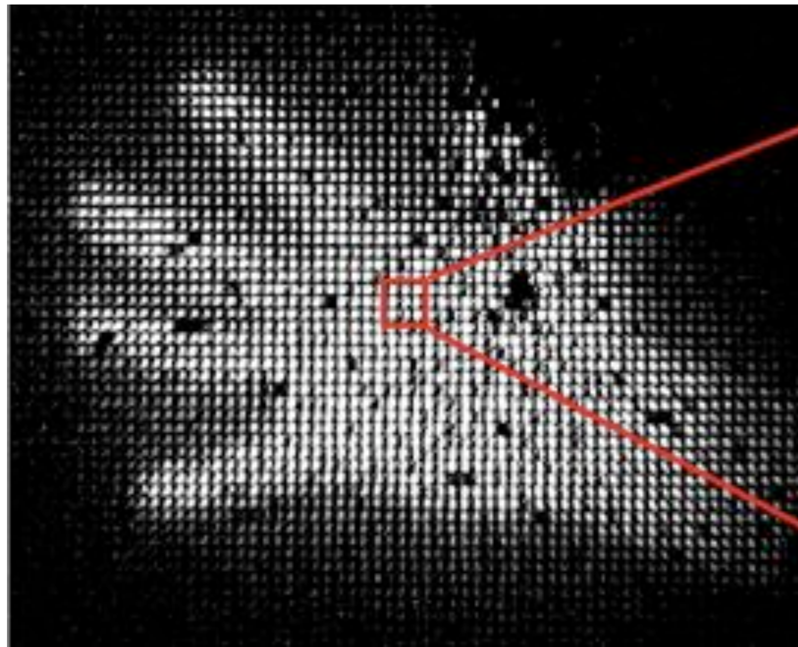

Figure 24 IR image reported by Guo et al. [50]

Table 3 Reported geometries and parameters for some micromechanical IR detectors currently in use

	Size (μm)	Sensitivity	Time constant (ms)	NETD theoretical (mK)	NETD measured (mK)
Nikon	55	0.5 mdeg/K			
Comb	200	110 nm/K	80 ms	2.2	2000-5000
Capacitive	50		9.8 ms	18	
Pneumatic	1700				0.868
Quartz	90		10 ms	8.3	
Substrate-free	200	1.47 mdeg/K			700

It can be seen from both Equation 25 and predicted *NETD* data in the Table 3 that *NETD* is inversely proportional to detector-size. The trend is to decrease the size of the detectors for better image resolution, which means that improvements need to be achieved elsewhere. The improvements could come from improving thermal isolation, improving detector rigidity etc. in order to keep the value of *NETD* acceptably low.

As can be seen from the discussion above and the images obtained, uncooled MEMS IR detectors have developed rapidly in recent years. Their performance is approaching those of bolometers even though there still exists room for improvement in terms of noise reduction. However, their advantages, such as low cost can, can make them a very attractive alternative technology in the future. This dissertation will attempt to combine some of the developments listed above in order to obtain detectors with even better performance.

Chapter 6

Demonstration of Imaging System Using Optically-Probed Micromechanical Infrared Detectors

This chapter is based on the papers titled *Uncooled infrared imaging using uncooled bimaterial microcantilever arrays* article in Applied Physics Letters [15] and a paper titled *Uncooled infrared imaging using bimaterial microcantilever arrays* paper in Proceedings of SPIE [16]

This chapter analyzes an uncooled IR imager based on a micromechanical FPA with optical readout. For this design, the improvements were sought by only modifying the detector geometry while keeping the standard materials such as SiN_x and Au. These materials have been widely used for micromechanical IR detectors and techniques for deposition of thin films of low-stress SiN_x are readily available.

Although many of the available MEMS readout schemes can achieve extremely high sensitivity and acceptably low noise levels, optical probing offers a contactless readout of micromechanical thermal transducers without the need for on-chip electronics and complex wiring architectures. The later factor has largely limited the size of the microbolometer and other electronically probed IR FPAs to or below 640×480 pixels [90]. Furthermore, fabrication of FPAs integrated with the readout interconnects and electronics often involves complex high-cost processes, such as membrane transfer bonding.

The focus was on micromechanical sensing elements with geometry simpler then that of Ishizuya et al. [30], yet smaller then that of Zhao et al. [31] in order to enable arranging (tiling) them into large arrays with a fill factor of 62%. The material of choice was SiN_x as it has shown favorable properties such as possibility of deposition of low stress layers as well as for good absorption in the 8 μm to 14 μm band as demonstrated by Datskos et al.[14] (Figure 9). This band is of interest for infrared imaging of room-temperature objects. The design of individual detector is displayed in Figure 25.

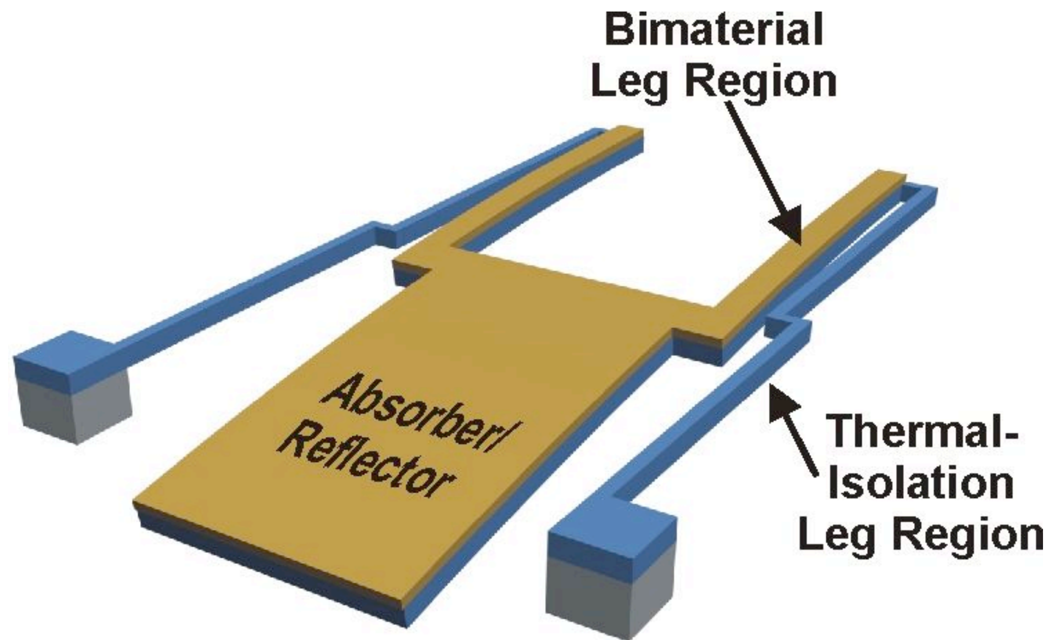

Figure 25 Illustration of SiN_x detector
Legs are folded for increased effective length increasing the thermal isolation. Active region consists of bimaterial region of the legs and the absorber/reflector.

It consists of an absorber and the pair of legs folded around in order to increase the effective length of the thermal isolation region. Absorber, also serving as a reflector, and coated portions of legs comprise the active part of the detector. Each detector is composed of a 600 nm structural SiN_x layer, with a 120 nm Au film in the bimaterial region. The absorber size was ~ 30μm x 60 μm. An 256 x 256 FPA was fabricated where the pitch is 75 μm. Theoretical calculations put the *NETD* limit to about 150 mK and response time of 13 ms. Experimental data indicates *NETD* between 450 mK and 2.5 K and the thermomechanical sensitivity of 50 nm/K

6.1 Fabrication

An array of 256×256 structures was fabricated using low stress SiN_x layers as structural material and Au as a second layer in the bimaterial regions [14]. Figure 26 shows an ion micrograph of a portion of the array with a 75μm × 75 μm pitch. Also shown in the inset is a close-up of an individual microcantilever where the patterning of the deposited metal (Au) layer can be seen. The brighter areas on the detector head and bimaterial regions indicate the presence of metal (Au). The two small rectangular openings in the center of the reflector are etch-holes designed to facilitate removal of the sacrificial oxide layer under the structure during the release step.

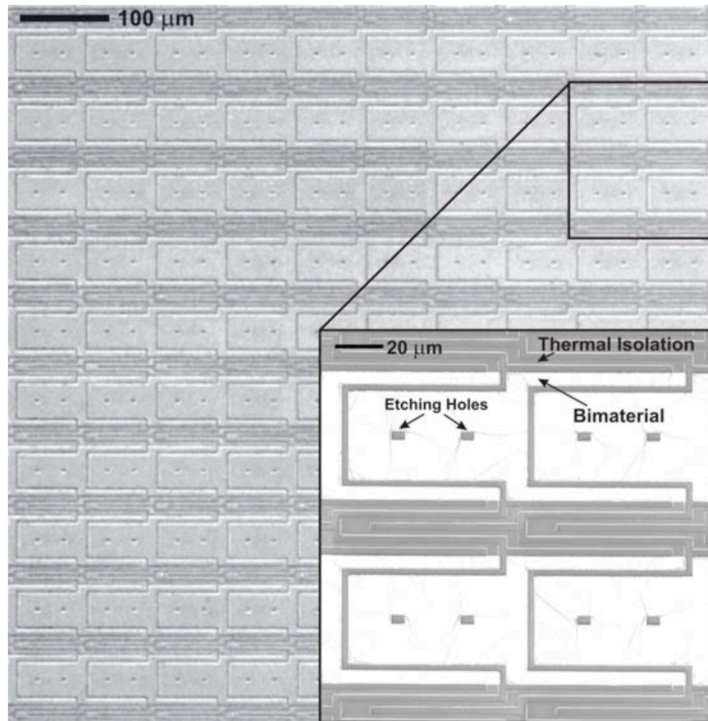

Figure 26 Ion Micrograph of the portion of the fabricated 256×256 MEMS FPA
The inset shows a close-up of detectors where the pattern of the deposited metal (Au) layer can be seen as brighter regions.

The diagram in Figure 27 illustrates the microfabrication process. The process flow involved only three photolithographic steps and, therefore, the overall level of microfabrication complexity was significantly lower compared to the microfabrication of other previously reported uncooled IR FPAs. During the first photolithographic patterning, reactive ion etching was applied to the original double side polished Si wafers through a photoresist mask and resulted in formation of arrays of 5 μm tall posts that provided anchoring for the subsequently formed suspended structures. An ICP SF_6 based etching process was used for Si etching. In the next step a 6.5μm thick silicon oxide sacrificial layer was deposited using plasma enhanced chemical vapor deposition (PECVD) at 250 ^{0}C. The resulting wafers were planarized using chemo-mechanical polishing (CMP) until a 4.5 μm thick oxide layer flush with the Si posts remained. The CMP was followed by deposition of a 600 nm thick structural SiN_x layer on the planarized oxide surface. The second photolithography involved lift-off patterning of a 120 nm Au layer evaporated on SiN_x. E-beam evaporation of the Au metallization was conducted immediately after depositing a 5 nm Cr adhesion layer. The pattern in the lift off photoresist layer corresponded to the superposition of the bimaterial leg sections and reflective regions of the detector heads. This third photolithography was used to define the detector geometry in the SiN_x layer. The final step in the FPA fabrication was using wet etching in the concentrated HF of the sacrificial layer, followed by rinsing and CO_2 critical point drying

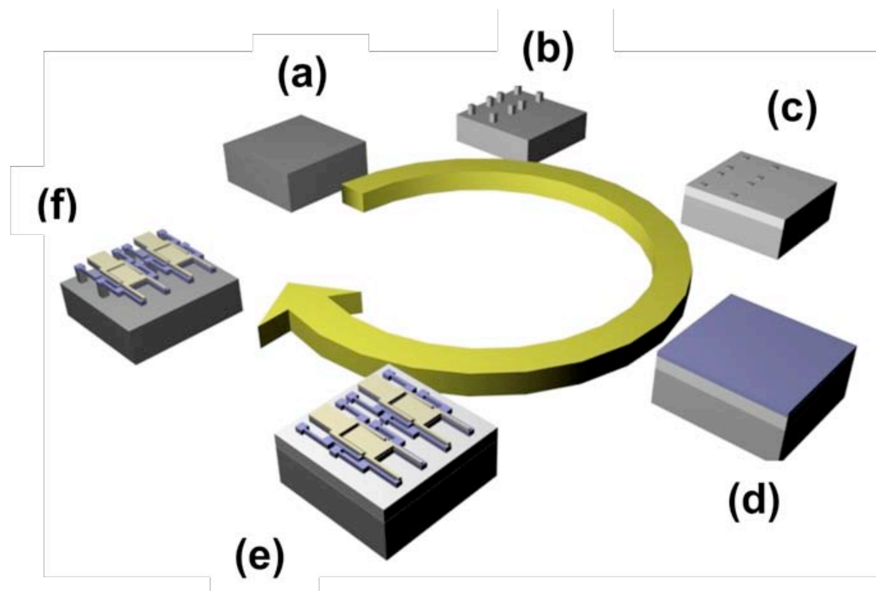

Figure 27 Microfabrication steps
(a) a double-polished Si wafer used as a substrate; (b) fabrication process started with reactive ion etching that created posts on the silicon wafer; (c) SiO_2 sacrificial layer was deposited; (d) chemo-mechanical polishing (CMP) was followed by deposition of a low-stress SiN_x layer; (e) lift-off metallization was followed by patterning of the detector geometry in SiN_x using RIE; and (f) wet etch of the sacrificial SiO_2 layer resulted in a released, suspended structure.

Comparison of the Model and Experimental Results

The finite element analysis predicted that the first two resonant modes of the structures were at 8.6 kHz and 14.5 kHz respectively. The material properties used in these computations are shown in Table 1. The lowest two resonant modes are the fundamental transverse resonance of the head and of the legs, respectively. The computationally predicted resonances were compared to the oscillatory behavior of the structures probed experimentally using the optical lever technique [91]. Typical frequency spectra of the microcantilever structures are shown in Figure 28. These results were obtained either by exciting the structures with a laser modulated in a sweeping mode (curve "A") or by recording the Fourier transform of spontaneous oscillations due to thermal energy as a resonant frequency spectrum (curve "B"). Both spectra show similar resonance features at 7.4 kHz and 12 kHz and are consistent with the finite element analysis.

An important parameter of microcantilever thermal detectors is their thermomechanical sensitivity, $\Delta z/\Delta T$, where Δz is a deflection and ΔT is a temperature change of the detector. Finite element analysis and analytical calculations yielded $\Delta z/\Delta T$ of 76 nm/K and 78 nm/K, respectively. The experimentally obtained value of $\Delta z/\Delta T$ for the fabricated structures was 50 nm/K. The discrepancy in these values can be explained by uncertainties in the Young's moduli and coefficients of thermal expansion of the two layers in the bimaterial structure. Our computations relied on previously reported material properties. Because these parameters depend on the exact deposition method,

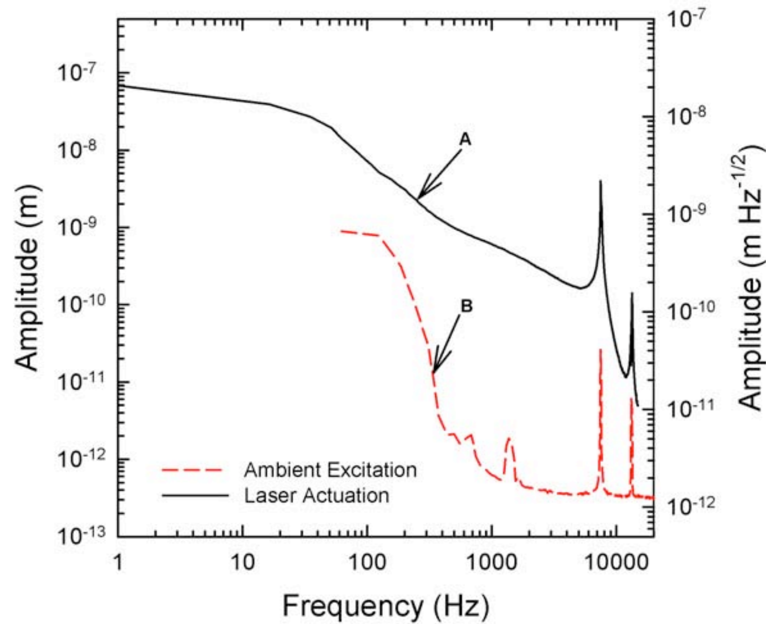

Figure 28 Frequency spectrum of the micromechanical IR detector structures
The two peaks at 7.4 kHz and 12 kHz represent fundamental resonance modes of the absorber and legs, respectively. Solid line represents the detector oscillatory response of the to the actuation by a laser modulated at different frequencies. Dashed line represents the frequency spectrum of spontaneous oscillations due to ambient excitations.

the values used in our calculations may differ from the actual material preoperties of the fabricated structures.

During regular operation of the cantilever thermal detector in the evacuated chamber at a pressure of 10 mTorr, the main heat loss mechanism is the conductance through two beams (“legs”) connecting the suspended bimaterial region of the detector to the substrate. Our measurements have also been conducted at 10 mTorr. Thermal conductance G is calculated using Equation 15 and assuming the thermal conductivity, g of the material (Table 1), and dimensions of the structure. For the current geometry, the finite element model predicted thermal conductance G of 5.06 x 10^{-7} W/K. A response time for these structures calculated using Equation 3, where G is determined by conductance through the legs only, is 7.67 ms. Experimental measurements of the response time were performed using the photothermal excitation with a laser driven by a square wave signal. The laser response to the driving signal as well as the cantilever response are displayed in Figure 29. Frequency of the square signal was 10 Hz and its amplitude was 30 mV. After performing the exponential fit to both rising and decaying segments, the response time of 6 ms was obtained. Using this value of the response time, the thermal conductance G was calculated to be 6.47×10^{-7} W/K. The difference between the values of thermal conductance calculated using experimentally measured response time and materials

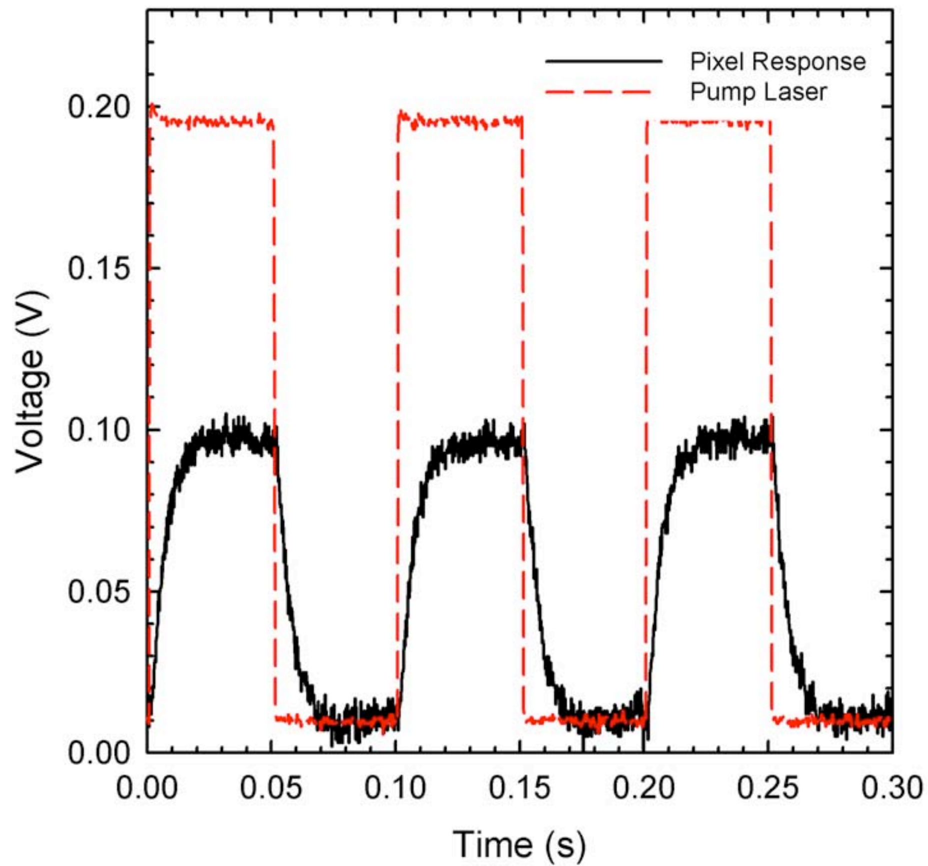

Figure 29 Response of the SiN_x detector to laser excitation
The frequency of the excitation signal was 10 Hz. Fitting the detector response in the form of tip deflection into the exponential saturation curve, yielded the response time of 6 ms

properties is related to the fact that the conduction through the legs is not the only heat dissipation pathway under the actual experimental conditions. In particular, radiative heat exchange may have contributed significantly when the temperature of the detector increased due to absorbed energy from the actuating and readout lasers. Therefore, the radiative heat exchange between the detector and its surroundings may have contributed to the total thermal conductance and, in turn, caused faster thermal response.

In order to gain insight into the fundamental limits of the microcantilever FPAs, as well as to properly compare its performance to that of other conventional IR detectors, it was most suitable to characterize the most commonly used parameter, *NETD*. The *NETD* was calculated using the equations provided in Chapter 4 for *NETD* influenced by the temperature fluctuations, $NETD_{TF}$ (Equation 33), background fluctuations, $NETD_{BF}$ (Equation 37), and thermomechanical fluctuations, $NETD_{TM}$ (Equation 45) along with the material properties given in Table 1. By using an active area of the detector of 3×10^{-9} m^2, along with assuming optics transmissivity of 0.5, 30 Hz bandwidth, background temperature of 307 K, detector absorptivity η of 0.5, and $(\Delta P/\Delta T)_{8-14\mu m}$ = 2.62 Wm^{-2} K, where P is power radiated by a blackbody target within the spectral band from λ_1=8 μm to λ_2=14 μm, k=0.024 N m^{-1} and Q=6000, the calculated $NETD_{BF}$, $NETD_{TF}$ and $NETD_{TM}$ were 2.52 mK, 14.2 mK and 301.4 mK respectively. The total *NETD* was calculated to be 301.7 mK.

6.2 System Integration

Schematic illustration of the implemented prototype of MEMS FPAs corresponds to the concept for simultaneous readout of multiple detectors described in Chapter 2. It is shown in Figure 30 along with the photograph of the actual setup. The IR radiation from the target was focused onto the array using a 50mm F=1 IR lens (TYTO, Janos Technology, Inc). The laser diode operated under a lasing threshold was used as a source of the probing light. The diverging light emitted by this spot source was re-focused by a 100 mm doublet lens (Lens 1 in Figure 30) so that it was converging to a size of the FPA at its plane. The total power of the beam and the power per detector were approximately 1mW and a few nW, respectively. The beam reflected off the FPA reached its minimum cross-section at the front plane of the 30 mm lens mounted on the CCD camera. The required angle-to-intensity conversion was achieved due to a small aperture (1/11) of this lens. Hence, the optical readout converted deflections of individual detectors (caused by different temperatures of the target being imaged) into proportionally varying intensities of the light projected onto a CCD chip. As a result, the object imaged by the MEMS FPA could be readily reconstructed by analyzing the output of a regular 12-bit CCD camera sensitive to visible light. Approximately one-to-one correspondence between the pixels of the CCD and detectors of the MEMS FPA was used in our experiments. Requirements for focal lengths and relative positions of the components had to satisfy the following requirements:

$$\frac{1}{f_1} = \frac{1}{o_1} + \frac{1}{\left(i_{11} + i_{12} + i_{13}\right)} \tag{73}$$

and

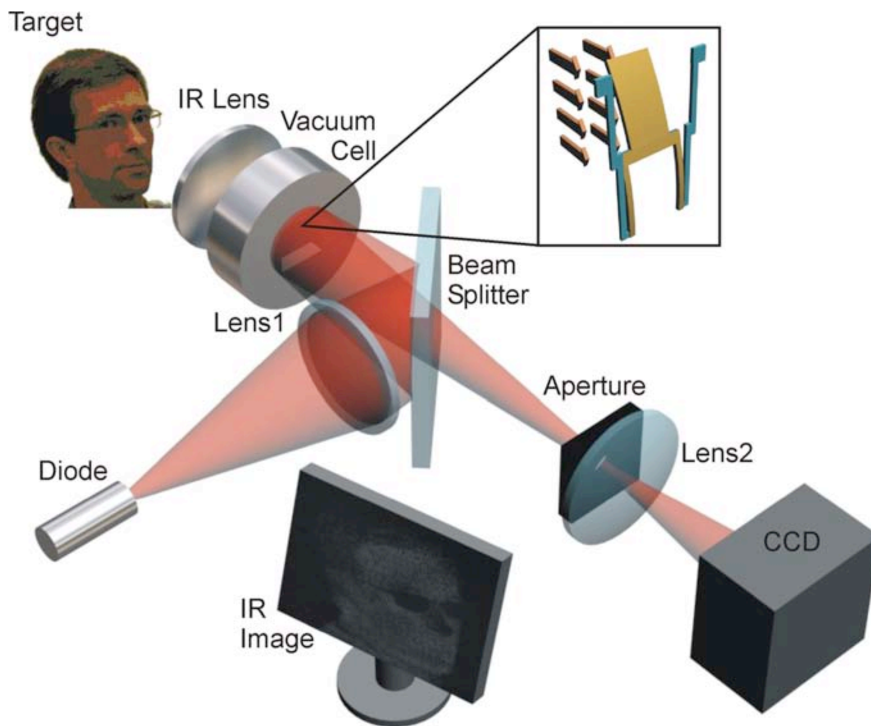

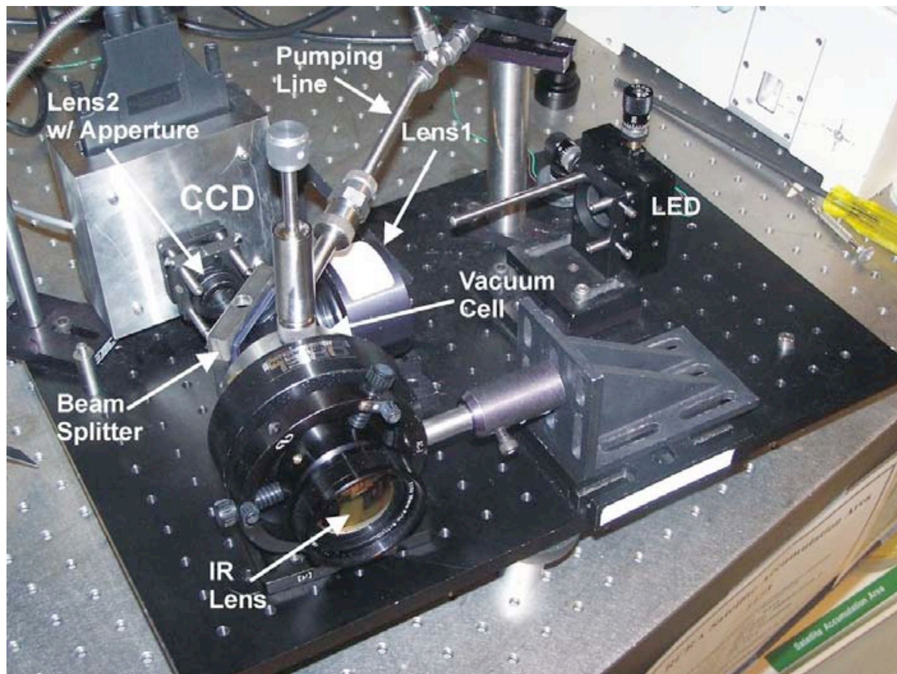

Figure 30 Schematic illustration and photograph of components and arrangement used in the implemented prototype of a MEMS IR imager
Probing visible light is emitted by a diode, re-focused by Lens1 and stirred onto the FPA using a beam splitter. The FPA is monitored by a CCD through Lens2 IR Lens is used to project IR photons from the target onto the FPA.

$$\frac{1}{f_2} = \frac{1}{o_2} + \frac{1}{i_2} \tag{74}$$

The parameters used in this equation are defined in Figure 31.

Using the above described readout, the *NETD* of the fabricated FPA was also measured experimentally using a calibrated blackbody source. For each detector element in the FPA, a value of *NETD* was determined using modified Equation 9:

$$NETD = \frac{C_N}{C_s}\left(T_T - T_B\right), \tag{74}$$

where C_s is the averaged output level of the CCD camera pixel and C_N represents the value for the noise. Here, T_s and T_B are the temperatures of the source (target) and the background, respectively. The histograms for all the pixels displaying the area of the blackbody temperature for temperatures of 0° C and 34° C are displayed in Figure 32. The average *NETD* value was 1.5 K and 1.3 K for target temperatures of 273 K and 307 K, respectively. It is important to emphasize, however, that the values of *NETD* experimentally determined for each microcantilever in the array span from less than 500 mK to approximately 2.5K. Our analysis of the *NETD* histogram indicated that several hundreds of detectors were characterized by *NETD* values of 500 mK or less. This means that only a relatively small portion of the detectors in the array had close to optimal (theoretically predicted) IR absorption and readout efficiency. The microcantilever-to-microcantilever variability in IR absorption and readout efficiency can be attributed largely to slight non-uniformity in the initial microcantilever bending due to the variability of their residual stress. The remaining discrepancy between the experimentally determined *NETD* for best performing microcantilevers (<500mK) and the theoretically predicted *NETD* value (301mK) can be attributed to the readout noise. The following sources of noise in the utilized optical readout were likely to limit the experimentally observed *NETD*: spontaneous intensity fluctuations in the readout light source, CCD camera noise, and disturbances in the refractive index of air within the readout optical path.

In order to determine the IR imaging capability of the system, a uniform background image of the FPA was first recorded (usually with a room-temperature lens cover in front of the IR lens). During the real time image acquisition, the camera assembly was pointed to the object and previously recorded background image was being subtracted from each frame. The result of this subtraction was displayed at a rate of 30 frames per second (fps). When pointed into the target, the IR lens projected the incoming radiation onto the detectors in the array resulting in deformation of detectors, which absorbed the IR photons. The portion of visible light, reflected from deformed detectors, was now stirred off the center of the aperture in front of the Lens 2 and blocked by the aperture. This resulted in change in light intensity detected by the corresponding CCD pixels. Subtracting the background from the newly obtained image revealed areas on the CCD with pixels whose intensity has changed, reconstructed as bright areas of the IR image, while leaving the areas with pixels not exposed to the IR photons with almost unchanged intensity, reconstructed as dark area of the infrared image (Figure 33).

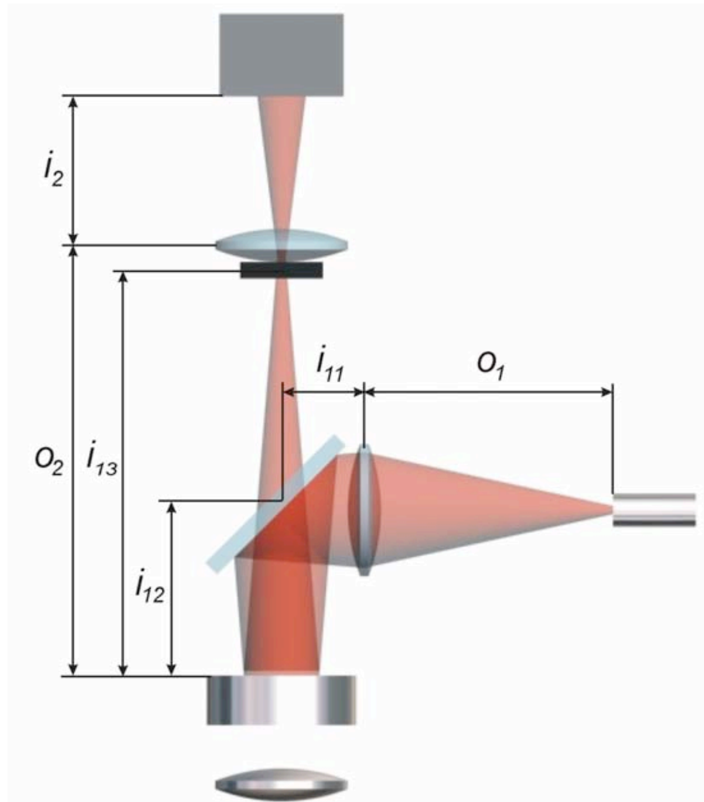

Figure 31 Optical configuration of the integrated system
Examples of IR images obtained with $F = 1$ IR optics are displayed in Figure 33

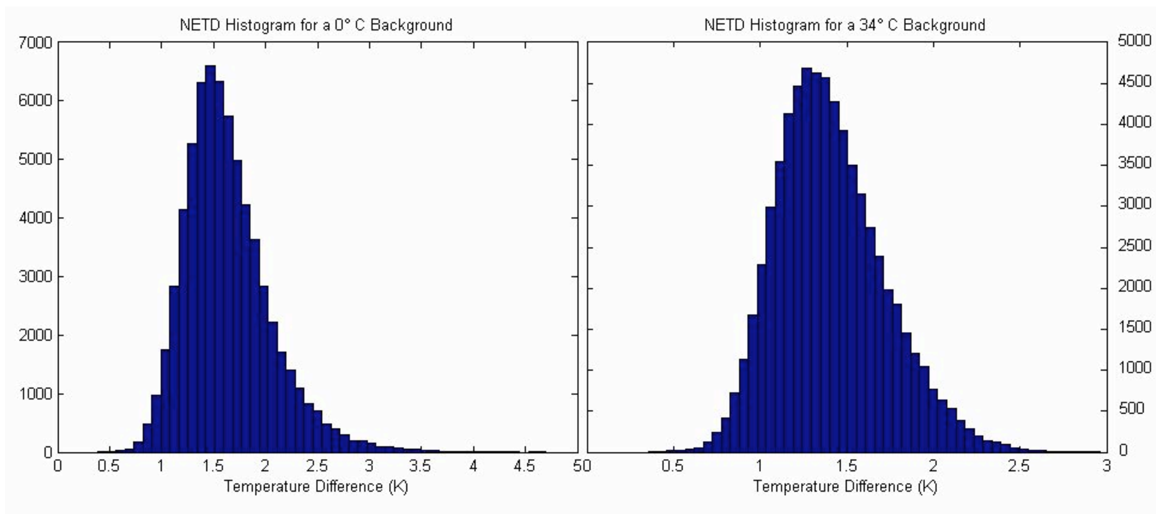

Figure 32 Two histograms of the pixels displaying targets with recorded backgrounds at different temperatures
It can be seen that majority of the pixels exhibit *NETD* of 1.5 K

Figure 33 Infrared images of human faces obtained using SiN_x detectors
The photographs of human faces are displayed along with corresponding infrared images

In summary, an uncooled IR imager based on a FPA array of micromechanical detectors has been demonstrated and it was characterized by an average *NETD* of about 1.5 K with some areas in the FPA having an *NETD* as low as 500 mK. This is an improvement over the detectors reported by Zhao et. al. [31] Our analysis showed that *NETD* of the fabricated FPA would improve if the readout components introducing less noise were used. In addition, application of more advanced image processing would additionally enhance the IR image quality. The measured response time of 6 ms for our fabricated FPA is acceptable for a 30 fps real-time video IR imaging. It is worth noting that the most important practical implication of the present approach is, however, is easy scalability to much larger (>2000×2000) FPAs.

Chapter 7

Design and Characterization of SiO_2 Substrate-Free Detector Arrays for IR and THz Imaging

This chapter is based on the paper titled *Arrays of SiO_2 Substrate-Free Micromechanical Uncooled THz and Infrared Detectors* accepted for publication in Journal of Applied Physics[36]

A number of advantages of optically-probed micromechanical infrared detectors have been discussed in detail in previous chapters. In this chapter, the two concepts discussed above, namely SiO_2-based structures and substrate-free design, are combined into a SiO_2 substrate-free micromechanical detectors for both infrared and THz imaging. Since the ultimate goal is developing affordable IR imaging devices suitable for a wide range of applications, further performance improvements of micromechanical infrared detectors have been investigated, this time by modifying both detector geometry and optimizing the combination of materials. This chapter also discusses modification of detector's immediate environment (substrate) in order to minimize the incoming radiation power loss through the substrate and to minimize the heat loss through convection of the air between the absorber and the substrate immediately beneath each detector.

The operation of the proposed FPA is based on the bimetallic effect and is discussed in detail in previous chapters. The key parts of each newly designed detector element in this FPA are radiation absorber, bimaterial region and thermal isolation region. In order to minimize thermal losses, the effective length of the thermal isolation region has been to maximized without unnecessary increase in detector size. On the other hand, similar increase in effective bimaterial region length has been achieved as well as improvement of the magnitude of deformation per degree of temperature change. Even though the material of choice for suspended micromechanical structures is most often silicon nitride (SiN_x) because of its high uniformity, compatibility with silicon based processing, and controllable stress [31, 52, 53, 89], we tried pursuing presently not very utilized SiO_2. Silicone dioxide has several potential advantages over SiN_x that promised improved performance of our newly designed micromechanical infrared detectors. The most

noteworthy of them include lower thermal conductivity and lower coefficient of thermal expansion (Table 1). Therefore, SiO_2 is preferable over SiN_x as a structural material as it positively impacts both thermal isolation and bimaterial regions.

The most obvious challenge on the way to implementing micromechanical thermal detectors with SiO_2 structural layers is high stress, which is particularly uncertain in thermally grown silicon oxides. As we have mentioned in previous chapter, Hunter et al. has demonstrated the feasibility of fabricating SiO_2-based IR detectors [46]. Their structural layer, however, featured multiple layers needed for purposes of capacitive readout while no group has pursued pure SiO_2 to date. It is important to emphasize that the bimaterial effect increases in the following order: Au-SiNx; Au-SiO_2; Al-SiO_2 (Table 1). The latter pair of materials was chosen for our design as it is capable of yielding the maximum deflection response to temperature changes due to the highest discrepancy in thermal expansion coefficients which, according to Equations 12 and 13, yields the highest deflection-per-degree of temperature change.

In all previous implementations of the micromechanical IR detectors with optical readout, the incident IR radiation was passing through the solid Si substrate. While this imposes several limitations on the detector performance, the most fundamental of them is related to the longest detectable wavelength: transmission through silicon decreases dramatically for photons with wavelengths above 15 μm [92]. In order to surmount this limitation, following the design strategy of Dong et al. [89] is proposed, *i.e.* removing the substrate material underneath the absorbing area of each detector. There are multiple advantages of this approach. In addition to providing an unobstructed optical path for IR and THz photons, this design eliminates the shortest pathway for heat transfer between the absorber and the substrate. Therefore, the thermal isolation of the detector can be improved allowing imaging even while the FPA is at atmospheric pressure [89]. Finally, in this process, the detectors are released by removing the substrate underneath them. Therefore, there is no need for raising the posts and using a sacrificial layer which was required for building almost all micromechanical infrared detectors and also one of the limitations that has prevented use of SiO_2 (i.e. it was hard to find a adequate sacrificial layer for microfabrication of SiO_2 structures). This immediately simplified the microfabrication process as it removed the requirement for etching of the posts, sacrificial layer deposition and chemomechanical polishing (CMP).

This chapter attempts to analyze and demonstrate the viability of fabricating micromechanical detectors suitable for both IR and THz imaging so the dimensions of the design reflect this desire. The analysis consists of a comparison of the finite element model to the experimental characterization of fabricated detectors. The proposed design combines the advantages of microfabricating the SiO_2-based and substrate-free arrays of microcantilever IR/THz detectors. To address the stress issue, two different types of SiO_2: thermal oxide and PECVD oxide have been investigated.

7.1 Model

Our model of an infrared detector consists of responsive bimaterial regions, and thermal isolation regions. Figure 34 illustrates a proposed detector design. Similar structures with SiN_x structural layers have been demonstrated in the previous work of our group [93] and by other groups [50, 53]. In the present design, bimaterial regions are folded in

order to accommodate a greater effective length [50, 53, 93] in a compact area of each element of the FPA. The central rectangular portion of the bimaterial region is designed to provide both absorption of the radiation being detected and reflection of the probing optical beam. As described by Guo et al. [50], this design is referred to as deformation-magnification structure and magnifies the thermal deformation by utilizing the fact that deformation of individual bimaterial regions are additive. Hence, the total angle of deformation is the sum of the angles of deformation of the two bimaterial regions as shown in Figure 35.

The overall size of the detector element was chosen taking into account photon wavelengths of the THz range. The thicknesses of the SiO_2 structural layer and an Al coating are 1000 nm and 200 nm respectively. The key thermal and mechanical parameters of this structure were initially determined by conducting the Finite Element Analysis (FEA). The material properties used in the model are provided in Table 1.

By performing modal analysis, six resonant modes of the structure have been determined. The fundamental (lowest) and second resonant frequencies were found to be 4.31 kHz and 4.37 kHz, respectively. Both of these modes are longitudinal, causing the reflector to oscillate out of the plane of the array. The modes are illustrated in Figure 36 and tabulated in Table 4. The third and fourth modes are antisymmetric, causing the torsional oscillations of the absorber. The fifth and sixth modes are mainly oscillations of the legs and do not cause significant motion of the absorber.

In addition to FEA, a simplified analytical model was evaluated that relied on the effective spring constant k determined from the FEA model by applying the force of 1 nN on the tip of the absorber and recording the resulting displacement. The force of 1 nN resulted in the displacement of 89.8 nm. Hence, the effective spring constant was 0.011 N/m. By applying the formula $\omega = \sqrt{k/m}$ to the lowest resonance mode $\omega = 27.1 \times 10^3$ rad/s, the effective suspended mass of the structure of has been obtained 2.32×10^{-11} kg.

Thermal analysis of the FEA model provided the values of thermal conductance between the central bimaterial region (absorber) and the substrate. The thermal conductance was obtained by applying a heat flux of 1 μW evenly distributed over the area of the absorber. The resulting temperature distribution in the whole structure relative to the heat sink is shown in Figure 37a. As can be seen in Figure 37a, 1 μW of power induces the temperature difference of 18.78 K between the absorber and the substrate (heat sink). It can also be seen from Figure 37a that, due to the high thermal conductance of the metal film, all bimaterial regions (including the absorber) are isothermal. This results in the whole temperature gradient being distributed over the thermal isolation regions. Since the isolation legs 2 and 4 are of the same dimensions, their temperature gradients need to be identical making the temperature of the bimaterial leg 1 twice the temperature of bimaterial leg 2. This can be verified by checking the temperatures corresponding to the colors of the bimaterial legs in Figure 37a.

Table 4 Modeled resonant modes of the deformation-magnification structure

Mode	1	2	3	4	5	6
Frequency (kHz)	4.31	4.37	11.61	16.93	17.6	18.1

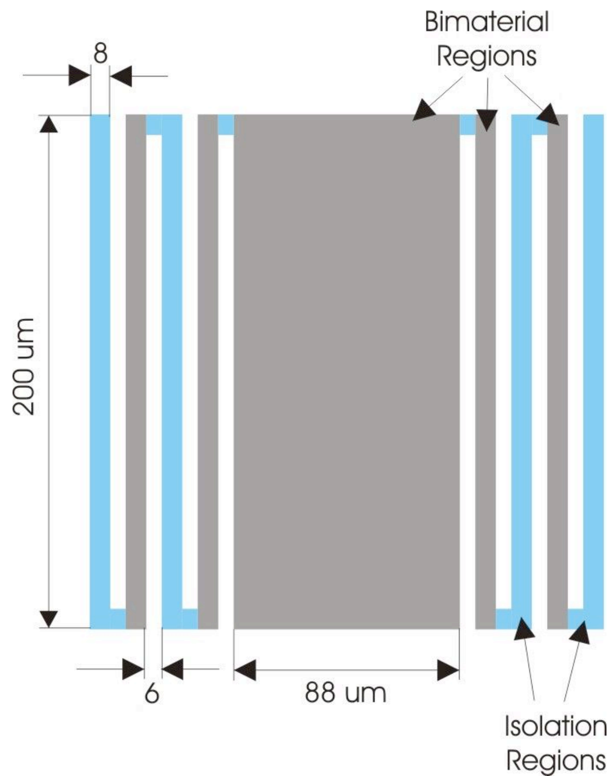

Figure 34 Illustration of the geometry of the substrate-free detector design
Dark areas represent bimaterial regions and bright areas represent the thermal isolation regions. This design is shown to maximize the detector sensitivity

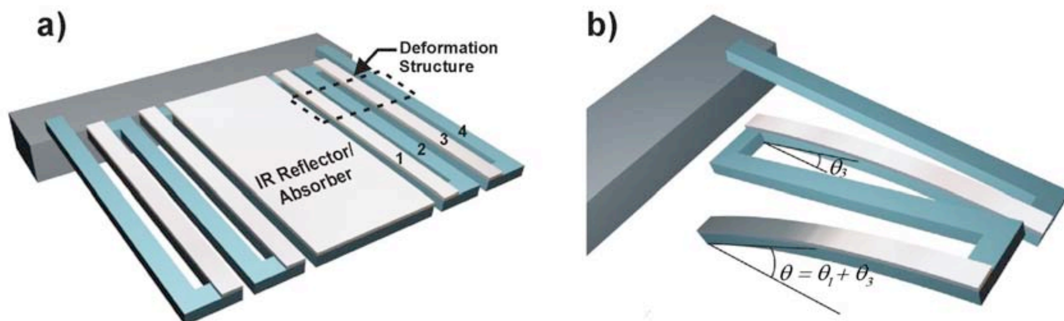

Figure 35 Illustration of addition of individual bimaterial region's deformation angles for deformation-magnification structure
Individual angles of deformation of bimaterial legs 1 and 3 are additively combined into the total angle of deformation of the reflector/absorber

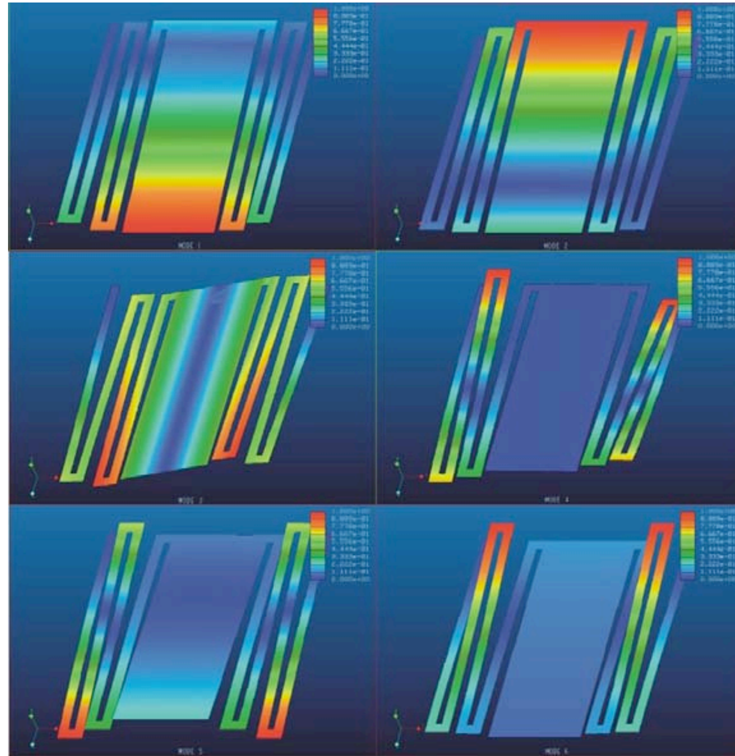

Figure 36 Illustration of the deformations of the structure in each of the first 6 modes of oscillation

The displacements are scaled such that the largest displacement in each mode has a magnitude of 1.

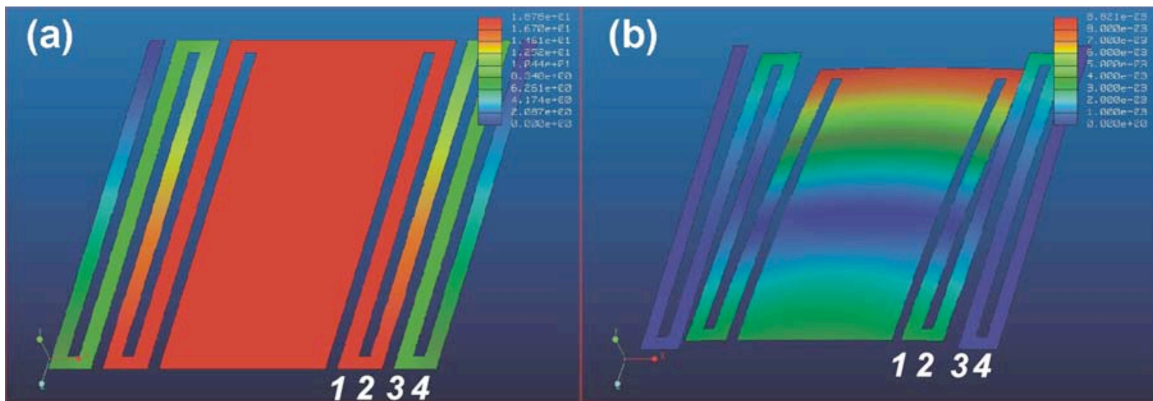

Figure 37 Thermal analysis of substrate-free detectors

(a) Temperature distribution caused by the 1 μW heat flux over the area of the absorber. (b) Thermal deflection (in mm) caused by the temperature distribution shown in figure A.

The total temperature difference between the absorber and heat sink yields thermal conductance of 5.32 x 10^{-8} W/K between the absorber and the substrate. The model only considered thermal conductance through the supporting structure and did not include heat loss through convection and radiation. Notably, this value is about an order of magnitude lower than that for the micromechanical thermal detectors with SiN_x structural layers [15, 50].

The parameters obtained as described above were then used in the dynamic (deflection) analysis (Figure 37b). As can be seen in Figure 37(b), the largest deflection is experienced by the absorber. The tip of the structure deflects out of plane by 8.8 μm at ΔT of 18.78 K. This corresponds to thermo-mechanical sensitivity of 468 nm/K. It can be seen that the back end of the absorber rises above the plane of the detector, while the tip falls below the plane. The approximate deflection angle was calculated by obtaining the absolute distance between the two ends of the absorber, in a direction perpendicular to the plane of the detector, and dividing it by the absorber length. In the case of ΔT of 18.78 K, the deflection angle was found to be 6.4 x 10^{-2} radians. Dividing the deflection angle by the temperature increase on the absorber, the sensitivity of 3.41 x 10^{-3} rad/K was obtained. This is a 70% improvement compared to the theoretical predictions for a similarly sized and shaped SiN_x structure reported previously [53].

The tip deflection and deformation angle per unit temperature can also be obtained by using Equations 12b and 13 along with material properties from Table 1 and detector geometry. For the simplification of deformation angle calculation, the absorber is assumed to remain flat even though its deformation will follow the deformation of bimaterial regions. The tip deflection is calculated using the formula, obtained taking into account the geometric arrangement of bimaterial regions (detailed derivation provided in Appendix.

$$\Delta z = \frac{3}{2}\Delta z_1 \tag{75}$$

where Δz_1 is the tip deflection from its equilibrium plane of the bimaterial region closer to the absorber. Similar expression is valid for the angle of deformation, θ, at the tip of the detector. The factor of ½ comes from the outer bimaterial region having the temperature increase half that of the inner one and the tip-displacement and angle of deformation being linear with temperature increase.

$$\Delta \theta = \frac{3}{2}\Delta \theta_1 \tag{76}$$

The calculated values for tip displacement per unit temperature and angle of deformation per unit temperature were 522 nm/K and 5.22 × 10-3 rad/K respectively. The vertical tip displacement estimate is slightly higher then the one obtained using the finite element model since Equation 75 is a slight overestimate due to the complex geometry (see Appendix). Estimating the deformation angle at the tip is simpler, and if the flat absorber is assumed, the deflection of the whole absorber will be equal to the deflection at the tip of the bimaterial leg 1. This value calculated by Equation 76 is larger then the estimate obtained by dividing the vertical distance of the absorber divided by its length, which is how the deflection angle was estimated using finite element analysis. This value was smaller due to deformation of the absorber, as can be seen in Figure 37b.

Finally, the thermal time constant of the detector was obtained by using Equation 3. A heat capacity C of 3.58 x 10^{-8} J/K for the absorber was obtained by using the dimensions provided in Figure 34 and material properties from Table 1. Equation 3 then provides the predicted thermal time constant of 672 ms based on the thermal conductance through the legs only. Equation 3 shows that there is a tradeoff between the thermal isolation (which, in turn, determines the sensitivity) and the response time. In other words, better thermal isolation improves the detector sensitivity at a cost of a longer response time.

In order to compare this design with other similar uncooled detectors, its fundamentally limited performance expressed was estimated in terms of noise equivalent power (*NEP*), normalized detectivity (D^*) and noise equivalent temperature difference (*NETD*). To calculate *NEP*, we used Equations 31, 35 and 43. For estimating the NEP_{TM}, the Equation 43 needed to be modified by the factor of 2 since the expression is derived from the expression for noise for a single bimaterial region (Equation 40) and this design features two of such regions on each side and their displacements are additive (see Appendix). The expression used is given below.

$$NEP_{TM} = \frac{2}{R(\omega)}\sqrt{\frac{4k_B TB}{Qk\omega_0}}, \tag{77}$$

Using the modeled values specified above and the detector geometry, the optics parameters such as transmission $\tau_0 = 0.5$ and $F = 1$, the detector geometry and absorption coefficient $\eta = 0.5$ and assuming a quality factor $Q = 100$, the following values were obtained: $NEP_{TF} = 5.77 \times 10^{-12}$ W, $NEP_{BF} = 8.49 \times 10^{-12}$ W and $NEP_{TM} = 1.88 \times 10^{-12}$ W. The combined *NEP* of the detector due to temperature fluctuations, background fluctuations and thermomechanical oscillations was obtained as:

$$NEP = \sqrt{NEP_{TF}^2 + NEP_{BF}^2 + NEP_{TM}^2} \tag{78}$$

The total *NEP* predicted by the model was 1.04 x 10^{-11} W.

To calculate D^*, we used Equations 32, 36 and 44. For estimating the D^*_{TM}, the Equation 44 needed to be modified by factoring out 2 since D^* is inversely proportional to rms noise amplitude which has been multiplied by the factor of two above. The expression used is given below.

$$D^*_{TM} = \frac{R(\omega)}{2}\sqrt{\frac{Qk\omega_0 A_d}{4k_B T}}, \tag{79}$$

Using the modeled values specified above and detector geometry, the following values were obtained: $D^*_{TF} = 1.26 \times 10^{10}$ Jones (cm $\mathrm{Hz}^{1/2}$ W^{-1}), $D^*_{BF} = 8.56 \times 10^9$ Jones and $D^*_{TM} = 3.86 \times 10^{10}$ Jones. The combined D^* of the detector due to temperature fluctuations, background fluctuations and thermomechanical oscillations was obtained using Equation 7, and is predicted to be 6.96×10^9 Jones.

To calculate the *NETD*, the Equations 33, 37 and 45 were used. For estimating the $NETD_{TM}$, the Equation 45 also needed to be multiplied by a factor of 2 for the reasons discussed above.

$$NETD_{TM} = \frac{8F^2}{\tau_0 A_d R(\omega)\left(\frac{dP}{dT}\right)_{\lambda_1-\lambda_2}}\sqrt{\frac{4k_B TB}{Qk\omega_0}}. \tag{80}$$

Using the modeled values specified above the following values are obtained: $NETD_{TF}$ = 1.00 mK, $NETD_{BF}$ = 1.47 mK and $NETD_{TM}$ = 0.33 mK. The combined $NETD$ of the detector due to these three sources is obtained as[14]:

$$NETD = \sqrt{NETD_{TF}^2 + NETD_{BF}^2 + NETD_{TM}^2} \tag{81}$$

Total $NETD$ predicted by the model is 1.81 mK.

7.2 Implementation

Once the dimensions yielding the optimal parameters have been obtained, the test arrays were fabricated. The layout of FPA was chosen to cover the largest technologically possible area of a 4" wafer. This showed that implemented approaches are suitable for large FPA while the structural integrity of the FPA remained uncompromised. The implemented FPAs contained 63,200 detector elements (pixels) in a format similar to 240 × 160 pixels.

Fabrication of the implemented FPAs involved three photolithographic processes. It is important to note that chemo-mechanical polishing and wet etching were avoided completely, which removed the need for sacrificial layer. The process flow is shown in Figure 38. The geometry used in the process-flow illustration has been slightly simplified for clarity. Initially, 1 μm of SiO_2 was deposited on the front side of a batch of 300-μm-thick double-side-polished (DSP) Si wafers and 2 μm was grown on the backside (Figure 38a). Two alternative processes, (1) the thermal oxidation of SiO_2 at 1100 ^oC and (2) plasma enhanced chemical vapor deposition (PECVD) of SiO_2 at 320 ^oC, were used for this purpose. This allowed us to investigate films with different intrinsic stresses. In addition, 2 μm of SiO_2 was deposited on the backside to serve as a mask for later substrate removal with deep reactive ion etching. The first photolithography was used to pattern a mask in the back-side layer of SiO_2 (Figure 38b). Figure 38c shows the patterned SiO_2 mask after reactive ion etching and photoresist removal. This patterned SiO_2 served as a mask for deep reactive ion etching (DRIE) of holes through the Si wafer underneath each detector. The second lithography (Figure 38d) was used for liftoff metallization of bimaterial regions (Figure 38e). Finally, the third photolithography (Figure 38f) was used to pattern the detector elements into the structural SiO_2 layer by reactive ion CHF_3/O_2 etch (Figure 38g). The front side of the wafer was then coated with a 7 μm film of SPR-220 photoresist and hard-baked for 4 hours at 90 deg C. This step provided protection and structural integrity of the front side during the subsequent deep reactive ion etch (Bosch process). The deep reactive ion etching (DRIE) was subsequently performed to remove the Si substrate underneath each detector. After the DRIE etch, the result was an array of densely packed 220 μm × 220 μm holes through the wafer. The boundaries of each hole matched the boundaries of a detector element on the front side of the wafer (Figure 38h).

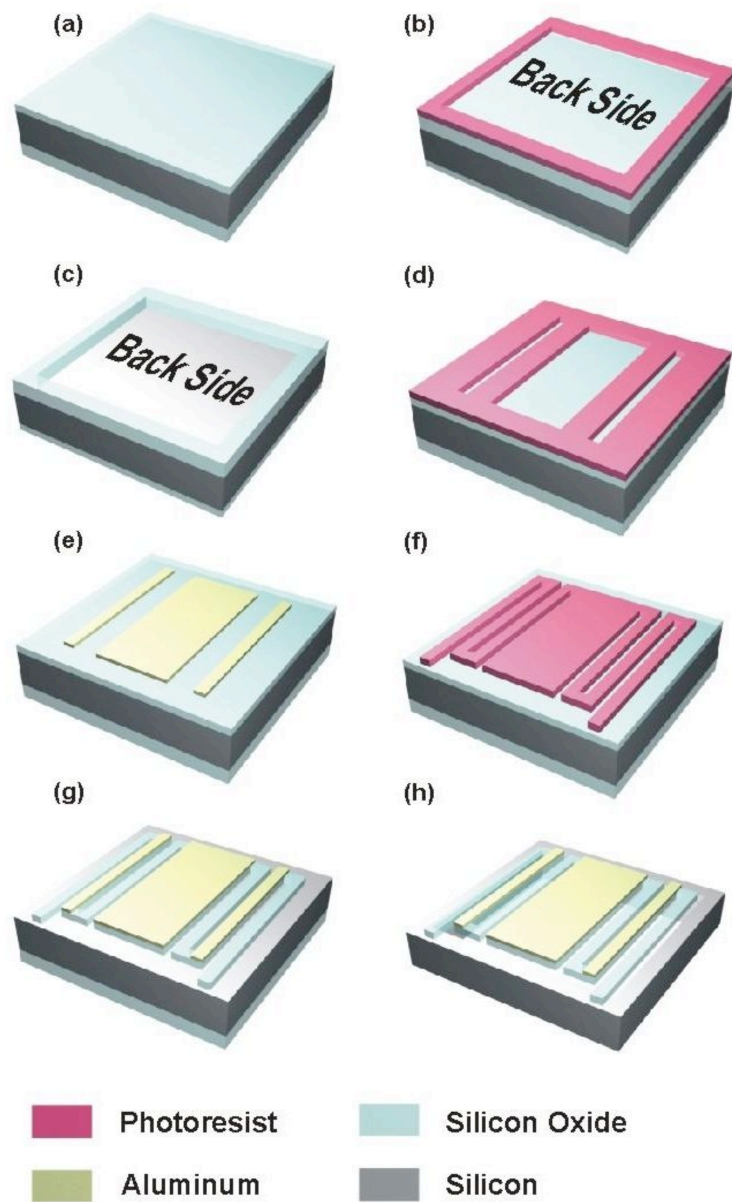

Figure 38 Process flow for the completely dry microfabrication of substrate-free detector arrays

a) Start by coating double-side-polished (DSP) Si wafer by a structural SiO_2 layer on the front side and mask SiO_2 layer on the backside; b) first photolithography used to pattern a mask into SiO_2; c) window mask to be used for deep reactive ion etching later in the process d) second photolithography used for liftoff metallization of bimaterial regions e) metallized regions after resist removal; f) third photolithography to be used to create detector geometry; g) detector geometry prior to removal of Si underneath it and h) released detector after DRIE from the backside using the back-side SiO_2 as a mask.

Figure 39 shows actual microscope photographs obtained after some of the fabrication steps outlined in Figure 38. Figures 39a through 39d correspond to Figures 38d through 38g. Figures 39e and 39f represent the same detector photographed using front side and back-side illumination respectively and they correspond to Figure 38h.

The final fabrication step was the release of structures by etching the protective photoresist layer in oxygen plasma. Figures 39e and 39f indicate that there is some intrinsic stress present after the release as front and backsides are not both in focus. Bringing both of them in focus and recording the height of the microscope lens can be used to determine the initial angle of stress deformation. Despite the fact that majority of the Si bulk was removed during the FPA fabrication, the structure remained robust enough to allow the handling (Figure 40). Note that the highly transparent mesh-like substrate permits enough visible light to clearly see the light source placed behind the wafer.

Described process made the microfabrication of SiO_2 structures simpler and more feasible as it did not involve CMP or use of the sacrificial layer.

Microscope photographs as well as ion micrographs are shown in Figure 41. Figures 41(c) and 41(d) show the magnified individual pixels made out of thermal SiO_2 and PECVD SiO_2, respectively.

7.3 Experiment and Results

Individual detectors from both arrays have been characterized. To quantify the initial stress as well as thermal sensitivity, the optical microscope and a test structure mounted on a heated sample holder were used. The absolute height difference between the two ends of the absorber was determined by focusing the microscope on the two ends. After dividing this displacement by the absorber length, its angular deflection was obtained. The average angle of the room-temperature deflections were 14^0 and 7.5^0 for the structures with thermal and PECVD SiO_2, respectively. In addition, as seen in Figure 41, the thermal-oxide structures were curled up, while PECVD-oxide structures were curled down. Very little initial deformation in thermal isolation regions of the structures with thermal oxide indicates insignificant stress gradient in the thermal SiO_2. However, bimaterial regions are deformed due to differential stress in the evaporated Al relative to the thermal SiO_2. The thermal isolation regions in the structures with PECVD SiO_2 were deformed, indicating an appreciable stress gradient in this layer. The deformation in the bimaterial regions, however, appeared to be lower. This can be explained by the fact that both the PECVD SiO_2 and the evaporated Al layer tend to have tensile stress. A complete balance of stresses in this bimaterial structure may be possible. In particular, the deposition temperature and the thickness of each layer can be varied in order to balance the stress.

The average thermal sensitivities of the implemented structures were 5.18×10^{-3} rad/K and 2.88×10^{-3} rad/K in the case of thermal and PECVD SiO_2, respectively. This correlates well with our FEA predictions, and is an order-of-magnitude improvement with respect to the measured values reported by Shi et al. [53]

Resonant frequencies and thermal response times were obtained using a combination of the conventional optical lever readout described elsewhere [94] and a photothermal excitation [95].

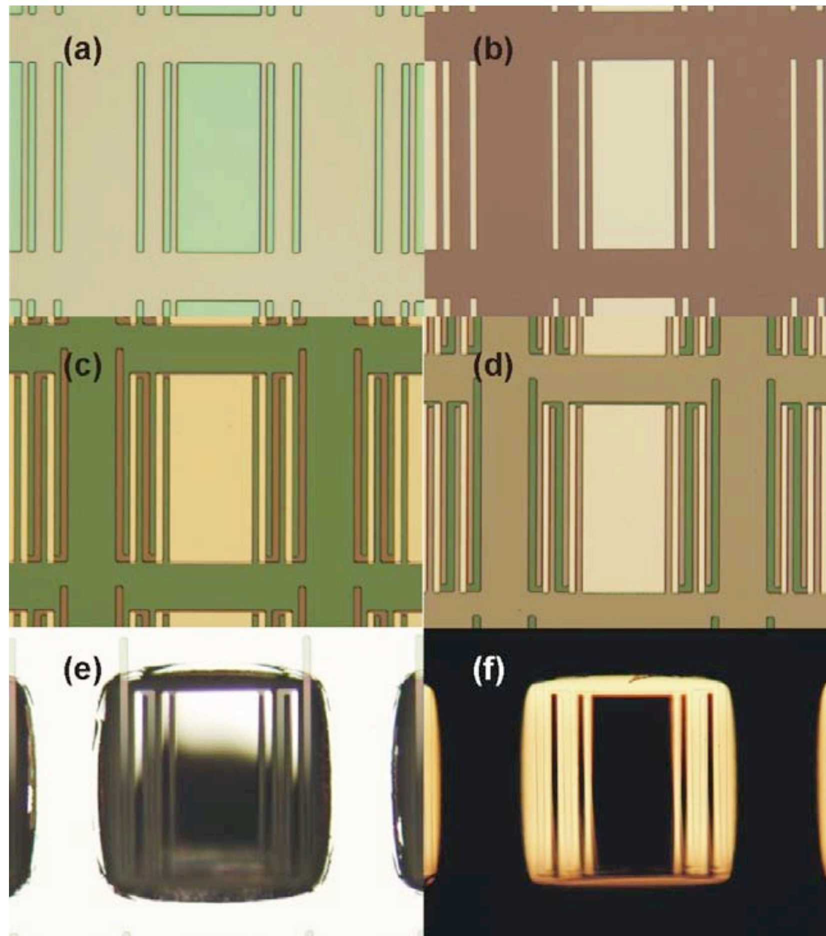

Figure 39 Microscope photographs taken after microfabrication steps
It shows a) photoresist mask for liftoff metallization; b) metalized areas; c) mask for patterning the detector geometry; d) detector geometry after etching; e) released structure photographed using front-side illumination and f) released structure photographed using back-side illumination

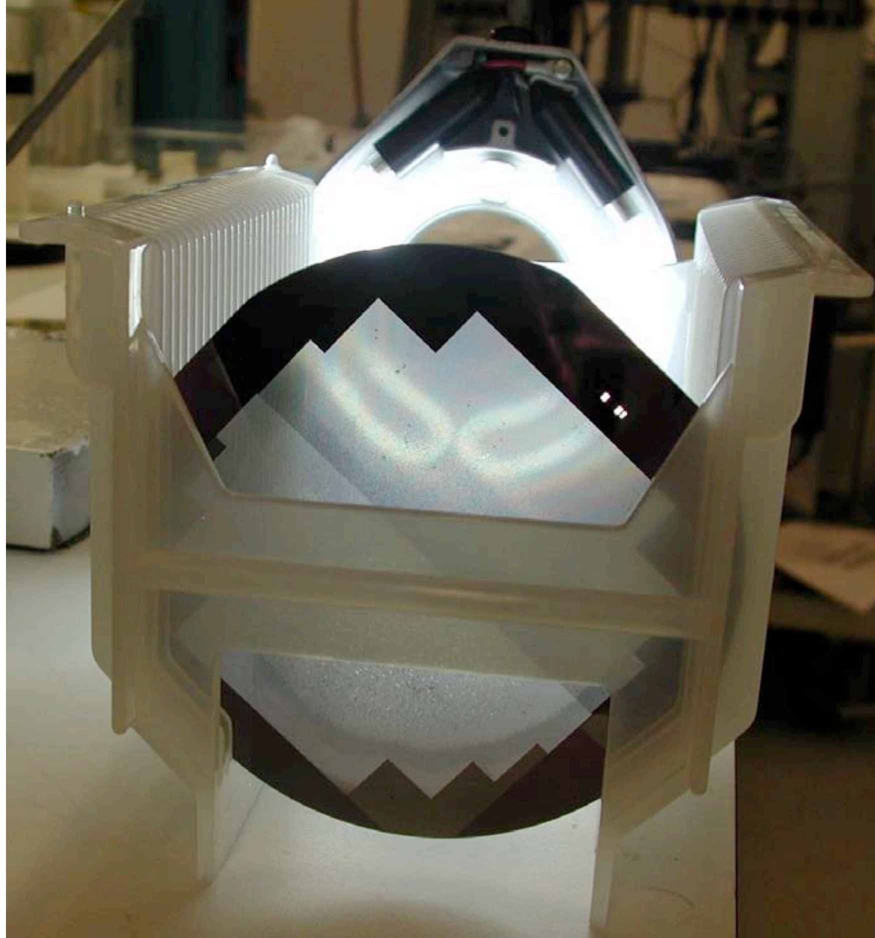

Figure 40 Photograph of a completed wafer of substrate-free detector arrays The processed wafer has a high degree of transparency for visible light. A dense array of through-holes has been formed in the central part of the Si wafer. The wafer remains mechanically robust making it possible to create wafer-sized focal plane arrays.

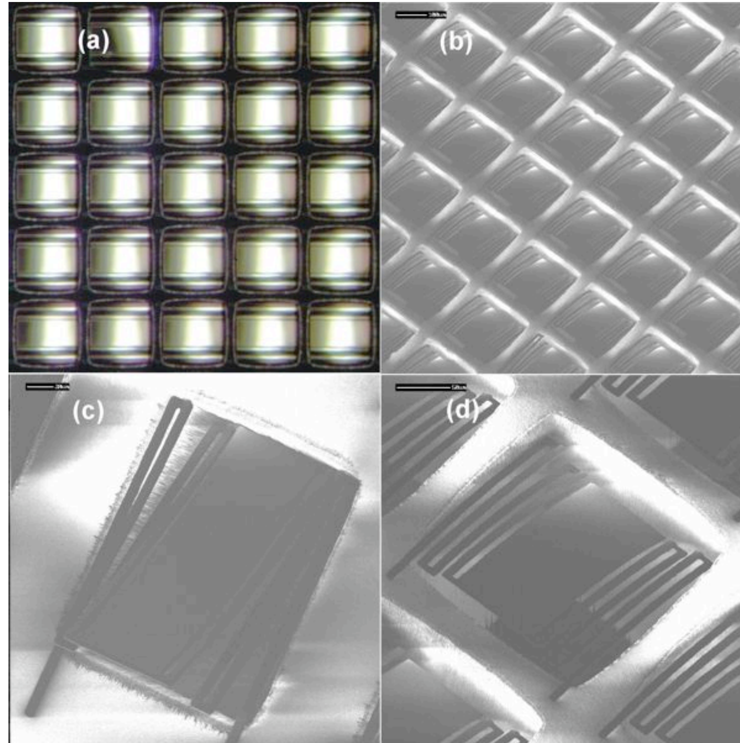

Figure 41 Microscope photograph and ion micrographs of completed SiO_2 substrate-free detector arrays
a) microscope photograph of a fabricated array b) ion micrographs of fabricated array and c) close-up of a thermal SiO_2 detector and d) close-up of a PECVD SiO_2 detector

This optical arrangement is illustrated in Figure 42. The readout diode laser is focused on the tip of a cantilever and reflected into the quad-cell position sensitive detector (PSD). The horizontal and vertical channels of the PSD correspond to the longitudinal and torsional modes, respectively. In order to measure the thermal response time, another modulated diode laser was focused on the detector and provided its photothermal excitation [95]. The square wave signal was used to modulate the laser intensity from zero to its maximum. This resulted in heating-cooling cycling of the detector. The readout laser was then used to quantify the deflection due to these temperature changes, and the resulting waveform was used to calculate the thermal response time. During these experiments, the detector array was inside the evacuated cell at 25 mTorr.

Figure 43 shows resonance spectra obtained as a Fourier transform of spontaneous oscillatory (thermo-mechanical) motion due to ambient excitations. It can be seen that the experimentally measured fundamental mode of the structures with thermal oxide deviates slightly from the FEA simulation. The average value was about 5 kHz with frequencies ranging from 4.4 kHz to 5.5 kHz measured for detectors in different regions of the array. The experimental average value of the lowest resonance frequency, 4 kHz, for the structures with PECVD oxide is more consistent with the FEA prediction. Frequencies ranging from 3.4 kHz to 4.1 kHz were measured. These frequency spreads can be attributed to non-uniformity of the structural oxide layers. The reason average

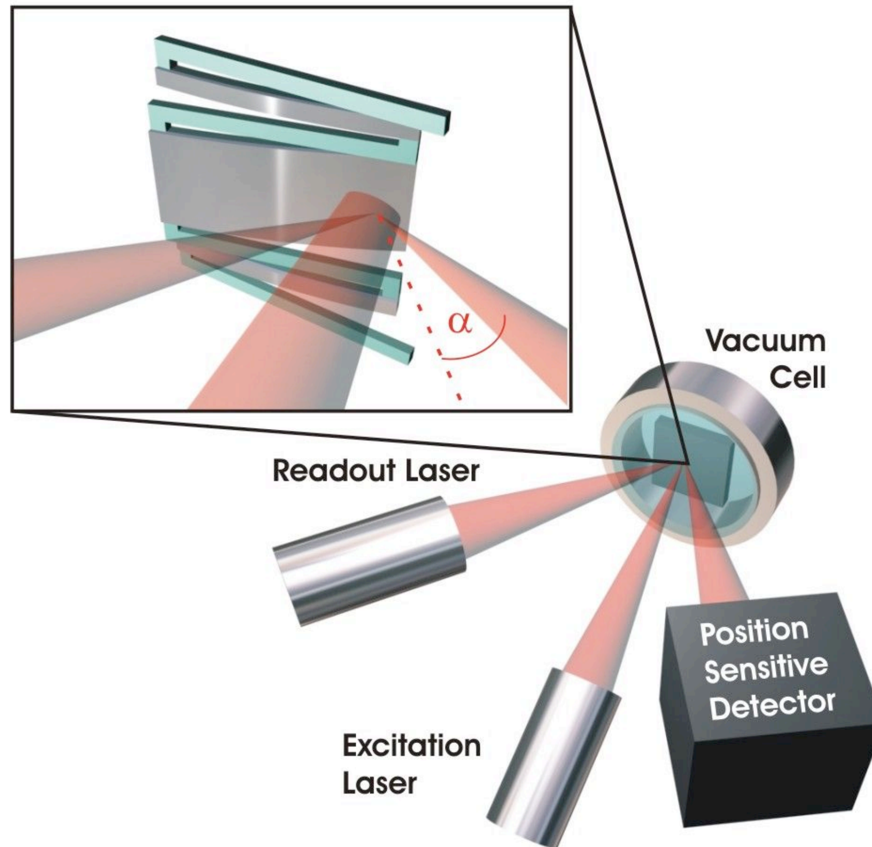

Figure 42 Schematic representation of the characterization system configuration
The FPA is placed in the vacuum cell. A readout laser with a position sensitive detector is used to quantify the deflections of the detectors. A photothermal actuation laser is pulsed in order to induce temperature increase on the detector causing it to deflect. A CCD camera with a microscope lens (not shown) is used for laser alignment

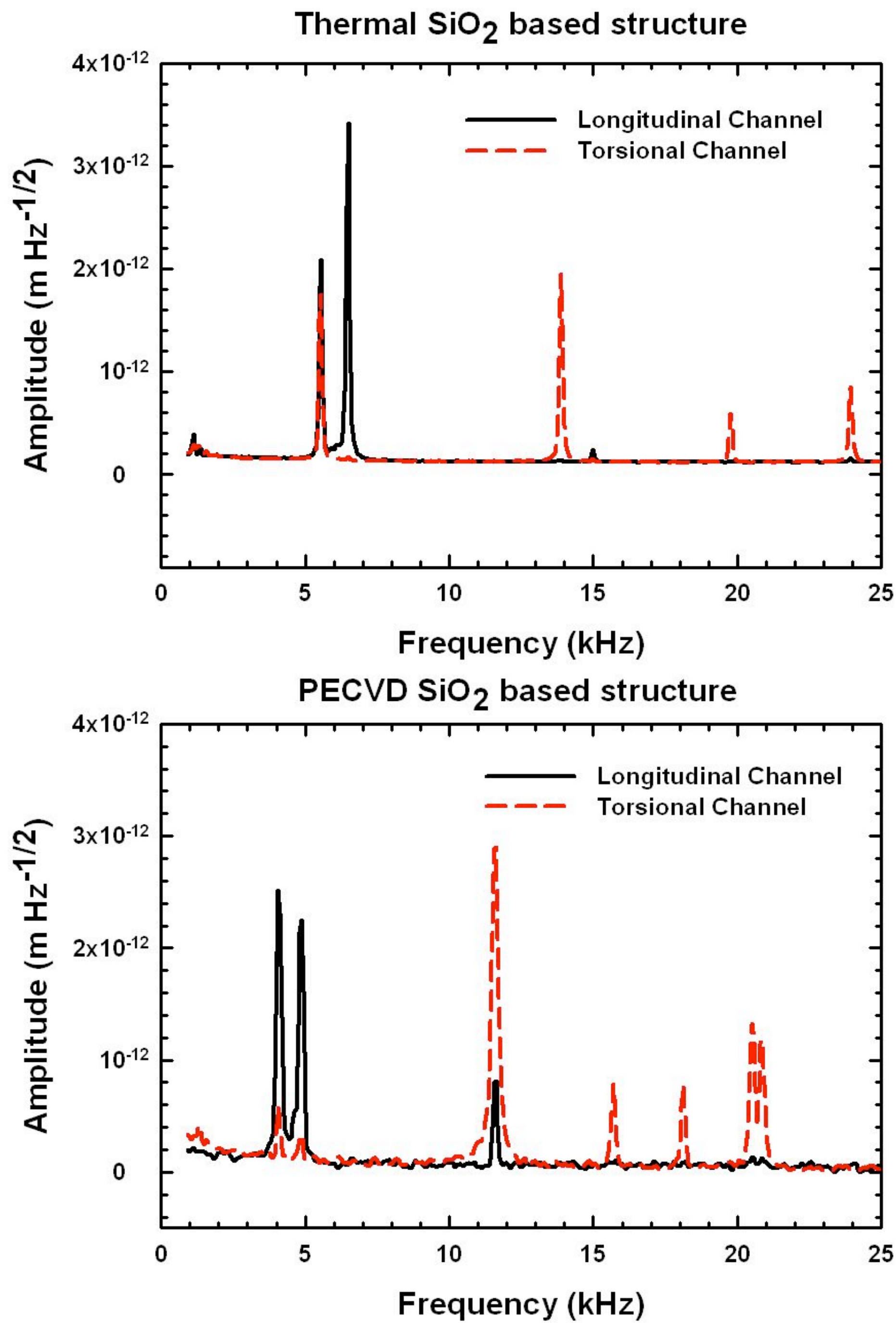

Figure 43 Frequency spectra of substrate-free detectors

Frequency spectrum of thermal oxide structures (upper graph) shows that the fundamental resonant frequency of these detectors was about 5 kHz while frequency spectrum of PECVD structures (lower graph) shows that the fundamental resonant frequency of these detectors was about 4 kHz.

resonant frequency for the PECVD structures is lower is the fact that thermal oxide has a higher Young's modulus than PECVD oxide [96]. Agreement between the experiment and simulation was also found for higher (torsional) modes. Using the experimentally measured fundamental frequencies of the fundamental mode and the effective mass, we find the spring constant $k = \omega^2 m$ to be 0.017 N/m and 0.0097 N/m for the structures with thermal oxide and PECVD oxide, respectively.

The response kinetics measured in photothermal excitation experiments is shown in Figure 44. By fitting the experimental curves to the first order exponential kinetic function, the thermal time constants of 62.5 ms and 53.5 ms were obtained for thermal SiO_2 and PECVD SiO_2 structures respectively. The relatively long response times are consistent with the high thermal isolation of the implemented detectors. Increasing the operating pressure of the detectors could be used to adjust their response times to less than 30 ms, which is normally required for 30 frames per second video imaging. As discussed in our previous work [15], this method of measurement could be introducing an increase in the radiative thermal conductance due to the temperature increase on the detector. This could cause the measured time constant to be shorter than the predicted one. Another reason for the discrepancy between these values might lie in the complexity of the structure, which has 5 separate bimaterial regions.

In order to verify the values obtained for thermal response times, the Bode plot method has been used [97]. This method relies on the thermal response being proportional to $1/\sqrt{1+\omega^2\tau^2}$. The thermal response times estimated using the Bode plots method measured at atmospheric pressure and 25 mT are, respectively, 9.8 ms and 58 ms. The latter value agrees well with the response time of 53.5 ms obtained using the deflection *vs*. time plot. The data taken at atmospheric pressure for the PECVD oxide structures are shown in Figure 45. The experimentally obtained response times were also used to verify our estimates of the thermal conductances for two types of structures. These calculations resulted in 5.73×10^{-7} W/K and 6.7×10^{-7} W/K for the thermal conductance of the structures with thermal and PECVD oxide, respectively.

In order to explore dependence of the thermal conductance on pressure, the detector time constants were measured at different pressures. The plot of measured time constant *vs*. pressure is shown in Figure 46. When compared to the values predicted using the analysis described by[66, 98], we see fair agreement but with a slight offset. This discrepancy is probably due to an increased rate of the radiation heat exchange as the temperature difference increases.

The frequency response graph (inset in Figure 45) was also used in order to estimate the quality factor Q. The obtained value of 50 was fairly low, which is consistent with strong damping by the atmospheric environment. The average Q-factor was measured to be about 400 at 25 mTorr, ranging from 290 to 530 on different detectors. Finally, the obtained values of thermal conductance G, spring constant k and resonant frequency f, have been used to re-iterate our estimates for the fundamentally limited *NEP*s, D^*s and *NETD*s. By using these values in Equations 31 through 37 and Equations 77 through 81, we obtained the following results. *NEP*s for thermal and PECVD oxide structures to be 2.91×10^{-11} W and 3.97×10^{-11} W respectively. D^*s for thermal and PECVD oxide structures to be 2.50×10^{9} Jones and 1.83×10^{9} Jones respectively. *NETD*s for thermal and PECVD oxide structures to be 5.04 mK and 6.82 mK respectively.

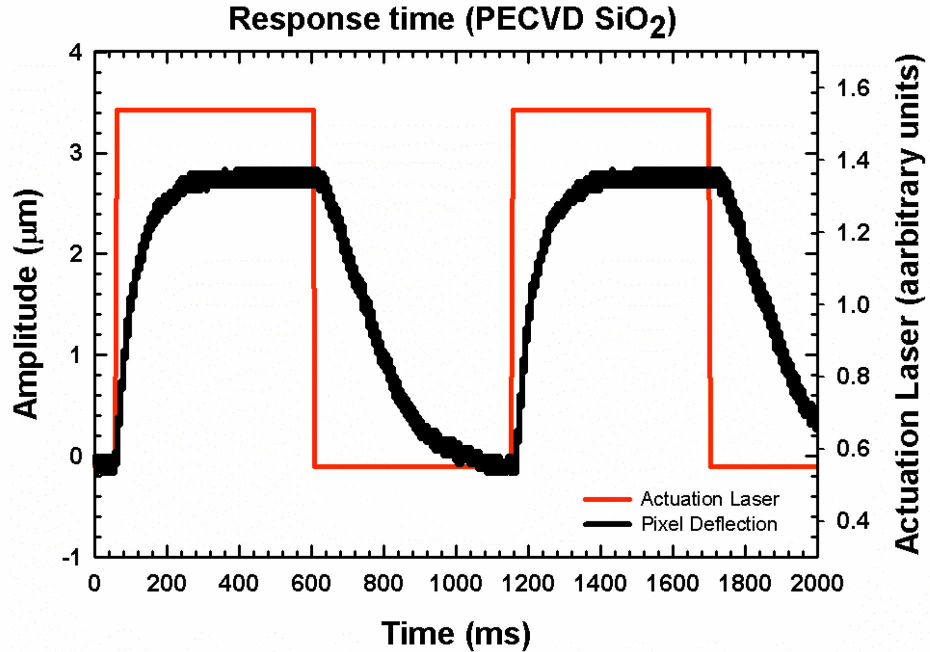

Figure 44 Thermal response times for substrate-free detectors
Displacement of the tip of the detector as a function time during photothermal excitation by a modulated diode laser. These data were subsequently analyzed to obtain the thermal response times. The values were 62.5 ms and 53.5 ms for thermal SiO_2 and PECVD SiO_2 respectively

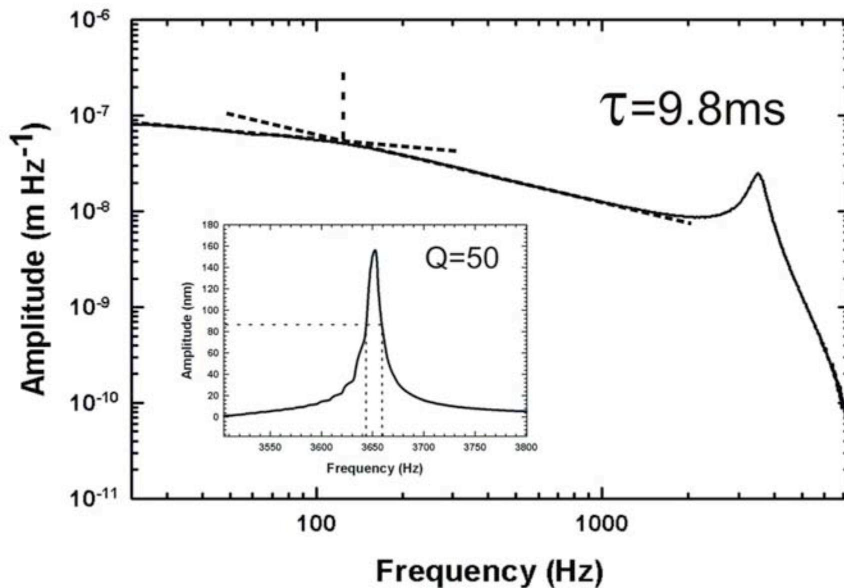

Figure 45 Detector response to laser actuation with detector at atmospheric pressure
The double log plot was used along with Bode method to obtain the response time for detectors at atmospheric pressure. Insert: an estimate for the Q factor of the detector was obtained graphically.

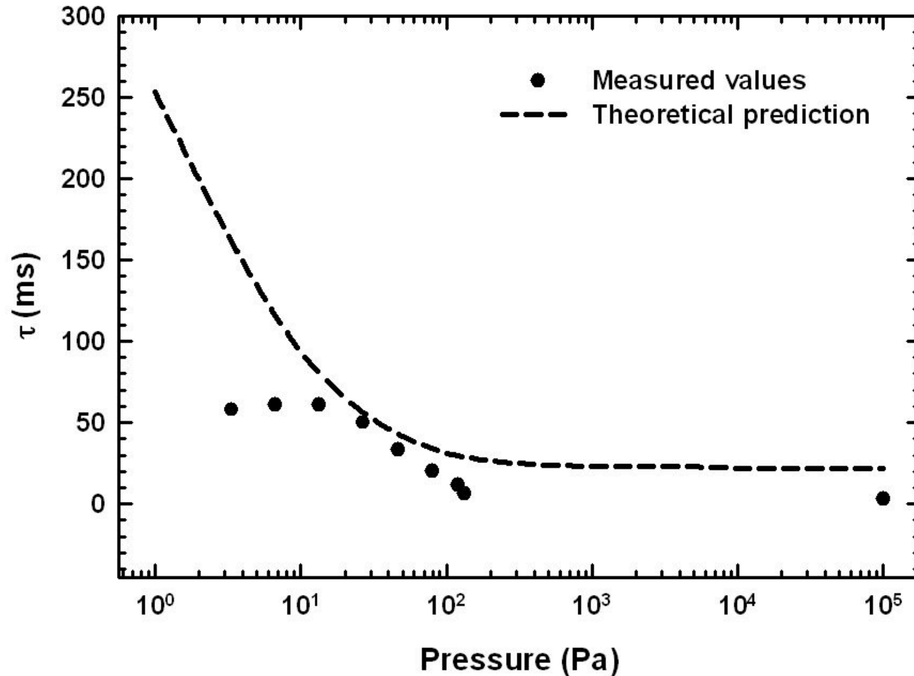

Figure 46 Thermal response times vs. pressure
Measured thermal response times and values predicted theoretically for a particular detector.

7.4 Summary

Results from the previous analysis are summarized in Table 5. Note that the modeled $\Delta\theta/\Delta T$ correspond to the absorber temperature increase, while measured $\Delta\theta/\Delta T$ correspond to the ambient temperature increase. The results of FEA modeling and experimental characterization of substrate-free micromechanical uncooled detectors with SiO_2 structural layers showed promising characteristics with very good mutual agreement. The results obtained with two alternative types of SiO_2 indicate a viable pathway to address the ubiquitous issue of high stress in common silicon oxides. Stress-matching in a (PECVD SiO_2 –Al) bi-layer system may be possible, for instance, by decreasing the SiO_2 thickness while increasing the thickness of the Al coating. Similar bi-layer structures with thermal SiO_2 are more stressed, which makes them less usable in the explored application.

The obtained high thermal sensitivities indicate that the implemented detectors can lead to an IR imaging system with improved performance. The calculated fundamentally limited figures of merit (*NETD* values) also indicate their potential, however, this analysis is limited to noise sources intrinsic to the detector and does not include the readout noise. Analysis of the complete imaging system including obtaining the total *NETD* is discussed in detail in Chapter 9.

Table 5 Summary and comparison of finite element model and experimental results for substrate-free deformation-magnification structure

SiO_2 DMS	Resonant frequency (kHz)	Q factor	Thermal conductance (W/K)	Response time (ms)	$\Delta z/\Delta T$ (nm/K)	$\Delta\theta/\Delta T$ (mrad/K)	NEP (pW)	D* (Jones)	NETD (mK)
SiO_{2model}	4.31	-	5.3×10^{-8}	672	468	3.41	10.4	6.96×10^{9}	1.81
$TSiO_{2actual}$	5.5	50	5.7×10^{-7}	62.5	-	5.18	29.1	2.50×10^{9}	5.04
$PSiO_{2actual}$	4.1	50	6.7×10^{-7}	53.5	-	2.88	39.7	1.83×10^{9}	6.82

Chapter 8

Implementation of SiO_2Substrate-Free Detector Arrays Featuring Built-In Optical Cavity for Enhanced Absorption of IR and THz Radiation

After successfully showing the potential for building the detectors out of SiO_2, further improvements were investigated. This chapter explores an opportunity for enhancing IR or THz absorption by the detector when an appropriate resonance cavity is embedded into the absorber. SiO_2 has favorable thermal expansion and thermal isolation properties but not very high absorbance of incoming IR radiation in the band of interest. To overcome that, the deformation-magnification structure, described in the previous chapter, has been modified by incorporating a layer of amorphous Si into the absorber, with thickness optimized for maximized absorption in the 8-14 μm wavelength range. This range is dominant in IR spectra emitted by room-temperature objects. This design would compensate for the lack of an optical cavity between the detector and the substrate, present in many previously implemented micromechanical IR detectors. Compared to the design described in Chapter 6, the optical cavity is removed by removing the substrate underneath the detectors

In addition to this design, the performance of a version of the design with built-in self-leveling arrangement has also been investigated. This is the concept already employed in designs described in previous chapters by Ishizuya et al., Corbiel et al. and Guo et al. [30, 50, 67], which is such that it minimizes the noise due to fluctuations in ambient temperature.

8.1 Model

8.1.1 Deformation-Magnification Detector

The model of an infrared detector, without self-leveling, with a built-in optical cavity is essentially identical to the deformation-magnification detector of the previous chapter

except it features a layer of amorphous Si between the SiN_x layer and the Al film. Figure 47 illustrates the design of the proposed detector. The central rectangular portion of the bimaterial region is designed to provide an enhanced absorption of the radiation to be detected and reflection of the probing optical beam. The extra layer will make the central absorber more rigid and less prone to thermal deformations. This is actually desirable as it decreases the lensing effect and preferable for optical probing. The overall size of the detector element was kept the same as for the detectors described in previous chapter in order for them to be sensitive to photon wavelengths of the THz range. The thicknesses of the SiO_2 structural layer and an Al coating are 900 nm and 170 nm respectively. The structure thickness was slightly reduced over the previous set of detectors in order to decrease the degree of initial stress. The key thermal and mechanical parameters of this structure were initially determined by conducting the Finite Element Analysis (FEA). The material properties used in the model are provided in Table 1.

The thickness of the amorphous Si layer was optimized using Generalized Rouard method [99]. According to this method, the reflectance of the multi-layer system is given by:

$$R = \left| r_{0,m}{}^{2} \right| \tag{82}$$

where $r_{0,m}$ is the coefficient of reflection between the medium and the last (m^{th}) layer of the system. At the 0° angle of incidence, it is given by a recursive formula:

$$r_{j,m} = \frac{r_{j,j+1} + r_{j+1,m} e^{i\frac{4\pi}{\lambda}\bar{n}_{j+1} d_{j+1}}}{1 + r_{j,j+1} r_{j+1,m} e^{i\frac{4\pi}{\lambda}\bar{n}_{j+1} d_{j+1}}} \tag{83}$$

where $r_{j,n}$ are Fresnel coefficients of reflection between j^{th} layer and last, m^{th}, layer and $\bar{n}_j$ and d_j are the complex index of refraction and thickness of jth layer respectively. Exponential part of the equations is there to account for the phase change in each layer. The reflectance at j^{th} interface, $r_{j,j+1}$, is given by

$$r_{j,j+1} = \frac{\bar{n}_j - \bar{n}_{j+1}}{\bar{n}_j + \bar{n}_{j+1}} \tag{84}$$

where complex index of refraction is defined as $n_j + ik_j$ where n_j and k_j are the index of refraction and index of extinction respectively.

Since the last layer in our case, Al, is completely reflective to IR wavelengths of interest, it was safe to regard the radiation that was not reflected as being absorbed. The optimal amorphous Si layer thickness was the one that yielded the maximum absorption of radiation with wavelengths between 8 μm and 14 μm.

The optimal cavity layer thickness is calculated to be ~700nm. However, the experimental PECVD deposition resulted in a measured 1100 nm thick amorphous Si layer. The reflectance curves calculated for both thicknesses, obtained using Equations 82 through 84, are displayed in Figure 48. It can be seen from Figure 48 that the actual fabricated cavity does not provide as much absorbance as the optimal one, but it should still improve the performance over the detectors without the cavity. For purposes of better accuracy of the model, the thickness used in the model discussed further in this chapter has been adjusted to 1100 nm.

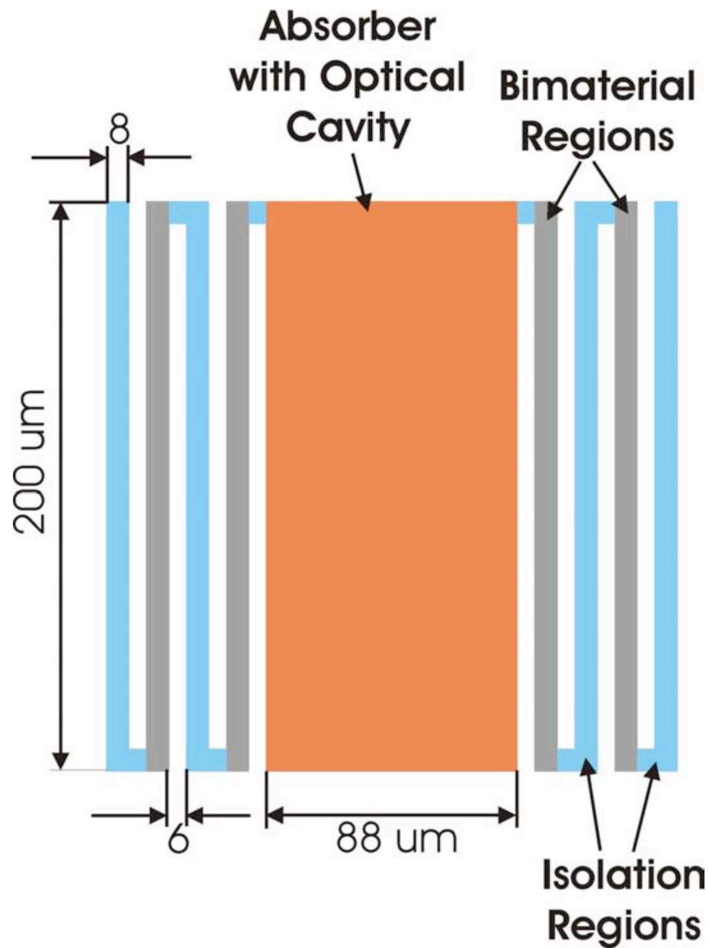

Figure 47 Illustration of geometry of the deformation magnification, substrate-free design with built-in optical cavity

Dark areas represent bimaterial regions and bright areas represent the thermal isolation regions. This design maximizes the absorption of IR radiation by incorporating additional layer of amorphous Si into the absorber, between the structural layer of SiO_2 and Al thin film. This configuration also maximizes the total deformation angle of the reflector, which is the sum of deformation angles of individual bimaterial regions. Resonant cavity layer together with deformation-magnification effect significantly improve the overall detector sensitivity to IR radiation.

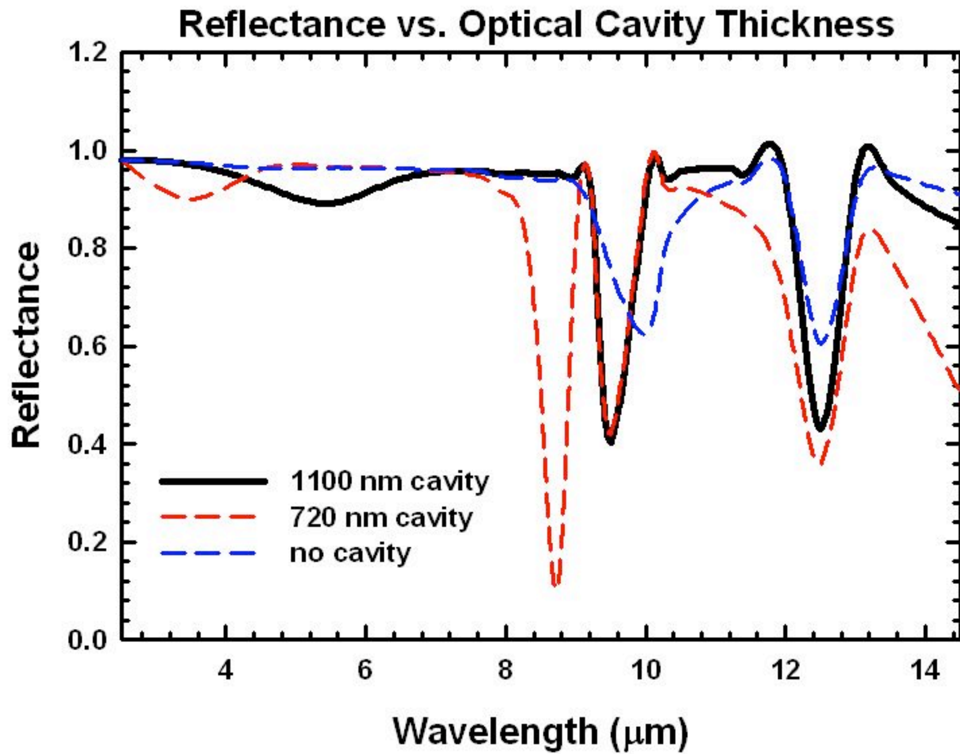

Figure 48 The reflection spectra calculated using generalied Rouard method[99]

Reflection of our multi-layer stack of SiO2, amorphous Si and Al is calculated for each wavelength using Rouard method generalized to account for the absorption of radiation by the stack layers. Since the last layer in the stack is Al, which is completely reflective to radiation in areas of interest, it was safe to consider all non-reflected radiation as being absorbed. Ideal absorption, according to calculation is for amorphous Si thickness of 720 nm. However, our deposition yielded 1100 nm film thickness so the model has been adjusted for better correspondence with the experimental observations.

Six resonant modes have been determined by performing the modal analysis for the structure. The first (lowest) and second resonant frequencies in case of detectors without self-leveling were found to be 2.78 kHz and 2.79 kHz, respectively. As in the case of detectors without a cavity, both of these modes are longitudinal, causing the absorber to oscillate out of the plane of the array. The modes are illustrated in Figures 49 and tabulated in Table 6. The third and fourth modes are antisymmetric, causing the torsional oscillations of the absorber. The fifth and sixth modes are mainly oscillations of the legs and do not cause significant movement of the absorber. Even though the resonance frequencies are lower due to the decreased thickness as well as the increased mass of the absorber, the nature of those corresponds to resonant modes of the detector discussed in Chapter 7.

In addition to FEA, a simplified analytical model was evaluated that relied on the effective spring constant *k* determined from the FEA model by applying the force of 1 nN on the tip of the absorber and recording the resulting displacement. The force of 1 nN resulted in the displacement of 130.8 nm. Hence, the effective spring constant was 0.0076 N/m. By applying the formula $\omega = \sqrt{k/m}$ to the lowest resonance mode ω=17.47 x 10^3 rad/s, we found the effective suspended mass of the structure to be 2.49 x 10^{-11} kg which is higher then the effective mass of the detector without the built-in optical cavity (2.32 x 10^{-11} kg). This is also expected, as the mass of the thin layer of amorphous Si would weigh approximately 2.87 x 10^{-12} kg.

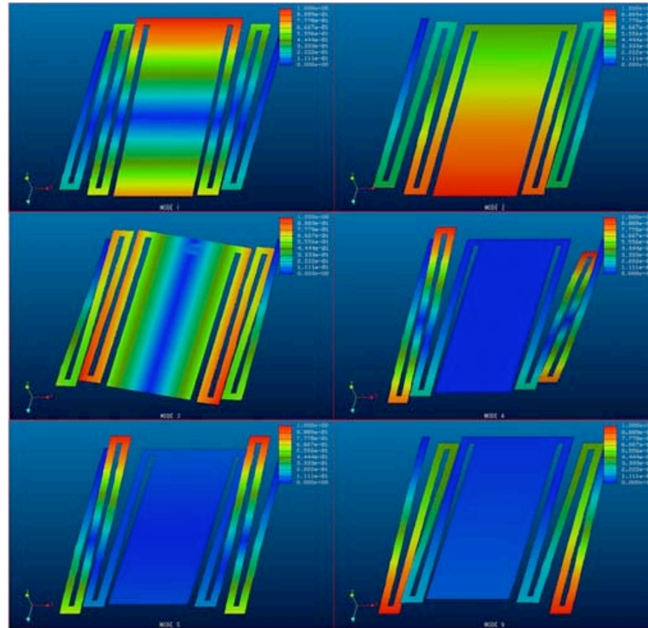

Figure 49 Deformation of the deformation-magnification structure in each of the first 6 modes of oscillation

The displacements are scaled such that the largest displacement in each mode has a magnitude of 1. These figures indicate that the higher resonant modes manifest in large displacements of the legs while the motion reflector/absorber remains minimal.

Table 6 Modeled resonant modes of deformation-magnification structure with cavity

Mode	1	2	3	4	5	6
Frequency (kHz)	2.78	2.79	8.81	14.94	15.26	15.86

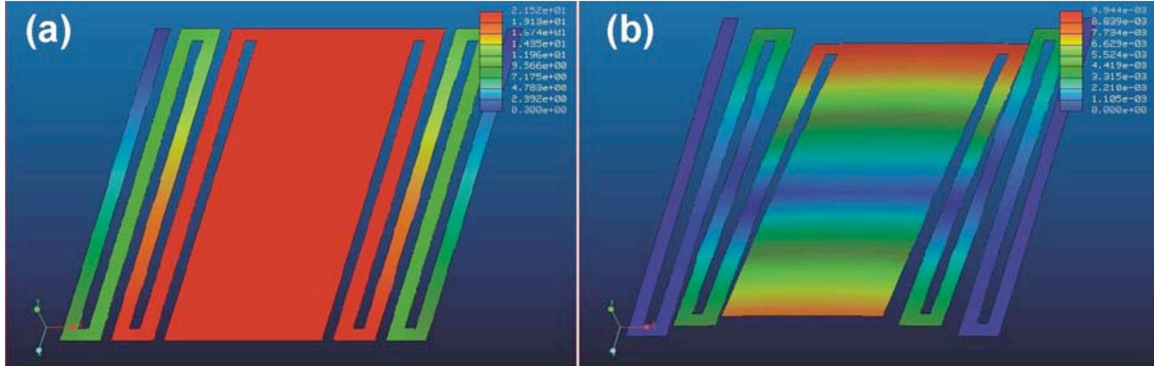

Figure 50 Thermal analyis of deformation-magnification detectors
(a) Temperature distribution caused by the 1 μW heat flux over the area of the absorber. Colors in this figure represent the increase in temperature This figure indicates that the temperature gradient is completely spread over the thermal isolation regions, while bimaterial regions remain isothermal due to large thermal conductivity of the metal layer. Figure also indicates that the outer bimaterial region experiences about one half of the temperature increase of the inner bimaterial regions and the absorber. (b) Thermal deflection (in mm) caused by the temperature distribution shown in figure (a). Colors in this figure indicate the magnitude of displacement from the plane of the detector.

Thermal analysis of the FEA model provided the values of thermal conductance between the central portion of the absorber and the substrate. The thermal conductance was obtained by applying an incoming heat flux of 1 μW evenly distributed over the area of the absorber. The resulting temperature gradient in the whole structure relative to the heat sink is shown in Figure 50a. As can be seen in Figure 50a, 1 μW of power induces the temperature difference of 21.52 K between the absorber and the substrate (heat sink). As in the previous chapter, it can be seen from Figure 50a that, due to the high thermal conductance of the metal film, all metalized regions (including the absorber) are isothermal. This results in the temperature gradient being distributed over the thermal isolation regions. And since the isolation legs 2 and 4 are of the same length, their temperature gradients need to be identical making the temperature of the bimaterial leg 1 is twice the temperature of bimaterial leg 2. This can be verified by checking the temperatures corresponding to the colors of the bimaterial legs in Figure 50a. The total temperature difference between the absorber and heat sink yields a thermal conductance of 4.65×10^{-8} W/K between the absorber and the substrate. The model only considered thermal conductance through the supporting structure and did not include heat loss through convection and radiation. The thermal conductance through the legs is slightly lower then in case of detectors without optical cavity due to lower thickness of the main structural material then in the previous case.

The parameters obtained as described above were then used in the dynamic (deflection) analysis (Figure 50b). As can be seen in Figure 50b, the largest deflection is experienced by the absorber. The tip of the structure deflects out of its plane by 9.94 μm at ΔT of 21.52 K. This corresponds to thermo-mechanical sensitivity of 462 nm/K. It can be seen that the back end of the absorber rises above the plane of the detector, while the front end falls below the plane. The corresponding deflection angle was calculated by obtaining the absolute distance between the two ends of the absorber, in a direction perpendicular to the plane of the detector, and dividing it by the absorber length. In the case of ΔT of 21.52 K, the deflection angle was found to be 8.8×10^{-2} rad. Dividing the deflection angle by the temperature increase on the absorber, the sensitivity of 4.1×10^{-3} rad/K was obtained. This is now over 70% improvement compared to the theoretical predictions for a similarly sized and shaped SiN_x structure reported previously [53]. When compared with detectors without built-in optical cavities discussed in the previous chapter, one can see two things. First, the introduction of the optical cavity improved the temperature sensitivity. This improvement is mainly due to the improved thermal capacity of the absorber by introducing another layer into the absorber but also due to the absorber becoming more rigid due to the additional layer. Note that this model does not account for the improvement in the absorption in the 8-14 μm wavelength band as it assumes identical incoming powers of 1 μW onto the absorber. This means that the actual sensitivity to infrared radiation of room-temperature objects would be improved even further. Comparing Figures 37b and 50b, one can see that the improved rigidity improves the angle deformation of the absorber plane as its backside rises further then the backside of the detector without optical cavity, making this design more appropriate for optical readout as it introduces less of unwanted lensing effect.

The tip deflection and deformation angle per unit temperature can also be obtained by using Equations 12b and 13 along with material properties from Table 1 and detector dimensions. The assumption of the flat absorber is completely appropriate here. The tip deflection is calculated using Equation 75 discussed in the previous chapter. These values should be identical to those for the deformation magnification structure without a cavity since the bimaterial regions responsible for the deformation are identical in both cases. The performance improvement is expected to be proportional to the increase in temperature rise on the absorber, which is not considered in this calculation. The calculated values for tip displacement per unit temperature and angle of deformation per unit temperature were 522 nm/K and 5.22×10^{-3} rad/K respectively. As in the previous case, the vertical tip displacement estimate is slightly higher then the one obtained using the finite element model since Equation 75 is a slight overestimate due to the complex geometry (see Appendix). Estimating the deformation angle at the tip is simpler, and for the flat absorber as in this case, the deflection of the whole absorber will be equal to the deflection at the tip of the detector. This value is closer to the estimate obtained by dividing the vertical distance of a curved absorber divided by its length as the absorber is flatter in this case.

Finally, the thermal time constant of the detector was obtained by using Equation 3. A heat capacity C of 3.39×10^{-8} J/K for the absorber was obtained by using the dimensions provided in Figure 47 and material properties from Table 1. Equation 3 then provides the predicted thermal time constant of 730 ms based on the thermal conductance

through the legs only. In order to compare this design with other similar uncooled detectors, its fundamentally limited performance were estimated expressed in terms of noise equivalent power (*NEP*), normalized detectivity D^* and noise equivalent temperature difference (*NETD*). Equations 31, 35 and 77 have been used to calculate *NEP*. Using the modeled values specified above, the optics parameters such as transmission $\tau_0 = 0.5$ and $F = 1$, the detector geometry and absorption coefficient $\eta = 0.7$ (increased compared to the previous chapter due to optical cavity), and assuming a $Q = 100$, the following values were obtained: $NEP_{TF} = 3.85 \times 10^{-12}$ W, $NEP_{BF} = 7.18 \times 10^{-12}$ W and $NEP_{TM} = 1.77 \times 10^{-12}$ W.

The combined *NEP* of the detector due to temperature fluctuations, background fluctuations and thermomechanical oscillations was obtained using Equation 78. The total *NEP* predicted by the model was 8.33×10^{-12} W.

To calculate D^*, Equations 32, 36 and 79 were used. Using the same parameters as for *NEP*, the following values were obtained: $D^*_{TF} = 1.89 \times 10^{10}$ Jones (cmHz$^{1/2}$W^{-1}), $D^*_{BF} = 1.01 \times 10^{10}$ Jones and $D^*_{TM} = 4.11 \times 10^{10}$ Jones. The combined D^* of the detector due to temperature fluctuations, background fluctuations and thermomechanical oscillations was obtained using Equation 7, and is predicted to be 8.72×10^{9} Jones.

To calculate *NETD*, we used the Equations 33, 37 and 80. Using the modeled values specified above, the following values were obtained: $NETD_{TF} = 0.67$ mK, $NETD_{BF} = 0.88$ mK and $NETD_{TM} = 0.31$ mK. The combined *NETD* of the detector due to these three sources is obtained using Equation 81 to be 1.14 mK:

8.1.2 Self Leveling Detectors

The second model of this detector has a different relative arrangement of isolation and bimaterial regions (Figure 51). In this design, the incremental deformation by the bimaterial region is sacrifised for better immunity to fluctuations of ambient temperature. This is accomplished by both bimaterial regions deflecting at the same time in case of uniform temperature change. The central rectangular portion of the bimaterial region is designed to provide enhanced absorption of the radiation to be detected and reflection of the probing optical beam. The extra layer will make the central absorber more rigid and less prone to thermal deformations suitable for optical probing. The overall size of the detector element was kept the same as for the detectors described in previous chapter in order for it to be sensitive to photon wavelengths of the THz range. The thicknesses of the SiO_2 structural layer and an Al coating are 900 nm and 170 nm respectively. The structure thickness was slightly reduced over the previous set of detectors in order to decrease the degree of initial stress. This design is referred to as self-leveling structure and it minimizes the effects of ambient temperature fluctuation using the fact that the angle of deformation of the absorber is equal to the difference of the angles of deformation of individual bimaterial regions. This concept is illustrated in Figure 52. The result of such arrangement is that in case of increase of the ambient temperature due to spontaneous temperature fluctuations, the temperature increase, and in turn, the

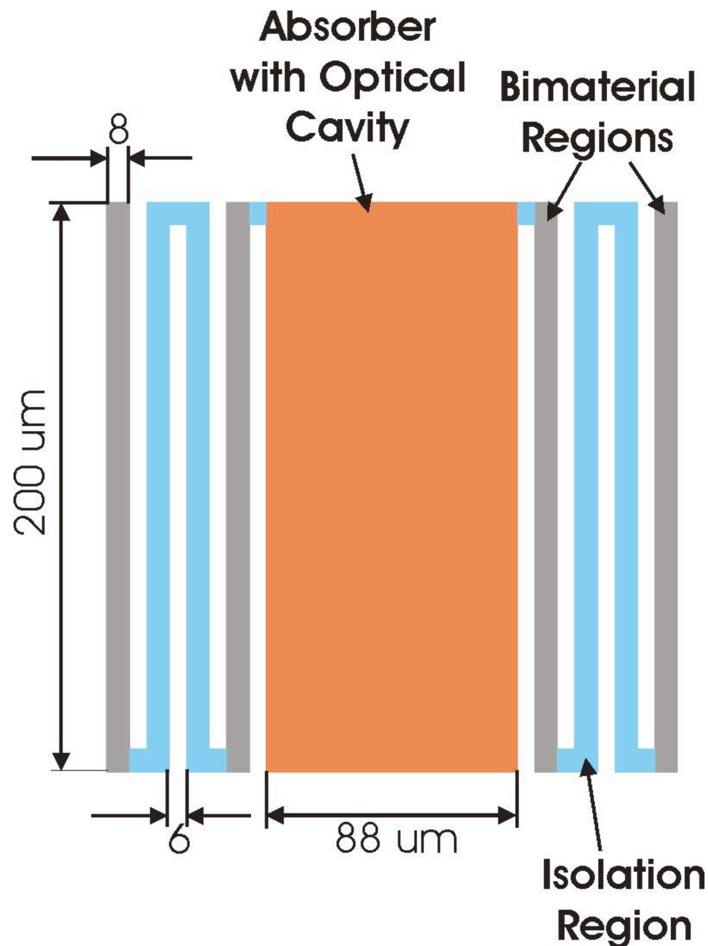

Figure 51 Illustration of geometry of the substrate-free, self-leveling design with built-in optical cavity

Dark areas represent bimaterial regions and bright areas represent the thermal isolation regions. Orange area represent the optical resonant cavity multi-layer stack of SiO_2, amorphous Si and Al as the absorber/reflector. This design also maximizes the absorption of IR radiation by incorporating additional layer of amorphous Si into the absorber, between the structural layer of SiO_2 and Al thin film. The bimaterial and isolation regions are arranged to minimize the oscillations due to ambient temperature fluctuations.

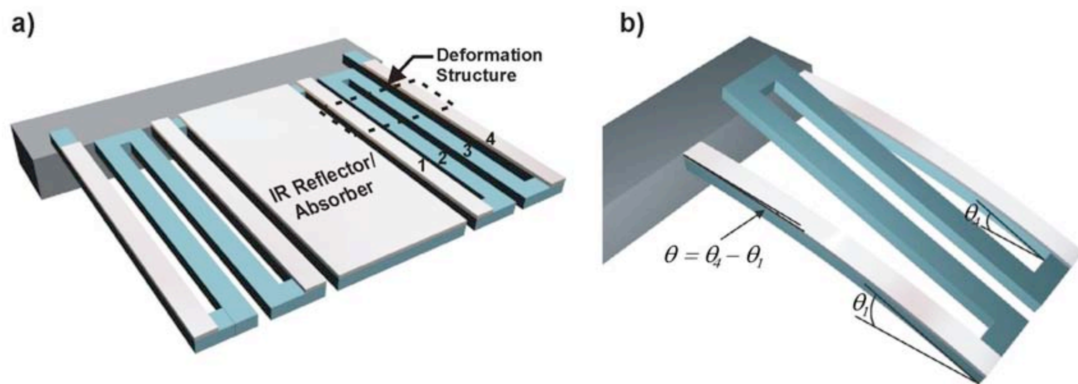

Figure 52 Illustration of addition of individual bimaterial region's deformation angles for self-leveling structure

The deformation angle of the reflector is equal to the difference of the deformation angles of the bimaterial regions on legs 1 and 4. Because of this arrangement, in case of equal temperature increase of both bimaterial regions, which would occur during ambient temperature fluctuations, the reflector should remain undeformed.

deformation angle on both bimaterial regions will be identical making the total deformation angle of the absorber zero.

The key thermal and mechanical parameters of this structure were initially determined by conducting the Finite Element Analysis (FEA). The material properties used in the model are provided in Table 1. The 1100 nm was used as thickness of amorphous Si layer for this model. The reflectance curve calculated for this thickness, obtained using Equation 82, is displayed in Figure 48.

Six resonant modes have been determined by performing the modal analysis for the structure. The first (fundamental) and second resonant frequencies in case of detectors without self-leveling were found to be 2.74 kHz and 2.75 kHz, respectively. As in the previous cases, both of these modes are longitudinal, causing the absorber to oscillate out of the plane of the array. The modes are illustrated in Figure 53 and tabulated in Table 7. The third and fourth modes are antisymmetric, causing the torsional oscillations of the absorber. The fifth and sixth modes are mainly oscillations of the legs and do not cause significant movement of the absorber. Even though the resonance frequencies are lower due to the decreased thickness as well as the increased mass of the absorber, the nature of those resonant modes corresponds to the modes of the detector discussed in Chapter 7.

In addition to FEA, a simplified analytical model was evaluated that relied on an effective spring constant k determined from the FEA model by applying the force of 1 nN on the tip of the absorber and recording the resulting displacement. The force of 1 nN resulted in the displacement of 140.2 nm. Hence, the effective spring constant was 0.0071 N/m. By applying the formula $\omega = \sqrt{k/m}$ to the lowest resonance mode ω=17.2 × 10^3 rad/s, the effective suspended mass of the structure was 2.4 × 10^{-11} kg which is also higher then the effective mass of the detector without the built-in optical cavity (2.32 x 10^{-11} kg).

Thermal analysis of the FEA model provided the values of thermal conductance between the central portion of the absorber and the substrate. The thermal conductance was obtained by applying an incoming heat flux of 1 μW evenly distributed over the area of the absorber. The resulting temperature gradient in the whole structure relative to the heat sink is shown in Figure 54a. As can be seen in Figure 54a, 1 μW of power induces the temperature difference of 21.71 K between the absorber and the substrate (heat sink). As in the previous cases, it can be seen from Figure 54a that, due to the high thermal conductance of the metal film, all metalized regions (including the absorber) are isothermal. This results in the temperature gradient being distributed over the thermal isolation regions. Since the bimaterial leg 4 is connected to the heat sink, it is isothermal and of the same temperature as a heat sink (meaning with 0 temperature increase over heat sink in case of power absorbed by the absorber). This means that it will not contribute to the absorber deflection in case of absorbing infrared radiation. This further justifies assumption that temperature increase due to the incoming ratiation is modeled by temperature increase of the absorber only.

Table 7 Modeled resonant modes of the self-leveling structure with cavity

Mode	1	2	3	4	5	6
Frequency (kHz)	2.74	2.75	9.01	15.56	15.60	16.97

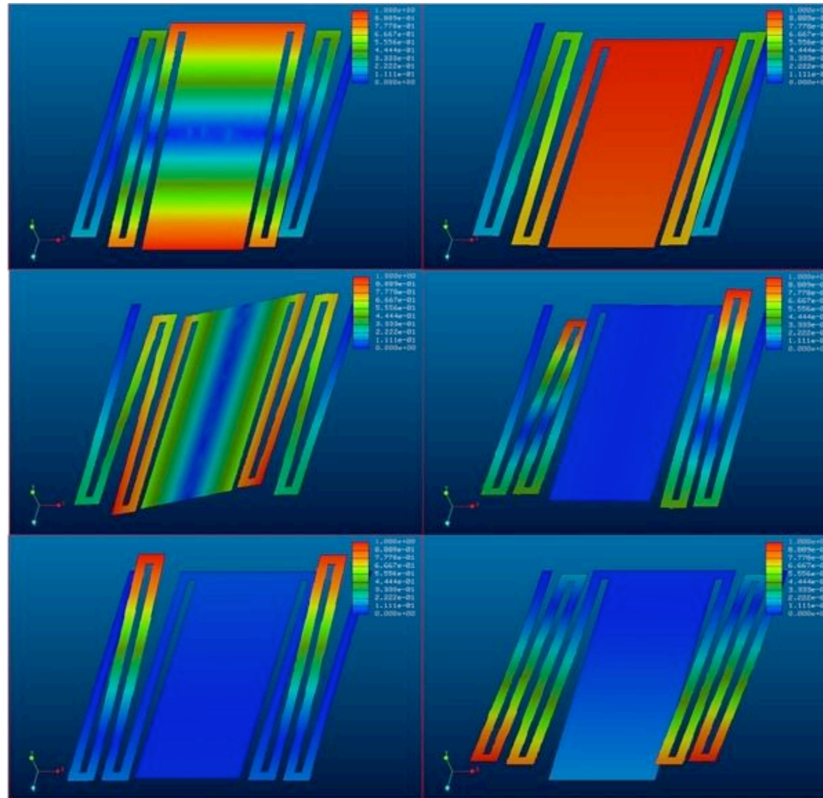

Figure 53 Deformations of the structure in each of the first 6 modes of oscillation for the self-leveling detector
The displacements are scaled such that the largest displacement in each mode has a magnitude of 1. These figures indicate that the higher resonant modes manifest in large displacements of the legs while the motion reflector/absorber remains minimal.

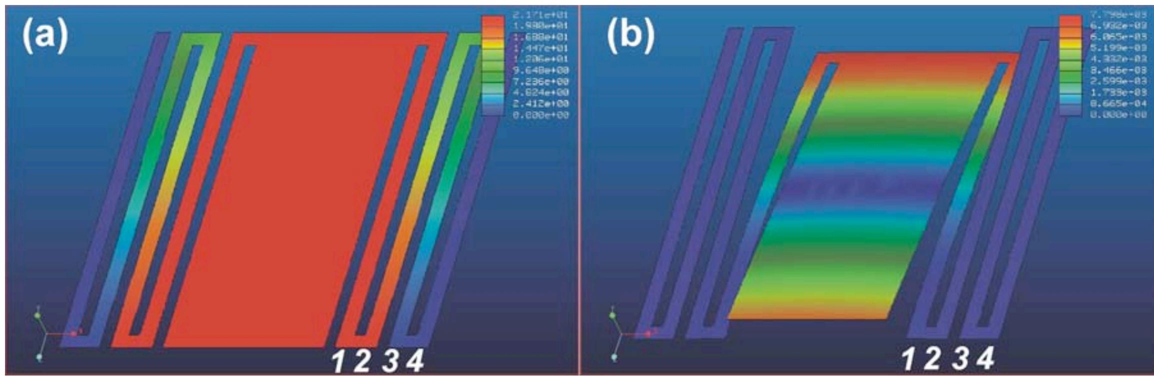

Figure 54 Thermal analysis for a self-leveling detector
(a) Temperature distribution caused by the 1 μW heat flux over the area of the absorber. Colors in this figure represent the increase in temperature. This figure indicates that the temperature gradient is completely spread over the thermal isolation regions, while bimaterial regions remain isothermal due to large thermal conductivity of the metal layer. Figure also indicates that the outer bimaterial region experiences no temperature increase as it is connected to the heat sink. (b) Thermal deflection (in mm) caused by the temperature distribution shown in figure (a). Colors in this figure indicate the magnitude of displacement from the plane of the detector.

Since the isolation legs 2 and 3 are connected, the complete temperature gradient of 21.71 K is distributed over them and temperature increase of the bimaterial leg 1 is almost equal to the temperature increase of the absorber while temperature increase of bimaterial leg 4 is 0 K. This can be verified by checking the temperatures corresponding to the colors of the bimaterial legs in Figure 54a. The total temperature difference between the absorber and heat sink yields a thermal conductance of 4.61×10^{-8} W/K between the absorber and the substrate. As expected, this value is almost the same as the one for deformation magnification structure, as the total lengths of bimaterial regions are identical in both cases. The model only considered thermal conductance through the supporting structure and did not include heat loss through convection and radiation. It was expected for these values to be very similar to those for the detectors without self leveling. This is because, even though the relative arrangement of isolation and bimaterial sections is different, the total length of bimaterial and isolation regions separating the absorber and the heat sink is the same (Figures 47 and 51).

The parameters obtained as described above were then used in the dynamic (deflection) analysis (Figure 54b). As can be seen in Figure 54(b), the largest deflection is experienced by the absorber. The tip of the structure deflects by 7.8 μm at ΔT of 21.71 K. This corresponds to thermo-mechanical sensitivity of 359 nm/K. It can be seen that the back end of the absorber rises above the plane of the detector, while the front end falls below the plane. The corresponding deflection angle was calculated by obtaining the absolute distance between the two ends of the absorber, in a direction perpendicular to the plane of the detector, and dividing it by the absorber length. In the case of ΔT of 21.52 K, the deflection angle was found to be 6.9×10^{-2} rad. Dividing the deflection angle by the temperature increase on the absorber, the sensitivity of 3.2×10^{-3} rad/K was obtained. In case of heating the absorber, as seen in Figure 54b, three outer legs on both sides show little deformation. The only bimaterial region that experiences temperature increase significant enough to cause the deformation is the one closest to the absorber. The outmost leg is well thermally isolated from the temperature increase of the absorber through two isolation legs and is close to the heat sink so it experiences almost no deformation.

The tip deflection and deformation angle per unit temperature can also be obtained by using Equations 12b and 13 directly, as there is only one bimaterial region contributing to the absorber deflection and the other one is connected directly to the heat sink and has zero temperature increase. Using the material properties from Table 1, and detector geometry, the values for tip displacement per unit temperature and angle of deformation per unit temperature were 348 nm/K and 3.48×10^{-3} rad/K respectively. These are very close to the values obtained using the finite element model. The assumption of the flat absorber is completely appropriate here as well.

Finally, the thermal time constant of the detector was obtained by using Equation 3. A heat capacity C of 3.39×10^{-8} J/K for the absorber was obtained by using the dimensions provided in Figure 51 and material properties from Table 1. Equation 3 then provides the predicted thermal time constant of 736 ms based on the thermal conductance through the legs only.

In order to compare this design with other similar uncooled detectors, its fundamentally limited performance was estimated expressed in terms of noise equivalent

power (NEP), normalized detectivity (D^*) and noise equivalent temperature difference ($NETD$). To calculate NEP, we used Equations 31 and 35. For estimating the NEP_{TM} the Equation 77 that multiplies Equation 43 a factor of by two could not be used. To get an estimate of the amplitude of oscillation due to thermo-mechanical noise Equation 40 that describes the spontaneous oscillations of bimaterial cantilevers (rms noise) needed to be considered. This formula applies to bimaterial legs 1 and 4 of the self-leveling structure. Figure 55b that describes structure deformation due to temperature increase can be used to estimate what the deflection of the tip of the absorber is in that case. From the Figure 55b, we see that at the maximum deflection of the bimaterial regions, 414 nm, the tip of the absorber moves 120 nm, or 0.29 times that deflection. Therefore, in order to estimate the motion of the absorber/reflector due to the thermo-mechanical noise, we multiplied the amplitude of the rms noise of the bimaterial region by 0.29 in our $NETD$ calculations. Note that in this case there is no addition of the deflections of individual bimaterial regions as they deform in parallel and do not enhance each other. The Equation 43, therefore, becomes:

$$NEP_{TM} = \frac{0.29}{R(\omega)}\sqrt{\frac{4k_B TB}{Qk\omega_0}}, \tag{85}$$

Using the modeled values specified above, the optics parameters such as transmission $\tau_0 = 0.5$ and $F = 1$, the detector geometry and absorption coefficient $\eta = 0.7$ (increased compared to the previous chapter due to optical cavity), and assuming a $Q = 100$, the following values were obtained: $NEP_{TF} = 3.83 \times 10^{-12}$ W, $NEP_{BF} = 7.18 \times 10^{-12}$ W and $NEP_{TM} = 3.43 \times 10^{-13}$ W.

The combined NEP of the detector due to temperature fluctuations, background fluctuations and thermomechanical oscillations was obtained using Equation 78. The total NEP predicted by the model was 8.14×10^{-12} W.

To calculate D^*, we used Equations 32 and 36. For estimating the D^*_{TM}, the Equation 44 needed to be modified by factoring out 0.29 since D^* is inversely proportional to the rms amplitude of noise (Equation 40) which we have multiplied by the factor of 0.29. The expression used is given below.

$$D^*_{TM} = \frac{R(\omega)}{0.29}\sqrt{\frac{Qk\omega_0 A_d}{4k_B T}} \tag{86}$$

Using the same values as for the NEP calculation, the following values have been obtained: $D^*_{TF} = 1.9 \times 10^{10}$ Jones (cmHz$^{1/2}$W^{-1}), $D^*_{BF} = 1.01 \times 10^{10}$ Jones and $D^*_{TM} = 2.12 \times 10^{10}$ Jones. The combined D^* of the detector due to temperature fluctuations, background fluctuations and thermomechanical oscillations was obtained using Equation 7, and is predicted to be 8.92×10^9 Jones.

Equations 33 and 37 were used to calculate the $NETD$. For estimating the $NETD_{TM}$, the Equation 45 needed to be modified by the factor of 0.29 as described

$$NETD_{TM} = \frac{1.16F^2}{\tau_0 A_d R(\omega)\left(\frac{dP}{dT}\right)_{\lambda_1-\lambda_2}}\sqrt{\frac{4k_B TB}{Qk\omega_0}}. \tag{87}$$

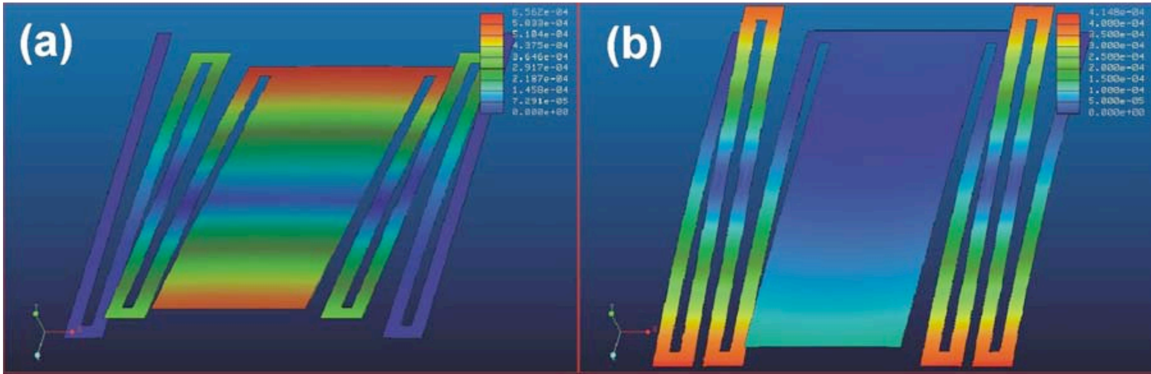

Figure 55 Comparison of responses of two detectors due to ambient temperature increase

Deformation-magnification detector when the ambient temperature is increased by 1 K. This figure indicates even larger magnitude of deformation then when the incoming radiation is absorbed by the absorber. This is because in this case, both bimaterial region experience equal temperature increase; b) self-leveling detector when the ambient temperature is increased by 1 K. Even though the magnitude of deformation of the legs is large, the reflector remains fairly level making the ambient temperature fluctuations not detectable by the readout.

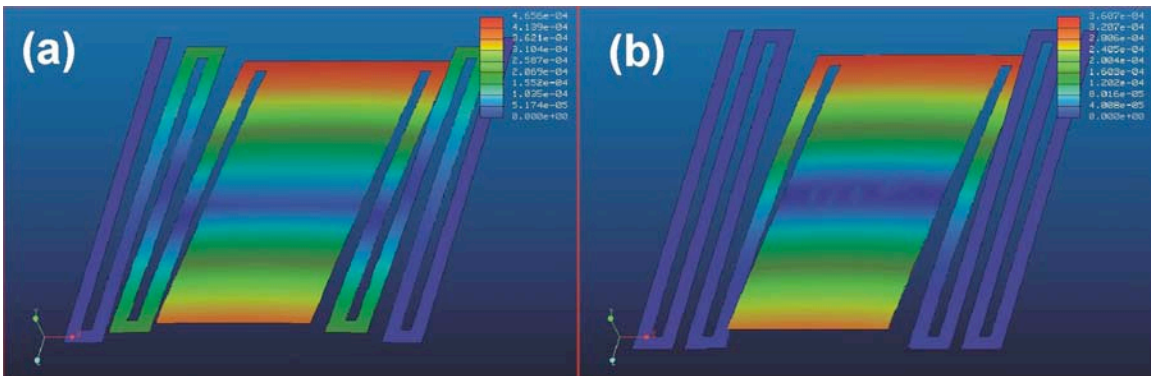

Figure 56 Comparison of responses of two detectors due to absorber temperature increase

a) Deformation-magnification detector when absorber temperature is increased by 1 K.; b) self-leveling detector when absorber temperature is increased by 1 K. This figure indicates that reflector of self-leveling detector experiences smaller deformation. This is because only inner bimaterial regions experience the temperature increase, while outer bimaterial regions are in thermal equilibrium with the heat sink due to close proximity and experience no temperature increase.

above.Using the same values as for the *NEP* calculation, the following values have been obtained: $NETD_{TF}$ = 0.66 mK, $NETD_{BF}$ = 0.88 mK and $NETD_{TM}$ = 0.06 mK. The combined *NETD* of the detector due to these three sources is obtained using Equation 81. Total *NETD* predicted by the model is 1.10 mK. These values show that the expected total *NETD*s are very similar for deformation-magnification structure and self-leveling structure. This has already been discussed by Guo et al. [50] who explained that even though the deformation-magnification structure has higher levels of noise, its higher responsivity compensates for it and the *NETD* (Equation 25) is comparable to that of the self-leveling structure.

8.1.3 Comparison of Two Designs

To best compare the two designs, the deflection due to the increase in temperature of the just absorber should be compared to the deflection due to ambient temperature increase. Figure 56 shows modeled deformations of two types of detectors in case the temperature of the absorber has increased by 1 K. Figure 56a shows the deformation-magnification detector and Figure 56b shows the self-leveling detector. It can be seen from Figure 56 that tip displacements of 465 nm/K and 361 nm/K for non-self leveling and self-leveling detectors, respectively, are consistent with the one obtained previously when 1 μW of power has been applied to the absorber only (462 nm/K and 359). The angular per-degree-kelvin deflections of 4.14×10^{-3} rad/K and 3.2×10^{-3} rad/K also correspond well to the previously obtained results.

From Equations 14 and 19, one can see that the temperature increase is directly proportional to the area of the object and inversely proportional to the thermal conductance between the object and a heat sink. The absorber has the largest area and has the lowest thermal conductance between itself and the heat sink (Si frame) since it is farthest away from it. It is, therefore, safe to assume that the increase in the absorber temperature is going to be the highest compared to the temperature increase of the rest of the detector even though the whole detector is irradiated with the same incoming radiation flux. In addition, the rest of the detector does not have an optical cavity and the calculations using Rouard method predicts lower absorption for those areas. For all these reasons, modeling the case of temperature increase as just increase of the absorber should give the results that are close to the situation when the temperature increase is due to the incoming radiation alone.

To best model the noise behavior of the two designs, we need to consider their behavior if the temperature of the whole object was uniformly increased. This is a valid approximation as temperature changes due to noise are much slower compared totemperature changes due to the incoming IR radiation [50]. If we now consider the increase of overall ambient temperature by 1 K shown in Figure 55 for both of the detectors, we can see that the non-self-leveling detectors (Figure 55a) exhibit deformation of 656 nm/K (6.19×10^{-3} rad/K) which is even larger then 465 nm/K (4.14×10^{-3} rad/K) in case of heating the absorber alone. This can be explained by the fact that the temperature distribution, in case of just heating the absorber, results in outer bimaterial

regions being at lower temperature increase (more specifically one half, as discussed in the previous chapter) then the absorber and inner bimaterial regions. In case of slow, ambient temperature increase, the temperature raise is uniform across the whole detector. Also the tip displacement of 656 nm is close to 1.5 times the displacement of 465 nm which further justifies the assumption of temperature increase on inner bimaterial region being twice that of the increase on the outer bimaterial regions of deformation-magnification detector. The estimate above corresponds well with calculations using Equation 13 and assuming equal ΔT of 1 K on all bimaterial regions. The total angular deflection of the reflector, $\Delta\theta$, being a sum of angular deformations of individual bimaterial regions, then becomes $2\Delta\theta_1$ and the result is a sensitivity of 6.96×10^{-3} rad/K. In case of self-leveling detector (Figure 55b), it is apparent that the total deformation of the absorber/reflector is about 120 nm/K (7.5×10^{-4} rad/K) which is significantly less then both tip deflection in case of deformation-magnification detector in the same case and tip deflection due to signal which is modeled by heating the absorber only. The figure shows that bimaterial regions do deform but by the same amount which results in zero-net-motion of the absorber itself. The conclusion from this analysis is that the self-leveling detector will be more resistant to noise due to ambient temperature fluctuations.

Guo et al. [50], however, have found that detectors with and without implemented self leveling exhibit similar *NETD* levels. This is explained by the fact that even though the deformation-magnification have higher sensitivity, they have a higher noise levels while less responsive self-leveling detectors have less fluctuations due to fluctuations in ambient temperature. Hence, the signal-to-noise ratios are similar.

8.2 Implementation

After determining the detector dimensions that provided the optimal parameters using FEA, the arrays have been fabricated in order to characterize individually as well as to employ in an optical readout system. Since the scalability to much larger arrays for substrate-free detectors has already been demonstrated in previous chapter, and for the detector arrays to be suitable for a vacuum cell application, the new mask was subdivided into several smaller rectangular arrays of 120 × 120 and 100 × 100 detectors. The same mask featured arrays of both deformation-magnification and self-leveling detectors.

This fabrication involved an additional photolithographic process compared to the fabrication of the detectors without a built-in optical cavity. Fabrication of these FPAs involved a total of four photolithographic processes. As in the previous case, the wet etching was avoided completely.

The process flow is shown in Figure 57. Note that the number of bimaterial and isolation regions has been reduced in these illustrations for simplification purposes. Initially, about 0.9 μm of SiO_2 was grown on 300-μm-thick double-side-polished (DSP) Si wafers (Figure 57a) using PECVD process at 300 ºC. A 1.1 μm amorphous, undoped Si layer has been deposited on top of each of the structural oxide layers at 300 ºC (Figure 57a). A mask layer of 2 μm SiO_2 has been deposited on the backside of each wafer (Figure 57a). The first photolithography has been used to pattern a mask in the backside

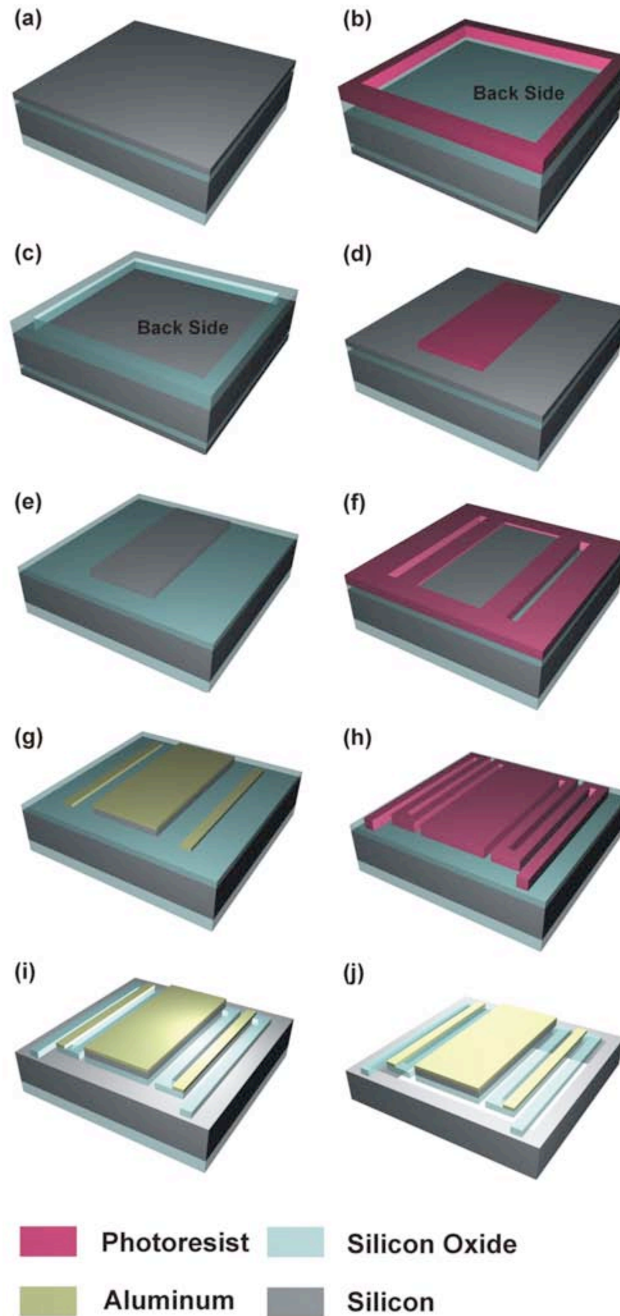

Figure 57 Process flow for completely dry microfabrication process of substrate-free detector arrays featuring built-in optical cavity

a) Start by coating double-side-polished (DSP) Si wafer by a structural SiO_2 layer, and layer of amorphous Si on top as well as mask SiO_2 layer on bottom; b) backside mask for patterning the back-side windows in the SiO_2 layer; c) SiO_2 after etching; d) front side mask to pattern the optical cavity in amorphous Si; e) cavity after etching f) front side mask for liftoff metallization; g) metallization regions after liftoff; h) front side mask to pattern the structure in SiO_2 i) structure before release j) structure after release

oxide layer for the holes to be DRIE etched underneath each detector at the end of the process. Reactive ion etching of SiO_2 has been performed to create this oxide mask (Figures 57b and 57c). The second photolithography was used to pattern the cavities in the amorphous Si layer. A short deep reactive ion etch has been used in this step (Figures 57d and 57e). The third photolithography was used for a liftoff metallization after e-beam evaporation of 170 nm Al film to pattern the bimaterial regions (Figures 57f and 57g). Finally, the fourth photolithography was used to pattern the structures into the SiO_2 layer (Figures 57h and 57i). The process was completed by deep reactive ion etching (DRIE) from the backside using the 2 μm SiO_2 mask created in the beginning of the process (Figure 57j). It was performed after the front side of the wafer was coated with a 7 μm film of SPR-220 photoresist and hard baked for 4 hours at 90 deg C. This step provided protection and structural integrity of the front side during the subsequent deep reactive ion etch (Bosch process). The boundaries of each hole matched the boundaries of a detector element on the front side of the wafer (Figures 57j).

Photographs of the structures obtained after each of the steps described using a microscope are shown in Figure 58. Each photograph has a corresponding illustration in Figure 57. Figures 58a through 58f correspond to Figures 57d through 57i. Figures 58g and 58h are showing the results of the same step obtained using front and backside illumination respectively, and correspond to Figure 57j.

The final fabrication step was the release of structures by etching the protective photoresist layer in oxygen plasma. Despite the fact that majority of the Si bulk was removed during the FPA fabrication, these arrays remained robust enough to allow handling.

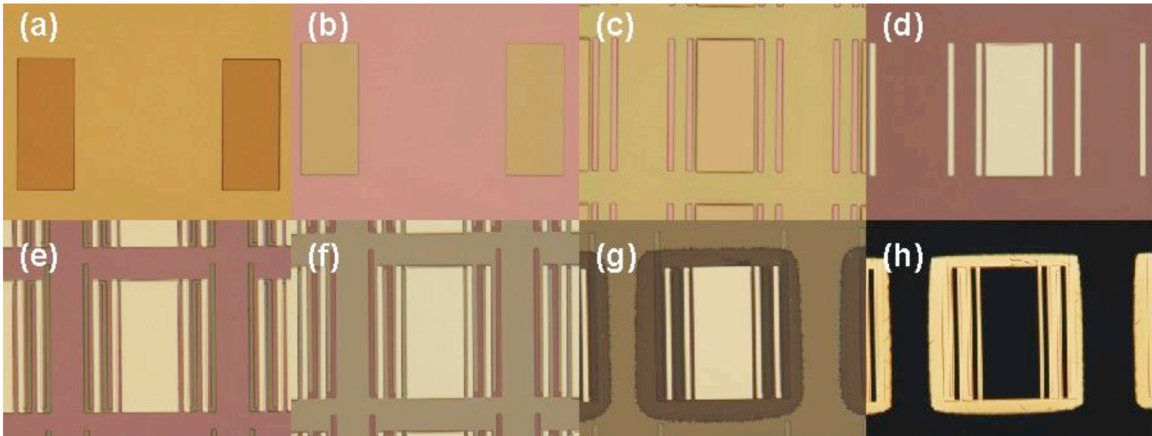

Figure 58 Microscope photographs obtained after microfabrication steps
a) Front side mask for patterning optical cavities in amorphous Si; b) cavities after etching and resist removal; c) front side mask for liftoff metallization; d) metalized regions after liftoff; e) front side mask for patterning the structures in SiO_2; f) structure before back-side etching g) complete unreleased structure illuminated from the front side; h) complete unreleased structure illuminated from the backside.

Microscope photographs of structures after oxygen plasma etch of protective photoresist layer are shown in Figure 59. They show deformation-magnification structures with front and back illumination (Figures 59a and 59b respectively) as well as self-leveling structures with front and back illumination (Figures 59c and 59d respectively). Comparing the two structures, we see that the absorber in case of self-leveling structure is almost in the plane of the FPA while the absorber of the deformation-magnification structure is slightly bent (this is apparent from the fact that the front and back edges are not both in focus). This is expected since both bimaterial regions in self-leveling detectors have identical radius of curvature no matter if it is due to temperature increase or intrinsic stress. Therefore, the leveling concept can also be applied to minimize the effects of intrinsic stress. However, while this additive effect in the deformation-magnification structure increases the sensitivity, it will amplify the effect of the intrinsic stress

This effect is also apparent in the perspective-view ion micrograph (Figure 60) obtained using the focused ion beam imaging capabilities. It can be seen that, consistently with results of our model, optical cavity has made the absorber more rigid and it is almost flat and not deformed by the intrinsic stress as if it is not expected to deform due to temperature changes

8.3 Experiment and Results

As in the previous chapter, the individual detectors from both arrays have been characterized. To quantify the initial stress as well as thermal sensitivity, the optical microscope was used with test detectors mounted on a heated sample holder. By focusing the microscope on the two ends of the absorber the absolute height difference between the two ends was determined. After dividing this displacement by the absorber length, its initial angular deflection was obtained. The average angles of the room temperature deflections were 10.5º and 3.8º for the deformation-magnification and self-leveling structures respectively. The bimaterial region deformations due to intrinsic stress counter each other and the effect of deformation due to intrinsic stress is also minimized as in the case of deformation due to temperature increase. The thermal isolation regions in both structures were deformed, indicating an appreciable stress gradient in this layer as in the case of detectors without optical cavity built out of PECVD SiO_2. These measurements indicate that the initial deformation of the absorber was decreased as compared to detectors without an optical cavity. This improvement is due to much smaller deformation of the absorber due to reinforced rigidity provided by the layer of amorphous Si.

The average thermal sensitivities of the implemented structures were 7.93×10^{-3} rad/K and 7.16×10^{-4} rad/K in the case of deformation-magnification and self-leveling detectors, respectively. This correlates well with our FEA predictions. Since the measurements have been performed by placing the detectors on a slow-heating hotplate, and the measurements were being taken when the detectors were in equilibrium, the most appropriate FEA results to compare to were those where the ambient temperature was being increased.

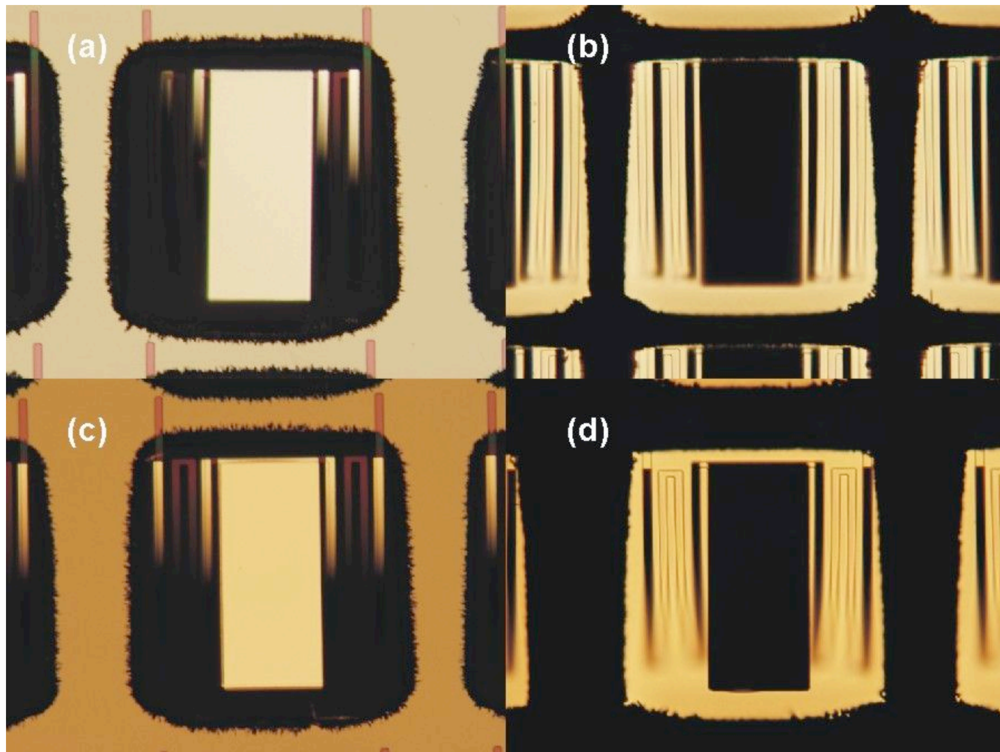

Figure 59 Microscope photographs of released detectors

a) deformation-magnification detector, top-side illumination b) deformation-magnification detector, bottom-side illumination c) self-leveling detector, top-side illumination d) self-leveling detector, bottom-side illumination

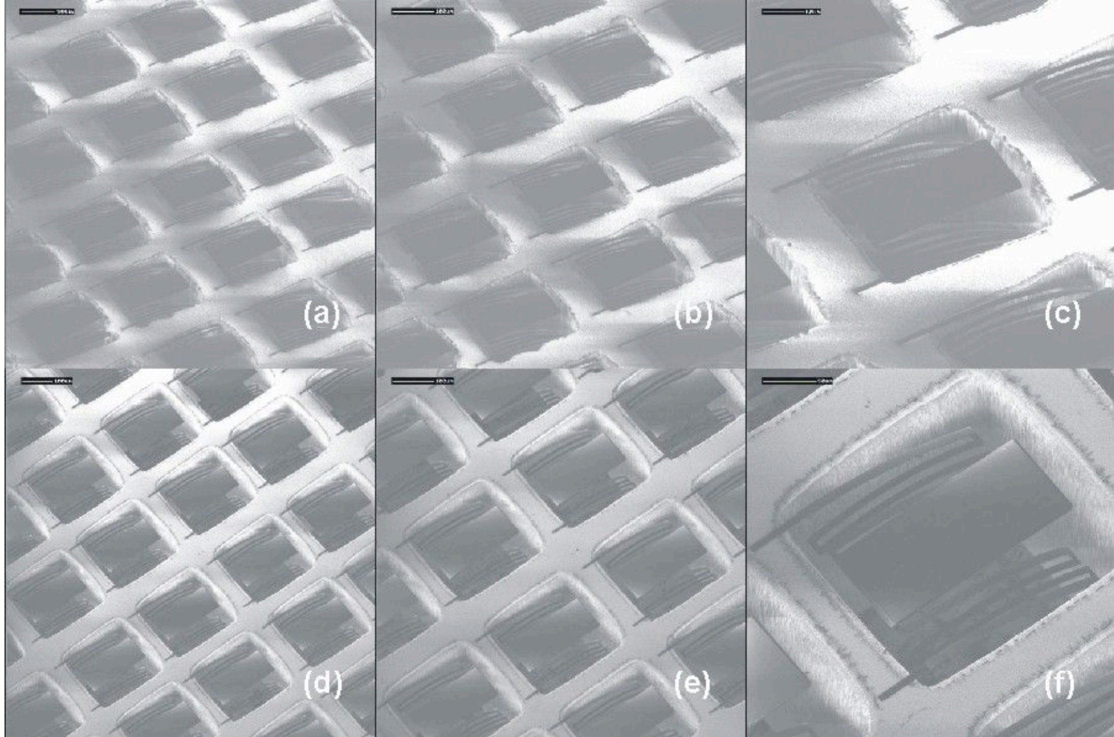

Figure 60 Ion micrograph at several magnifications showing the fabricated focal plane arrays

Parts a) b) and c) show the deformation-magnification detectors while parts d), e) and f) show the self-leveling detectors.

Resonant frequencies and thermal response times were obtained using a combination of the conventional optical lever readout described elsewhere [94] and a photothermal excitation [95]. This optical arrangement is illustrated in Figure 42. The readout diode laser is focused on the tip of a cantilever and reflected into the quad-cell position sensitive detector (PSD). The horizontal and vertical channels of the PSD correspond to the longitudinal and torsional modes, respectively. In order to measure the thermal response time, another modulated diode laser was focused on the detector and provided its photothermal excitation in case of response time measurements [95]. The square wave signal was used to modulate the laser intensity from zero to its maximum. This resulted in heating-cooling cycling of the detector. The readout laser was then used to quantify the deflection due to these temperature changes, and the resulting waveform was used to calculate the thermal response time. During these experiments, the detector array was inside the evacuated cell at 25 mTorr.

Figure 61 shows resonant frequency spectra of detector oscillations due to the spontaneous (thermo-mechanical) motion. Figures 61a and 61b show the characteristic frequency spectra for the deformation-magnification and self-leveling detectors respectively. The average measured frequencies for first several modes for the deformation-magnification detector were 2.1 kHz, 2.5 kHz and 6.6 kHz. These deviate slightly from the results obtained by the model for corresponding modes (Table 6). The

type of oscillatory motion (longitudinal or torsional), however, does correspond to the model. The average measured frequencies for first several modes for the self-leveling detector were 1.9 kHz and 6 kHz. As can be seen from Figure 57b, the frequency resolution was not sufficient to be able to tell those two frequencies apart. These also deviate slightly from the modeled values (Table 7) but their type of motion does correspond to the predicted ones. One of the reasons for lower-then-predicted resonant frequencies is that both structures investigated in this chapter were made of PECVD SiO_2 deposited at 300 ºC. This temperature was even lower then the one used for depositing the structural layer for structures discussed in Chapter 7, and those structures have already exhibited lower resonant frequencies then the model predicted. A good indicator of model accuracy, are the heights of experimentally measured resonant peaks. As can be seen in Figures 49 and 53, the modes 4 through 6, for both detectors, induce insignificant amount of motion of the reflector out of its equilibrium position (the color is blue). There is a good agreement between this prediction by the model and experimental observation since the measured peak amplitudes, corresponding to the longitudinal or torsional oscillations for higher three modes are substantially lower then those for the lower three resonant modes. For the spectrum in Figure 61b, a log-scale needed to be used since the oscillation amplitudes above the third mode was more then an order of magnitude lower then the first thee modes. This is also in agreement with the model since Figures 49d through 49f and Figures 53d through 53f indicate that the main motion is done by the legs and the reflector experiences low amplitudes of oscillation, while the motion of the reflector in the first three modes is dominant over the motion of the legs. Using the experimentally measured fundamental frequencies of the fundamental mode and the effective mass, the spring constant was calculated to be $k = \omega^2 m$ to be 0.0043 N/m and 0.0036 N/m for the deformation-magnification and self-leveling structures, respectively.

The response kinetics measured in photothermal excitation experiments is shown in Figure 62. By fitting the experimental curves to the first order exponential kinetic function, the average thermal time constants of 187 ms and 150 ms were obtained for deformation-magnification and self-leveling detector geometries, respectively. The relatively long response times are consistent with the high thermal isolation of the implemented detectors. Increasing the operating pressure of the detectors could be used to adjust their response times to less than 30 ms, which is normally required for 30 frames per second video imaging. As discussed in our previous work [15], this method of measurement could be introducing an increase in the radiative thermal conductance due to the temperature increase on the detector. This could cause the measured time constant to be shorter than the one predicted by the model. This effect could be even more pronounced then in the previous work due to the fact that the radiative thermal conductance is proportional to the detector area and detectors in Chapters 7 and 8 are of larger area then the detectors discussed in Chapter 6. Another reason for the discrepancy between these values might lie in the complexity of the structure, which has 5 separate bimaterial regions.

The experimentally obtained response times were also used to verify our estimates of the thermal conductances for two types of structures. These calculations resulted in 1.8×10^{-7} W/K and 2.3×10^{-7} W/K for the thermal conductance of the deformation-magnification structures and self-leveling structures, respectively.

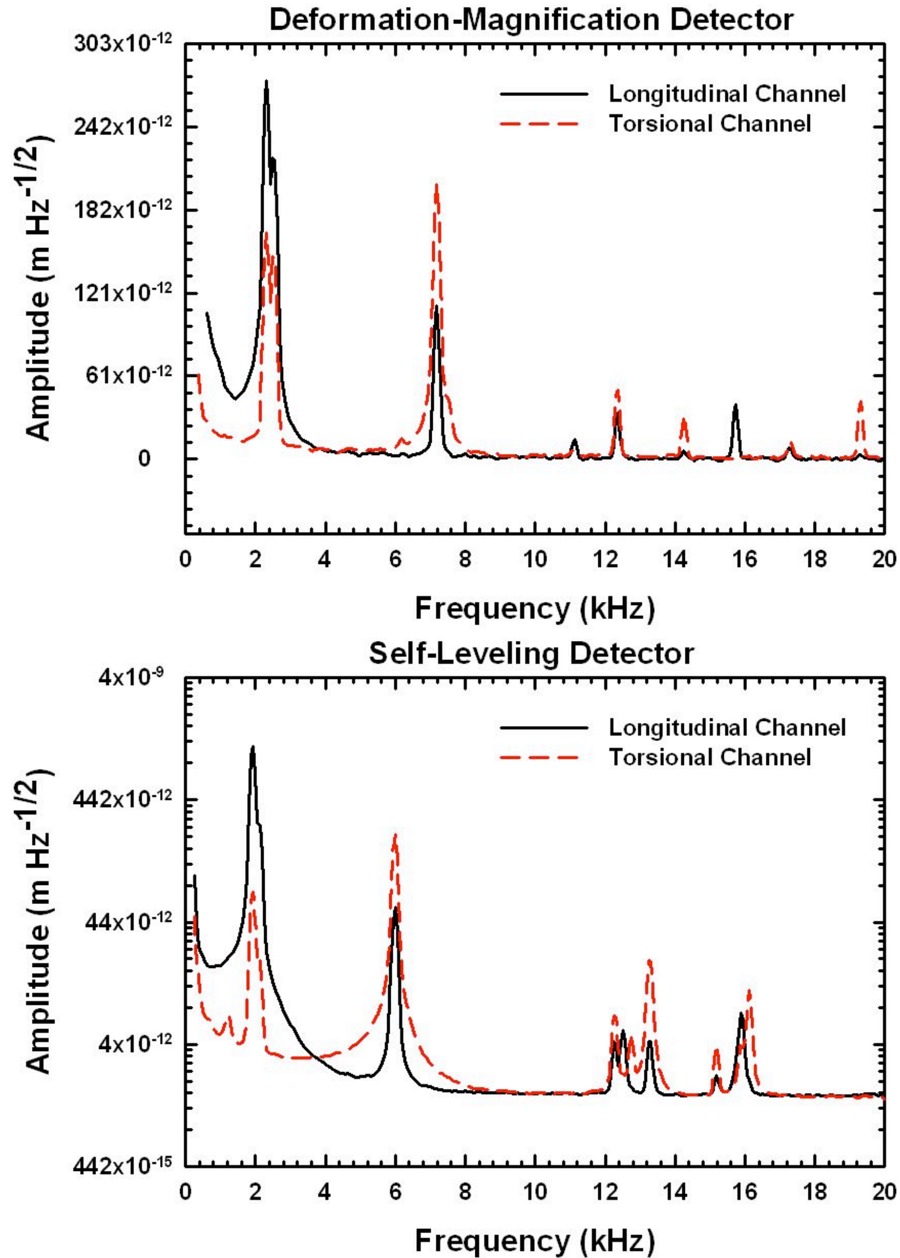

Figure 61 Frequency spectra of arrays of substrate-free detectors with optical cavity

a) deformation-magnification detector and b) self-leveling detector. The spectra indicate fundamental resonant frequencies being close to 2 kHz. There is a significant decrease in resonant frequency introduced by adding the extra resonant cavity layer due to the increase in mass. Low amplitudes for modes above the third mode are in good agreement with types of deformation predicted by the model since the largest deformations are experienced by the legs while reflectors (which were being probed for obtaining these graphs) remain fairly steady.

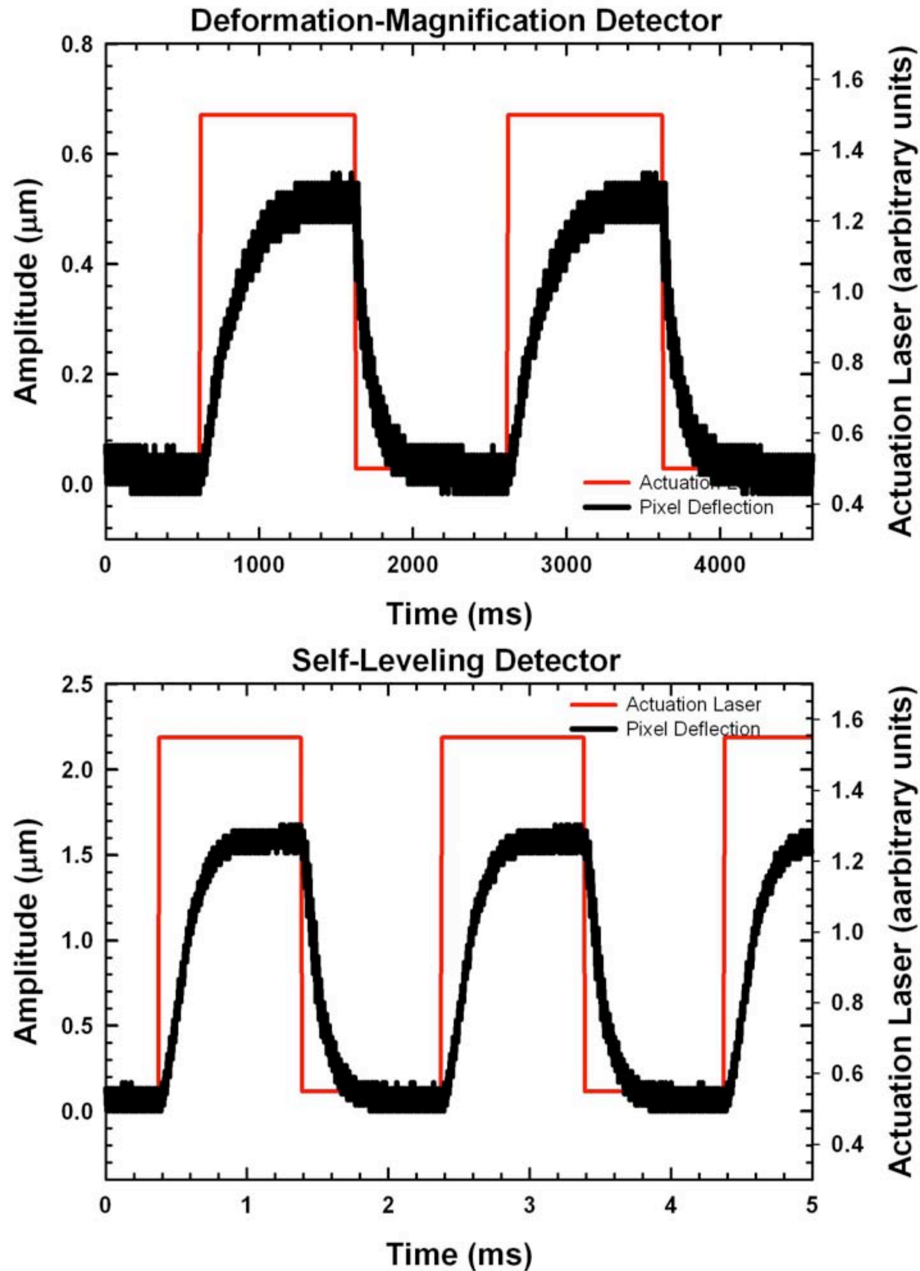

Figure 62 Thermal response times

Displacement of the tip of the detector as a function time during photothermal excitation by a diode laser modulated by a square wave signal. These data were subsequently analyzed to obtain the thermal response time. Top graph shows the deformation-magnification detector thermal response while bottom graph shows self-leveling-detector thermal response. The thermal response times of 187 ms and 150 ms were obtained for deformation-magnification detectors and self-leveling detectors respectively.

As in the previous chapter, the frequency response graph was also used in order to estimate the quality factor Q. The obtained value of 30 was even lower then that of the detectors without optical cavity, which is expected since the absorber mass was increased significantly. Finally, the obtained values of thermal conductance G, spring constant k and resonant frequency f, were used to re-iterate our estimates for the fundamentally limited *NEP*s, D^*s *and NETD*s. By using these values in Equations 31 through 37, Equations 77 through 81 and Equations 85 through 87, the following results were obtained. *NEP*s for deformation-magnification and self-leveling structures were 1.79 x 10^{-11} W and 1.17 x 10^{-11} W respectively. D^*s for deformation-magnification and self-leveling structures were 4.07 x 10^7 Jones and 6.20 x 10^7 Jones respectively. *NETD*s for non-self–leveling and self-leveling structures were 2.97 mK and 2.14 mK respectively. Similar *NETD* results between the two detector designs confirm previous findings by Guo et al. [50] that suggest that even though the deformation-magnification detectors experience higher levels of intrinsic noise, their magnified response and higher spring constant and resonant frequency compensates for that resulting in *NETD* levels similar if not better then that of self-leveling detectors. One of the advantages worth mentioning, however, is that self-leveling structure design also decreases the effect of intrinsic stress on the initial deformation of the absorber/reflector.

8.4 Summary

Results from the previous analysis are summarized in Table 8. Note that the modeled $\Delta\theta/\Delta T$ correspond to the absorber temperature increase, while measured $\Delta\theta/\Delta T$ correspond to the ambient temperature increase. After observing significantly improved performance parameters over previously reported SiN_x detectors of similar size and shape, implementing integrated imaging systems was the next step.

Table 8 Summary and comparison of finite element model and experimental results for deformation-magnification and self-leveling structures with cavities

Detectors with Cavity	Resonant frequency (kHz)	Q factor	Thermal conductance (W/K)	Response time (ms)	$\Delta z/\Delta T$ (nm/K)	$\Delta\theta/\Delta T$ (mrad/K)	NEP (pW)	D* (cmHz$^{1/2}$/W)	NETD (mK)
DMS_{model}	2.78	-	4.65×10^{-8}	730	462	4.1	8.33	8.72×10^{9}	1.14
DMS_{actual}	2.1	30	1.8×10^{-7}	187	-	7.93	17.9	4.07×10^{9}	2.97
SLS_{model}	2.74	-	4.61×10^{-8}	736	359	3.2	8.14	8.92×10^{9}	1.10
SLS_{actual}	1.9	30	2.3×10^{-7}	150	-	0.72	11.7	6.20×10^{9}	2.14

Chapter 9

Implementation and Characterization of Integrated Imaging System

After completing the characterization of individual detectors based on their geometry, material and mechanical properties, the substrate-free arrays, described in Chapter 6, were integrated into the optical system. In addition to testing the integrated system's imaging capabilities, the setup was used to complete the characterization of individual detectors once integrated into the imaging system. This characterization is important because the parameters obtained in Chapter 8 might be deceptive since readout configuration introduces a significant noise through several sources as discussed in Section 5.4.3.2. It is, therefore, only such configuration that can provide the most relevant noise and detectivity parameters. The system used was identical to the one described in Chapters 1 and 6.

Because of the initial deformations of detectors due to intrinsic stress in their layers, the relative angle of the focal plane arrays (i.e. the vacuum cell assembly) had to be adjusted so that the plane of the reflectors was perpendicular the incoming readout illumination (Figure 63). The angle α depicted in Figure 63 had to match 10.5º and 3.8º measured for deformation-magnification and self-leveling structures, respectively, as discussed in Section 8.3. Such an adaptability to compensate for intrinsic stresses is an important advantage of optical readout compared to other readouts for micromechanical uncooled detectors, such as capacitive readout. The possibility of compensating for some levels of initial stress in SiO_2 detectors is one of the main characteristics of this readout that has allowed use of SiO_2 as a structural material possible.

Imaging and individual-detector characterization have been performed for both deformation-magnification and self-leveling structures and will be discussed in the following two sections of this chapter. Two types of detector characterization have been performed. The first type is simultaneous aggregate characterization of multiple detectors and providing the histogram distribution of their parameters. The second type focuses on a single detector observed through the readout and such investigation should provide the most accurate noise and detectivity information since it incorporates all of the

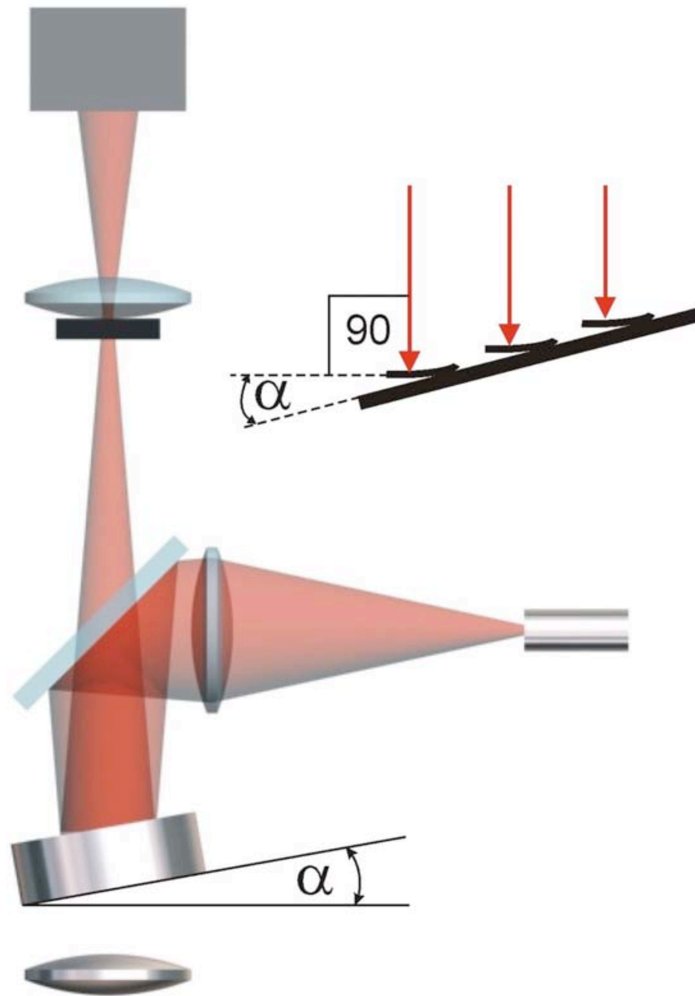

Figure 63 Illustration of FPA angle adjustment
Relative position of the FPA needed to be adjustable to allow for compensation of intrinsic stress. This capability was one of the advantages of optical readout that allowed for use of SiO_2 detectors experiencing levels of intrinsic stress.

noise sources such as mechanical vibrations of the setup as well as readout-related noise from fluctuations in readout light intensity, dark current in CCD pixels or noise coming from digitalization of charge in CCD pixels.

9.1 Imaging Using Arrays of Deformation-Magnification Structures

Imaging has been performed using the background subtraction method described in Chapter 6. No further image processing algorithms have been utilized. The thermal images obtained are shown in Figure 64. Figure 64a shows the image of a human hand and Figure 64b shows the image of a human face with sun-glasses on. As expected, since glasses are made out of plastic and they are opaque for infrared radiation and at a lower temperature then the human body, they appear darker in the image.

Several conclusions can be drawn from the images. Bright spots (active detectors) are further apart then in images shown in Chapter 6. This is because the inter-detector spacing in the array needed to be such that it would leave room for the frame that holds the chip together once the substrate was removed underneath each detector. In addition, the size of this array was only 120 × 120, compared to 256 × 256 of SiN_x detectors. This is because the detector size, designed having in mind potential capability for THz radiation, allowed much lower resolution. Approximately 16 SiN_x detectors, discussed in Chapter 6, have been replaced by a single substrate-free detector. Also, some bright spots in Figures 64a and 64b, closer to the middle of the array, are of irregular shape. This is due to non-uniformities of some detectors in the array manifesting in different angles of initial deformation. One possible reason for non-uniformities is that etching of the holes and releasing of the detectors in the middle of the wafer (corresponding to the corner of the arrays) was not fully completed due to the disappearance of the back-side window mask. Had the time allowed, several hundred extra nanometers on top of 2.2 μm back-side mask would have improved the final microfabrication step of deep reactive ion etching the holes underneath detectors and would result in much more uniformity among detectors in the array.

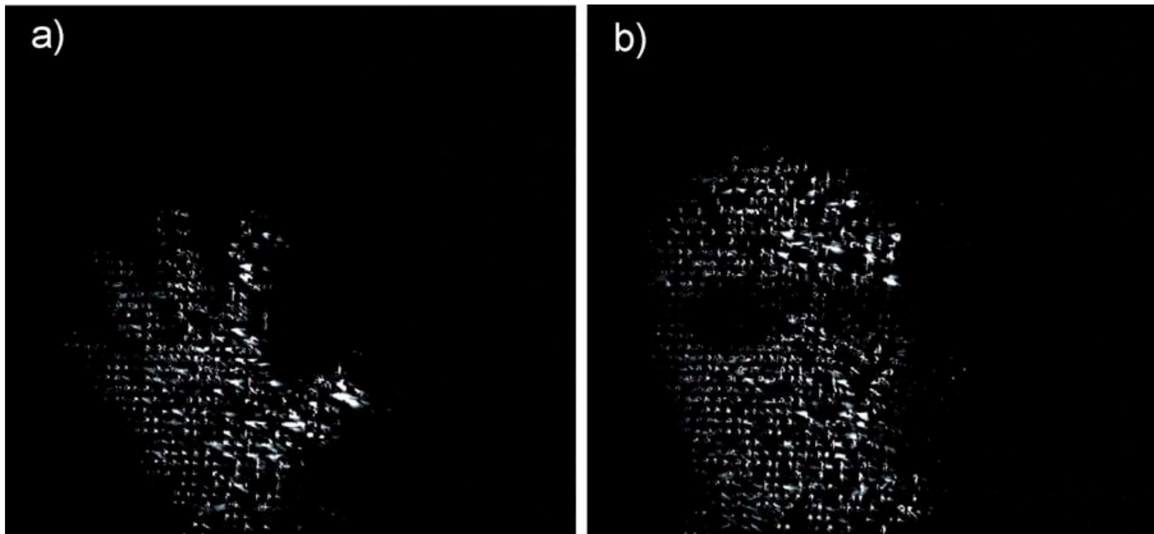

Figure 64 Thermal images of human hand and head with sun-glasses obtained using array of SiO_2 deformation-magnification detectors

However, despite some obvious flaws such as non-uniformity and decreased resolution, these detectors showed some advantages over the ones, without optical cavity, described in Chapter 6. One of the immediate indicators of improved sensitivity is that the gain used to multiply the results of background subtraction before imaging was 3×, compared to the gain of 30× required for SiN_x detectors. Furthermore, there were enough of active and responsive detectors in the array to perform imaging as well as aggregate analysis of their essential parameters such as *NEP*, *NETD* and *D**. The measurements have been performed using the heater shown in Figure 65a. It consists of a metal cube with a hole where a 140 Ω resistor has been passed and connected to a power supply.

The first parameter to measure was the *NETD,* which is the most widely used as well as the most straight-forward to obtain as it deals with target object temperatures and easily measured output parameters. Other important parameters such as *NEP* and *D** are detector-specific as they are a function of detector temperature. As such, they are extractable from the *NETD* by using the transfer function, *H* (Equation 21). In addition, the *NETD* is the only parameter defined for the system as a whole. The expression based on Equation 9 has been used, with gray-level intensity as output parameter.

$$NETD = \frac{i_N}{\Delta i_S}(T_T - T_B) \qquad (87)$$

where i_N is the level of output noise, Δi_S is the difference in output levels when camera is pointed into the target object and output levels when the camera is pointed to object whose temperature is in equilibrium with the background, T_T is the temperature of the target object and T_B is the background (environment) temperature, usually the room temperature. Since a 12-bit camera was used the possible levels of output were from 0 to 2^{12}. A thermometer probe was connected close to the surface of the hole facing the IR camera. The current of 50 mA to 300 mA was used to control the temperature of the heating element. It was initially located on the imaging screen, using the software, and positioned so that it covers as many of the uniform detectors as possible (Figure 65b). Once the focus was adjusted, the image of the whole illuminated array was recorded without background subtraction. This image was essentially a two-dimensional array of absolute intensities of individual CCD pixels, *target intensity array, TIA*. After that, the room-temperature shield was placed in front of the heating element and another image was recorded. This array of absolute intensities was a *background intensi*ty *array, BIA*. Finally a sequence of images was recorded as subsequent frames with the camera pointing into the heater. These images were used to obtain the noise data. The fluctuations in individual pixel intensities were incorporating all noise sources, including the detector-specific vibrations, vibrations transferred through the pumping line as well as the noise coming from the readout light source and CCD. Standard deviation for each of the pixels was obtained and stored in the *noise array*. To obtain the aggregate information about the *NETD* in the form of histogram, Equation 87 has been performed on each of the elements of above-mentioned array. However, as can be seen in Figures 64 and 65b, there are some dark areas surrounding each of the active pixels, corresponding to the frame around each detector as well as to the unreleased areas of the array. Those areas needed to be removed from consideration as the difference in recorded intensities of CCD pixels in those areas when imaging the heater and the shield

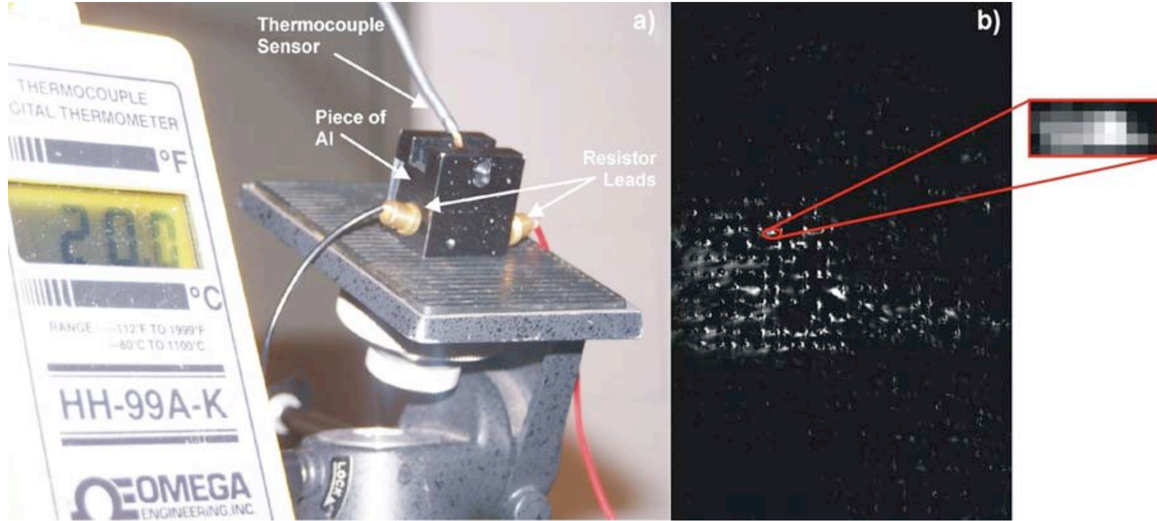

Figure 65 Illustration of resistive heater used for parameter-measurements
a) shows the photograph of the heater mounted on a tripod; b) shows the thermal image of the same heater with zoomed-in segment focusing isolating a single detector for characterizing its parameters

would be equal to 0 yielding infinite *NETD*. An element-by-element subtraction has been performed so that the *background intensity array* has been subtracted from *target intensity array,* resulting in an array of intensities Δi_S.

$$\Delta i_{S-i,j} = TIA_{i,j} - BIA_{i,j} \tag{88}$$

Elements with 0 values have been excluded from further calculations. Subsequently, for each position with a nonzero intensity difference, an element of the *noise array* has been divided by a corresponding element in the Δi_S array. The newly formed array has then been multiplied by the difference between the temperature of the heater and temperature of the background and the results were plotted in the form of histogram. The process has been repeated for several different temperatures between 30 ºC and 50 ºC. The histograms for 35 ºC and 50 ºC are shown in Figure 66.

The majority of detectors exhibit similar *NETD* value, around 200mK, for all temperatures. Comparing these to the histograms in Figure 32, the improvement in terms of noise is observed. This is not unexpected as the combination of materials promises higher sensitivity. Furthermore, increasing the detector area, A_d, alone should decrease the *NETD* (Equation 25). It is evident that these values are much larger then the values modeled and experimentally obtained for detector-specific noise sources which were of the order of few mK. This indicates that most of the additional noise comes from the readout and that there is a lot of room for improvement in the readout configuration.

However, encouraging *NETD* values should not be considered without considering values of normalized detectivity *D** which takes into account the detector area and might be useful for comparing these detectors to other infrared detectors of different sizes. Since *D** is another detector-specific parameter but depends on a readout configuration,

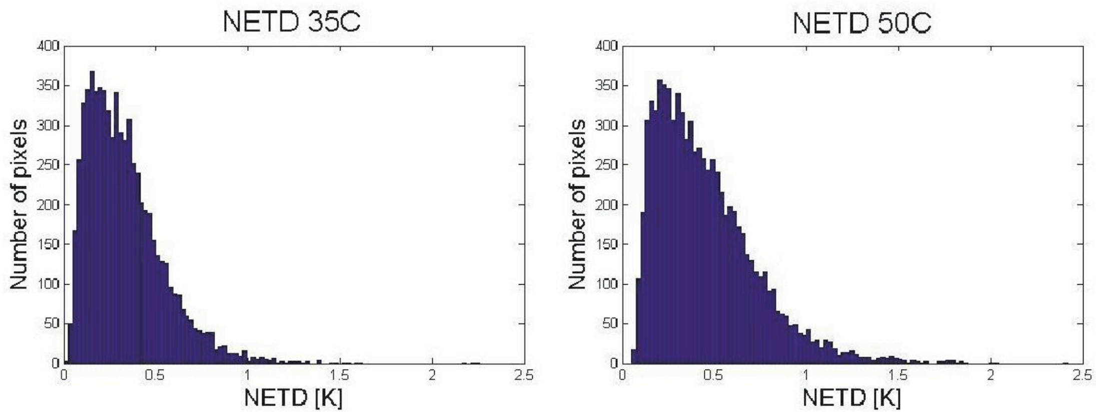

Figure 66 NETD histograms for the array of SiO_2 deformation-magnification detectors measured at two different temperatures.
The figures indicate majority of detectors exhibiting NETDs of about 200 mK.

individual detectors employed in the complete readout system needed to be evaluated. To achieve this, we needed to focus on a single detector by selecting one of the active areas of the output (Figure 65b), which would correspond to a single detector. Based on the concept of our readout, the brightness of this spot was changing with changes in temperature of the target. To capture the whole active area (reflector), we needed to use more then one CCD pixel. More specifically, the area of interest was 12 × 5 pixels. The average value of brightness intensity of those pixels was monitored as the temperature was varied. Similarly for the aggregate measurements, for each temperature, sets of images were recorded with a) camera pointed into the heater, b) camera pointed into a room-temperature shield and c) camera lens cover on for recording the noise. Simple averaging operation was performed on the first two sets of images and their difference yielded the $\Delta i'_S$ for that individual detector. The third set was used to first obtain the standard deviation of values of each pixel and then to average those values to obtain the average fluctuations of brightness intensity, corresponding to cumulative effect of all noise sources. The plot of differences of intensities versus temperature is shown in Figure 67. It can be seen from the plot that due to high sensitivity, the detector deformation reaches a saturation point at about 40 ºC. This is a result of the detector reaching its maximum deflection angle detectable by the readout configuration.
Using the noise information, the *NETD* values for each of the temperatures could be obtained using Equation 87, where the averages obtained for signal intensity difference and noise were used. The most relevant parameters should be those from the linear part of detector operation, i.e. temperatures between 25 ºC and 40 ºC. The average value of *NETD* was 114 mK. This is slightly lower then the value that most of the CCD pixels have in the histograms in Figure 66. The reason for the discrepancy is that histograms contain all of responsive areas including bimaterial regions on the side of the main reflectors whose size and reflective areas are considerable due to large overall detector size. These regions do not have the total deformation angle as high as the reflector for the same temperature difference (Δi_S in Equation 87) and therefore exhibit higher *NETD*.

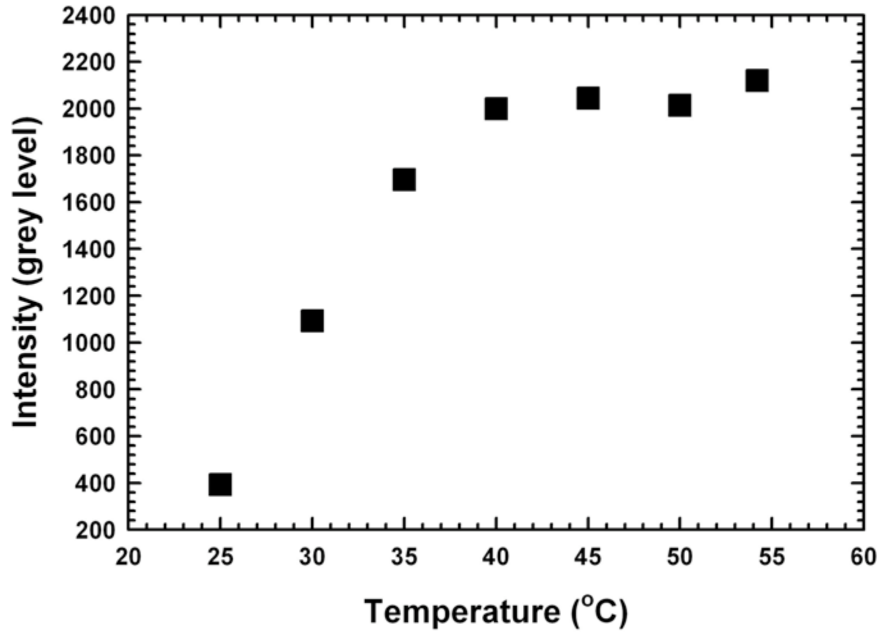

Figure 67 Average light intensity versus temperature for CCD pixels corresponding to a single SiO_2 deformation-magnification detector
Differences in light intensities when system was exposed to the target at different temperatures and when it was exposed to the background at room temperature show that the optimal region of operation is for target temperatures below 40 ºC. This saturation is due to very high detector sensitivity.

Obtained *NETD* value can now be used to estimate the *NEP* and *D** of individual detectors. However, since these parameters involve the temperature of detector rather then that of the target-object, it is necessary to calculate the transfer function *H*, provided by Equation 21. Using the values from previous chapter for absorption coefficient of the detector $\eta = 0.7$, transmission coefficient of the optics $\tau_0 = 0.5$, area of the detector $A_d = 1.76 \times 10^{-8}$ m^2, f-number of the optics $F = 1$, thermal conductance $G = 1.8 \times 10^{-7}$ W/K and $(dP/dT)_{\lambda1-\lambda2} = 2.62$ W/m^{2}K, the value of transfer function is obtained to be $H = 0.022$. In other words, for 1K of temperature increase of the target object, the detector temperature will increase by 22 mK. The expression for evaluating *NEP* and *D** have been derived in the following way. Using Equation 5 and 6, we obtain:

$$NEP = \frac{\theta_N}{\Delta\theta_s} P_0 \tag{89}$$

Then, using steady-state version of Equation 14 with Equation 89, we further obtain:

$$NEP = \frac{\theta_N}{\Delta\theta_s} \frac{G\Delta T_D}{\eta} \tag{90}$$

Finally, using the Equation 21 which states that $\Delta T_D = H\Delta T_T$, we obtain the final relation between *NEP* and measured *NETD*:

$$NEP = \frac{\theta_N}{\Delta\theta_s} \frac{GH}{\eta} \Delta T_T = NETD \frac{GH}{\eta} \tag{91}$$

Using the values for thermal conductance, G, transfer function, H, and absorption coefficient, η, used above, provides the average noise equivalent power NEP of 6.58×10^{-10} W for the temperature span where detector response is linear i.e. linear part of the plot in Figure 67.

Finally, average normalized detectivity D^* was easily obtained from noise equivalent power NEP using Equation 7 together with the area of the detector and bandwith $B = 30$ Hz. The value obtained was $D^* = 1.1 \times 10^8$ cm Hz$^{1/2}$ W^{-1} which is comparable to current uncooled infrared detectors such as bolometers [100].

Since the individual characterization of these detectors performed in previous chapter showed them to have improved parameters compared to the ones published for similar SiN_x detectors by Dong et al [89], which were already capable of imaging without placing the detectors at low operating pressure, we decided to test our arrays in those conditions. Imaging the soldering iron with detectors at atmospheric pressure was performed and the obtained image is shown in Figure 68. In addition, human hand similar to those shown in Figure 64 was imaged, but we were not able to record quality still images due to non-responsive areas of the array. Recording videos of head and hand is, however, possible since human brain is capable of interpreting the non-responsive areas as "stains" on a viewing window. Videos of the soldering iron and head and hand recorded with detectors at atmospheric pressures, along with the video recorded with detectors operating at 5 mTorr, are available on the DVD ROM, titled "Dissertation Multimedia Supplement", stored in the University of Tennessee Library Archives and can be accessed under author's name and dissertation title.

Figure 68 Thermal image of a soldering iron recorded with SiO_2 deformation-magnification FPA at atmospheric pressure

The removal of the substrate underneath each detector which removed the closest path for convective heat dissipation, allowed for acceptable thermal isolation of the detector even at atmospheric pressures. This, along with the improved sensitivity allowed obtaining images of both hot and body-temperature objects while detectors were in atmospheric pressure environment.

9.2 Imaging Using Arrays of Self-Leveling Structures

Imaging has been performed using the background subtraction method described in Chapter 6. No further image processing algorithms have been utilized. The thermal images obtained are shown in Figure 69. Figure 69a shows the image of a human hand and Figure 69b shows the image of a human face with sun-glasses on. As expected, since glasses are made out of plastic and they are opaque for infrared radiation and at a lower temperature then the human body, they appear darker in the image.

Bright spots (active detectors) were even further apart then in images obtained using deformation magnification structures. This is because the array spacing was designed to be larger on most of the arrays to ensure that the arrays would survive the deep reactive ion etching. Spacing was decreased on one of the arrays and those were the arrays that were discussed earlier in this chapter. The size of this array was only 100 × 100. This is because the detector size, designed having in mind potential capability for THz radiation, allowed much lower resolution. As in the case of deformation-magnification structures, non-uniformity among detectors initial deformation caused some bright spots in Figures 69a and 9b, closer to the edge of the array to be of irregular shape. Notably, there was more active detectors possible to be used simultaneously since the self-leveling design results in much smaller initial deformation of the reflector and the range of deflections was smaller as a result. As in the previous case, several hundred extra nanometers on top of 2.2 μm back-side mask would have improved the final microfabrication step of deep reactive ion etching the holes underneath detectors and would result in higher array uniformity.

These detectors, too, showed significantly higher sensitivity over the ones described in Chapter 6. One of the immediate indicators of improved sensitivity is that the gain used to multiply the results of background subtraction, before using those values to reconstruct the image, was 4×, compared to the gain of 30× required for SiN_x detectors. As in the previous case, there were enough of active and responsive detectors in the array to perform imaging as well as aggregate analysis of their essential parameters such as *NEP*, *NETD* and *D**. The measurements have been performed using the heater shown in Figure 65a.

The first parameter to be measured was again *NETD*, and multiple detectors have been probed using the procedure explained in Section 10.1 and Equation 87 applied to each of the elements of the arrays corresponding to intensities from CCD pixels recorded with imaging system pointing into the heating element, into the room-temperature shield and as well as mean noise levels of each pixel. Measurements were performed at several different temperatures and two representative histograms taken at 35 ºC and 50.2 ºC are shown in Figure 70.

These histograms show that the majority of detectors have *NETD* of about 200 mK. As expected, the total *NETD* does not differ significantly from that of imaging system implemented with deformation-magnification structures since most of the noise originates from the integrated configuration setup as discussed in the previous section, and the less then 1 mK of difference in detector specific *NETD*, calculated in Chapter 8, was not expected to be observed at this level.

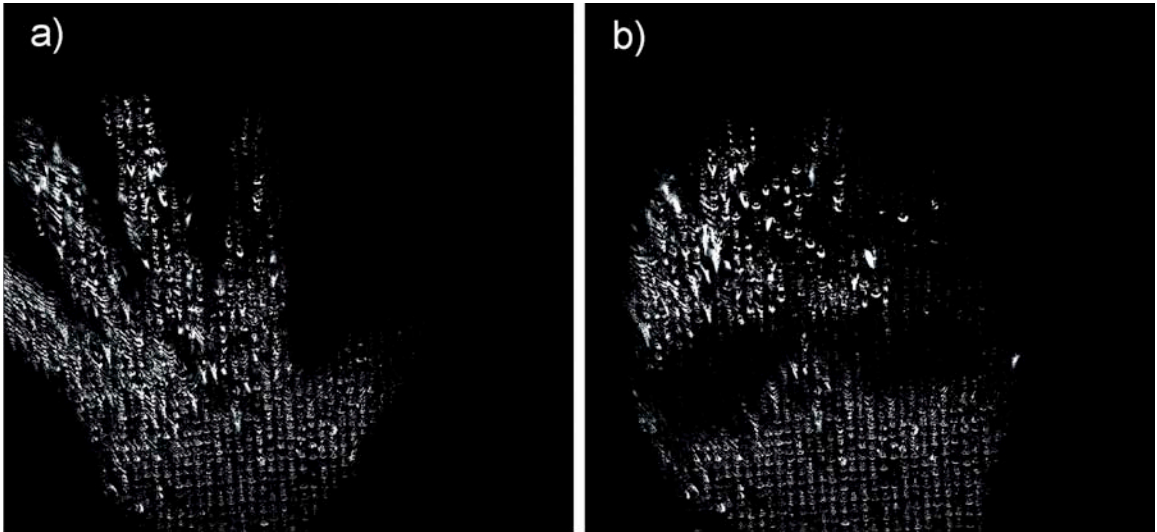

Figure 69 Thermal images of human hand and head with sun-glasses obtained using array of SiO_2 deformation-magnification detectors

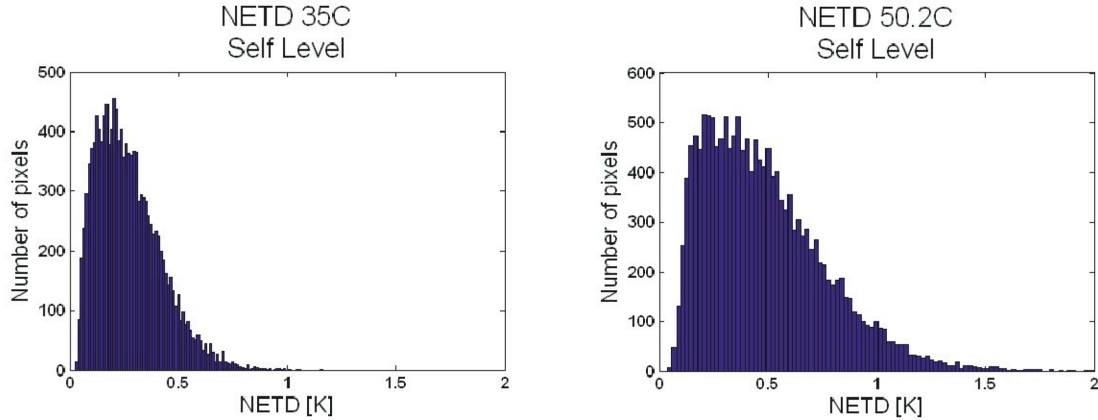

Figure 70 NETD histograms for the array of SiO_2 self-leveling detectors measured at two different temperatures

The figures indicate majority of detectors exhibiting NETDs of about 200 mK.

Following the sequence from previous section, normalized detectivity *D** needed to be measured in order to be able to compare these with other conventional detectors of different sizes. In order to obtain *D**, noise equivalent power *NEP* needed to be obtained first. Focus was, again, on one of the detectors observed through the readout. This was achieved by isolating the reflection of a single detector for which a 6 × 4 region we needed to be selected. Two sets of images were recorded again, at several different temperatures, in order to obtain the average light-reflection intensity from a particular detector when imaging system was pointed into the heater element, average light-reflection intensity with a room-temperature shield in front of the imaging system and average fluctuation levels in the selected CCD pixels with the camera pointed into the heater. The values of intensity difference were plotted and are shown in Figure 71.

Compared to the plot of grey-level intensity obtained for deformation-magnification structures, these detectors can evidently provide higher dynamic range since the intensity increase is almost linear to 50 degrees and then it starts saturating at a slower rate then for deformation magnification detectors.

Using the noise information, the *NETD* values for each of the temperatures could be obtained using Equation 87, where the averages obtained for signal intensity difference and noise were used. The most relevant parameters should be those from the linear part of the plot, i.e. temperatures between 35 ºC and 45 ºC. The average value of *NETD* was 173 mK, which is slightly higher then the average for linear part of the response of deformation-magnification detectors. This can be explained by the fact that signal-to-noise ratio is worse for these detectors once employed in the imaging system as the noise levels are almost the same since they come mostly from the integrated configuration and not the detector itself, while the sensitivity in the linear part is lower as expected and as testified by comparing the slopes of plots in Figures 67 and 71 as well as by the modeled results discussed in previous chapter. This value, however, is still slightly lower then the value that most of the CCD pixels have in the histograms in Figure 70, but the reason for it is that histograms contain all responsive areas including bimaterial regions on the side of the main reflectors whose size and reflective areas are considerable due to large overall detector size. These regions do not have the total deformation angle as high as the

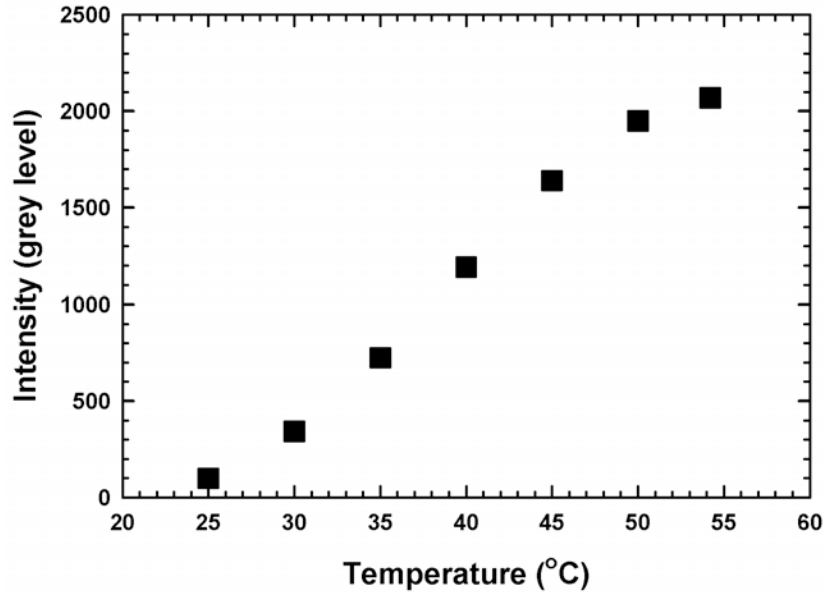

Figure 71 Average light intensity versus temperature for CCD pixels corresponding to a single SiO_2 self-leveling detector

Differences in light intensities when system was exposed to the target at different temperatures and when it was exposed to the background at room temperature show that slightly lower sensitivity of these detectors allows for a higher dynamic range of temperatures then for deformation-magnification detectors.

reflector for the same temperature difference (Δi_S in Equation 87) and therefore exhibit higher *NETD*.

Obtained *NETD* value can now be used to estimate the *NEP* and *D** of individual detectors. However, since these parameters deal with the temperature of detector rather then that of the target object, the va;ie transfer function *H* is required, provided by Equation 21. Using the values from previous chapter for absorption coefficient of the detector $\eta = 0.7$, transmission coefficient of the optics $\tau_0 = 0.5$, area of the detector $A_d = 1.76 \times 10^{-8}$ m^2, f-number of the optics $F = 1$, thermal conductance $G = 2.3 \times 10^{-7}$ W/K and $(dP/dT)_{\lambda 1-\lambda 2} = 2.62$ W/m^{2}K, the value of transfer function is obtained $H = 0.018$. In other words, for 1K of temperature increase of the target object, the detector temperature will increase by 18 mK.

Using the values for thermal conductance, transfer function and absorption coefficient used above together with Equation 91, we obtain the average noise equivalent power *NEP* of 1.09×10^{-9} W for the temperature span where detector response is linear i.e. linear part of the plot in Figure 71.

Finally, average normalized detectivity *D** was easily obtained from noise equivalent power *NEP* using Equation 7 together with the area of the detector and bandwith $B = 30$ Hz. The value obtained was $D^* = 0.76 \times 10^8$ cm Hz$^{1/2}$ W^{-1}. Both *NEP* and *D** are not as good as those of deformation magnification detectors, and it is due to the fact that the

noise levels have not changed much while sensitivity has decreased. However, these values are still comparable to current uncooled infrared detectors such as bolometers.

Since the measurements of parameters of these detectors, performed in previous chapter, showed that they too have improved parameters compared to the ones published for similar SiN_x detectors by Dong et al [89], which were already capable of imaging without placing the detectors at low operating pressure, we decided to test our arrays in those conditions. Imaging the soldering iron has been performed and the obtained image is shown in Figure 72. Videos of the soldering iron with detectors at atmospheric pressure, along with the video of head and hand recorded with detectors operating at 5 mTorr, are available on the DVD ROM, titled "Dissertation Multimedia Supplement", stored in the University of Tennessee Library Archives and can be accessed under author's name and dissertation title.

Due to a better uniformity of these detectors compared to the array of deformation-magnification detectors shown in previous section, the image of a soldering iron has a better clarity in this case.

9.3 Summary

Results from this and Chapter 8 have been compared in Table 9. Chapter 8 focused on measuring the intrinsic properties of detector while Chapter 9 observed those parameters through the integrated system and accounted for the noise introduced by the integrated configuration.

Table 9 Comparisson of experimentally evaluated parameters for detector alone and detector in the integrated system

	$NEP_{detector}$ (pW)	$NEP_{readout}$ (pW)	$D^*_{detector}$ (Jones)	$D^*_{readout}$ (Jones)	$NETD_{detector}$ (mK)	$NETD_{readout}$ (mK)
DMS	17.9	658	4.07×10^9	1.1×10^8	2.97	114
SLS	11.7	1090	6.20×10^9	0.76×10^8	2.14	173

DMS – Deformation-Magnification Structure
SLS – Self-Leveling Structure

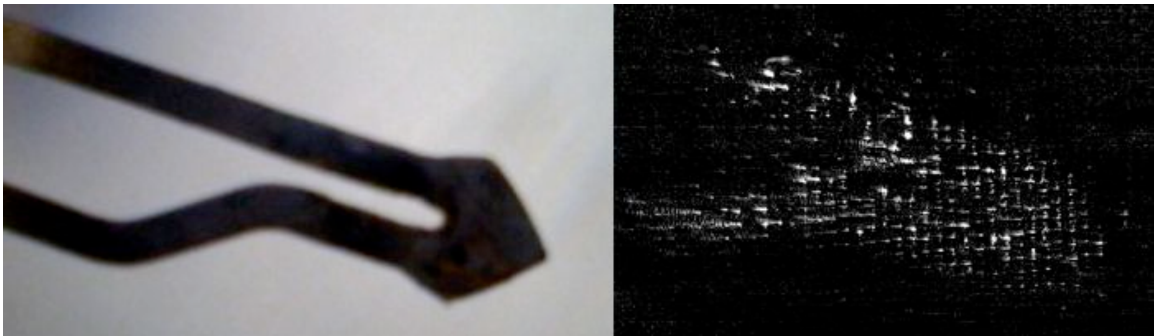

Figure 72 Thermal image of a soldering iron taken with deformation-magnification FPA at atmospheric pressure

The removal of the substrate underneath each detector which removed the closest path for convective heat dissipation, allowed for acceptable thermal isolation of the detector even at atmospheric pressures. This, along with the sensitivity improved by the optical resonant cavity allowed obtaining images of hot and objects while detectors were in atmospheric pressure environment. The photograph of the soldering iron is shown for reference

Chapter 10

Conclusion

In this dissertation, the viability of optically-probed uncooled micromechanical infrared detectors has been investigated. Parameters for comparison with the contemporary uncooled infrared detectors needed to be defined.

We have first built an array of simplified micromechanical uncooled infrared detectors and integrated it into the imaging system. The simplifications were possible since the absorption of infrared radiation from room-temperature objects for SiN_x which we have chosen for this step is sufficient enough that combined with the optical cavity between the detector and the substrate, we eliminated the need for building a complex air gap into the absorber. This has simplified the microfabrication process compared to the work by Ishizuya [30] by removing a few lithographic steps. Based on the parameters defined, performance comparable to contemporary uncooled infrared detectors, such as measured noise equivalent temperature difference (*NETD*) of 500 mK, has been achieved.

We have then demonstrated the possibility for significant further improvement of the detector thermomechanical properties by combining the concepts of both substrate removal beneath each detector and choice of materials with highly dissimilar coefficients of thermal expansion (SiO_2 and Al). Microfabrication of structures made of single-layer SiO_2 has not been attempted prior to this work. This new approach further simplified the microfabrication process by not requiring the etching of the anchoring posts, sacrificial layer deposition and chemomechanical polishing. The disadvantage of SiO_2 over SiN_x in terms of lower absorption of infrared photons in the region of interest has been addressed by incorporating a optical resonant cavity in the form of an additional layer of amorphous Si within the detector's absorber. Building an optical resonant cavity as of a layer of solid material within the absorber has not been attempted previously either. Previous absorption improvements using optical cavities were based on an air-gap cavity either integrated into the absorber or between the absorber and the substrate. The cavity has increased the absorption from 40% to 60% for some of the wavelengths (Figure 48). With better control of the deposition conditions (i.e. film thickness), the cavity thickness

can be more readily optimized and further improvements in absorption and detector sensitivity are possible as can be shown in the curve representing the reflectance for 750 nm optical cavity. All of these improvements have been demonstrated to improve the parameters such as noise equivalent temperature difference (*NETD*) compared to the currently used micromechanical uncooled infrared detectors (Table 3), while achieving the normalized detectivity (*D**) values comparable to other uncooled infrared detectors (such as bolometers) [100]. The measured *NETD* of about 120 mK has been achieved with the normalized detectivity of the order of 10^9 Jones.

Issues, such as stress, are present and need to be addressed, but this dissertation shows that it is possible to compensate for stress by modifications to the integrated configuration. One of the proposed modifications consists of adjusting the relative angle between the probing light and the normal of the plane of the array. This dissertation has also demonstrated that structural layer and metallization thin film deposition conditions influence the level of intrinsic stress and future work could focus on finding optimal conditions for minimizing the stress. In addition, future work can focus on obtaining the systematic data on dependence of film stress on deposition parameters and then utilizing the Stoney equation [101] to match the stresses of the two layers in order to reduce overall initial deformation of the detectors. One example of stress-control is by using annealing techniques, which control the concentration of hydrogen in PECVD oxides. Work by Elliman et al. has shown that type and magnitude of stress in PECVD films depends on hydrogen concentration. One of the near-term possibilities is to use two types of metal deposition for depositing parts of either layers (or even both). This would involve depositing one part of the layer using e-beam evaporation and remaining part using the sputtering. These deposition methods have shown to result in opposite types of stress (e-beam evaporation results in tensile stress while sputtering deposition results in compressive stress). Therefore, finding the optimal ratio of metallization thicknesses deposited using these two methods may also lead to less stressed metal thin film.

This dissertation has also shown that most of the noise in this type of device originates from the integrated configuration. Improvements to this configuration might be achieved by securing the components more rigidly. Noise coming from vibrations of the optical components will be inherently resolved if such a system is to be implemented in a packaged camera case where most of the optical components as well as the readout light source and cell for the focal plane arrays would be mounted into a rigid, solid-piece molding assembly.

Until then, it will not be possible to decrease overall noise by utilizing the advantage of low-noise self-leveling detectors over deformation-magnification detectors. However, the self-leveling design also reduces the level of initial deformation of the readout reflectors (3.8º vs. 10.5º) as seen in Chapter 8, making them more suitable for utilizing in the optical-readout configuration discussed in this dissertation. Furthermore, higher temperature range can be imaged using self-leveling detector arrays as the effect of saturation is minimized in that configuration.

Another issue inherent to the substrate-free arrays is the requirement of the substrate frame around every detector in order to allow creation of the through-substrate channel beneath each detector. This frame results in the dark area around each bright spot in the image visible in thermal images displayed in Figures 64, 65, 68, 69 and 72. This issue,

however, can be addressed with image-processing techniques that would also help with non-responsive areas of the arrays that appear as dark spots in the image. Image-processing techniques include spatial Fourier transforms that are very successful in removing the regular patterns such as the one that would be present on a uniform substrate-free array, as well as morphological component analysis (MCA) inpainting method already investigated by our group [102] that is successful with minimizing the effect of non-uniformities and non-responsive areas.

The advantage of this optically-probed, substrate-free micromechanical uncooled infrared detectors over currently used bolometric infrared detectors lies in microfabrication simplicity, easy scalability, and reliability. Absence of electrical connection between individual detectors and the substrate simplifies the microfabrication process while improving the yield and reducing the cost. In addition, this approach improves the thermal isolation and therefore improves the sensitivity. Large reduction in cost can bring infrared imaging to a much larger range of applications than is currently the case. It is also conceivable that, with further development, these detectors would be capable of achieving acceptable sensitivities and low levels of noise for imaging room-temperature objects under atmospheric conditions. This has been enabled by removing the substrate underneath the detector, which has increased the length of the shortest pathway between the detector and the substrate. This pathway has previously been the one for substantial heat dissipation by convection. Decreasing the thermal conductance both through the legs and through convection, allows operation at higher pressures including the atmospheric. Operation at atmospheric pressures would further simplify the system-integration and manufacturing and decrease the cost of the imaging systems along with improving their reliability and robustness.

The higher sensitivity provided by the high thermal expansion coefficient mismatch in the arrays analyzed in this dissertation could open the potential for direct-view cameras. Direct-view is the term used for arrays with sensitive enough detectors that do not require the background subtraction. This would remove the need for a microprocessing and, as the name implies, enable viewing directly by the unaided human eye.

Another advantage of detectors described in this dissertation is that their size makes them applicable for THz detection. In the future, as development of THz sources matures, it would be more practical to explore additional THz imaging applications. This is an emerging field, especially in the field of safety and security. Further improvements could be achieved by choosing the material and thickness for the optical cavity layer that would be specifically tuned for photons - in the THz wavelength-range.

All the results presented are encouraging and describe the large potential of micromechanical uncooled infrared/THz detectors for future imaging devices. Further improvements will make these detectors a viable alternative to more complex and more expensive bolometer-based uncooled infrared detectors.

Bibliography

Bibliography

1. Planck, M., *On the law of distribution of energy in the normal spectrum.* Annalen der Physik, 1901. **4**: p. 553.
2. Datskos, P.G., et al., Ultramicroscopy, 2001. **86**: p. 191.
3. Mao, M., et al. in *Microelectromechanical Systems, Proceedings of the American Society of Mechanical Engineers*. 1999.
4. Balcerak, R.S. *Uncooled IR imaging: technology for the next generation*. in *Infrared Technology and Applications XXV*. 1999: Proceedings of the SPIE.
5. Kayes, R.J., *Optical and Infrared Detectors*. 1977, Berlin: Springer-Verlag.
6. Miller, J.L., *Principles of Infrared Technology*. 1994, New York: Van Nostrand Reinhold.
7. Rogalski, A., *New trends in infrared detector technology.* Infrared Physics & Technology 1994. **35**: p. 1.
8. Hanson, C.M. *Uncooled thermal imaging at Texas Instruments*. in *Infrared Technology XIX*. 1993: Proceedings of the SPIE.
9. Butler, N.R., et al. *Low-cost uncooled microbolometer imaging system for dual use*. in *Infrared Technology XXI*. 1995: Proceedings of SPIE.
10. Kruse, P.W., *A comparison of the limits to the performance of thermal and photon detector imaging arrays.* Infrared Physics & Technology, 1995. **36**(5): p. 869-882.
11. Kruse, P.W., *Uncooled Infrared Imaging Arrays and Systems*. Semiconductors and Semimetals, ed. P.W. Kruse and D.D. Skatrud. Vol. 47. 1997, San Diego: Academic Press.
12. Wood, R.A. *Uncooled thermal imaging with monolithic silicon focal planes*. in *Infrared Technology XIX*. 1993: Proceedings of SPIE.
13. Wood, R.A. and N.A. Foss, Laser Focus World, 1993. **101**.
14. Datskos, P.G., N.V. Lavrik, and S. Rajic, *Performance of uncooled microcantilever thermal detectors.* Review of Scientific Instruments, 2004. **75**(4): p. 1134-1148.
15. Grbovic, D., et al., *Uncooled infrared imaging using bimaterial microcantilever arrays.* Applied Physics Letters, 2006. **89**(7).
16. Lavrik, N.V., et al. *Uncooled infrared imaging using bimaterial microcantilever arrays*. in *Infrared Technology and Applications XXXII*. 2006: Proceedings of the SPIE.

17. Amantea, R., et al. *Progress toward an uncooled IR imager with 5-mK NETD*. in *Infrared Technology and Applications XXIV*. 1998: Proceedings of the SPIE.
18. Amantea, R., et al. *Uncooled IR imager with 5-mK NETD*. in *Infrared Technology and Applications XXIII*. 1997: Proceedings of the SPIE.
19. Datskos, P.G., et al., *Remote infrared radiation detection using piezoresistive microcantilevers.* Applied Physics Letters, 1996. **69**: p. 2986.
20. Datskos, P.G., S. Rajic, and I. Datskou, *Photoinduced and thermal stress in silicon microcantilevers.* Applied Physics Letters, 1998. **73**: p. 2319.
21. Lai, J., et al., Sensors and Actuators, 1997. **58**: p. 113.
22. Oden, P.I., et al., *Uncooled thermal imaging using a piezoresistive microcantilever.* Applied Physics Letters, 1996. **69**: p. 3277–3279.
23. Perazzo, T., et al., *Infrared vision using uncooled micro-optomechanical camera.* Appl. Phys. Lett, 1999. **74**: p. 3567.
24. Senesac, L.R., et al., *IR imaging using uncooled microcantilever detectors.* Ultramicroscopy, 2003. **97**: p. 451.
25. Wachter, E.A., et al., *Remote optical detection using microcantilevers.* Review of Scienific Instruments, 1996. **67**: p. 3434.
26. Salerno, J.P., *High frame rate imaging using uncooled optical readout photomechanical IR sensor.* Proceedings of SPIE, 2007. **6542**: p. 65421D.
27. Kruse, P.W. *Uncooled IR focal plane arrays*. in *Infrared Technology XXI*. 1995: Proceedings of the SPIE.
28. Howard, P.E., et al. in *Infrared Technology and Applications XXVI, Proceedings of the SPIE*. 2000.
29. Murphy, D.F., et al. *High-sensitivity 25-μm microbolometer FPAs*. in *Infrared Detectors and Focal Plane Arrays VII, Proceedings of the SPIE*. 2000.
30. Ishizuya, T., et al. *160× 120 pixels optically readable bimaterial infrared detector*. in *The Fifteenth IEEE International Conference on Micro Electro Mechanical Systems*. 2002.
31. Zhao, Y., et al., *Optomechanical uncooled infrared imaging system: design, microfabrication, and performance.* Microelectromechanical Systems, Journal of, 2002. **11**(2): p. 136-146.
32. Federici, J.F., et al., *THz imaging and sensing for security applications-explosives, weapons and drugs.* Semicond. Sci. Technol, 2005. **20**(7): p. S266-S280.
33. Hu, B.B. and M.C. Nuss, *Imaging with terahertz waves.* Opt. Lett, 1995. **20**(16): p. 1716–1718.
34. Miller, A.J., A. Luukanen, and E.N. Grossman, *Micromachined antenna-coupled uncooled microbolometers for terahertz imaging arrays.* Proceedings of SPIE, 2004. **5411**: p. 18-24.
35. Woolard, D.L., et al., *Terahertz frequency sensing and imaging: a time of reckoning future applications?* Proceedings of the IEEE, 2005. **93**(10): p. 1722-1743.
36. Grbovic, D., et al., *Arrays of SiO2 Substrate-Free Micromechanical Uncooled Infrared and THz Detectors.* Accepted for publication in Journal of Applied Physics, 2007.

37. Cumming, D.R.S. and T.D. Drysdale, *A micro-mechanical beam-steering device for terahertz frequencies.* Optics Communications, 2006. **259**(1): p. 373-377.
38. Dragoman, D. and M. Dragoman, *Terahertz field characterization using Fabry–Perot-like cantilevers.* Applied Physics Letters, 2001. **79**: p. 581.
39. Dragoman, D. and M. Dragoman, *Terahertz fields and applications.* Progress in Quantum Electronics, 2004. **28**(1): p. 1-66.
40. Hartnagel, H.L. and M. Dragoman, *Modulation of quantum-electronic devices by bending of special MEMS structures.* Semiconductor Conference, 2004. CAS 2004 Proceedings. 2004 International, 2004. **1**.
41. Richards, P.L., *Bolometers for infrared and milimiter waves.* Journal of Applied Physics, 1994. **76**(1).
42. Vig, J.R., R.L. Filler, and Y. Kim, *Uncooled IR Imaging Array Based on Quartz Microresonators.* JOURNAL OF MICROELECTROMECHANICAL SYSTEMS, 1996. **5**(2): p. 131.
43. Kenny, T.W., et al., *Micromachined infrared sensors using tunneling displacement transducers.* Review of Scientific Instruments, 1996. **67**(1): p. 112-128.
44. Datskos, P.G. *Micromechanical uncooled photon detectors*. in *Photodetectors: Materials and Devices V,* . 2000: Proceedings of the SPIE.
45. Huang, S. and X. Zhang, *Application of polyimide sacrificial layers for the manufacturing of uncooled double-cantilever microbolometers.* Material Research Society Symposium Proceedings, 2006. **890**.
46. Hunter, S.R., et al., *High-sensitivity uncooled microcantilever infrared imaging arrays.* Reliability of Optical Fiber Components, Devices, Systems, and Networks III. Edited by Limberger, Hans G.; Matthewson, M. John. Proceedings of the SPIE, 2006.
47. Li, B., *Design and simulation of an uncooled double-cantilever microbolometer with the potential for~ mK NETD.* Sensors and Actuators A: Physical, 2004(2): p. 351-359.
48. Kenny, T.W., et al., *Electron tunnel sensors.* Journal of Vacuum Science and Technology A, 1992. **10**.
49. Sarid, D., *Scanning Force Microscopy*. 1991, New York: Oxford University Press.
50. Guo, Z., et al., *Performance analysis of microcantilever arrays for optical readout uncooled infrared imaging.* Sensors & Actuators: A. Physical, 2007. **137**(1): p. 13-19.
51. Ishizuya, T., et al., *160× 120 pixels optically readable bimaterial infrared detector.* The Fifteenth IEEE International Conference on Micro Electro Mechanical Systems, 2002: p. 578-581.
52. Lavrik, N.V., et al., *Uncooled infrared imaging using bimaterial microcantilever arrays.* Infrared Technology and Applications XXXII, 2006. **6206**: p. 62061K.
53. Shi, S., et al., *Design, simulation and validation of a novel uncooled infrared focal plane array.* Sensors and actuators. A, Physical, 2007. **133**(1): p. 64-71.
54. Datskos, P.G. and N.V. Lavrik, *Detectors—Figures of Merit.* Encyclopedia of Optical Engineering, 2003.

55. Dereniak, E.L. and G.D. Boreman, *Infrared Detectors and Systems*. 1996, New York: John Wiley and Sons.
56. Dereniak, E.L. and D.G. Crowe, *Optical Radiation Detectors*. 1984, New York: John Wiley and Sons.
57. Kruse, P.W., *Uncooled Thermal Imaging, Arrays Systems and Applications*. 2001, Bellingham, WA: SPIE Press.
58. Kruse, P.W., L.D. McGlauchlin, and R.B. McQuistan, *Elements of Infrared Technology*. 1962, New York: John Wiley and Sons. 351.
59. Williams, C.S. and O.A. Becklund, *Optics: A Short Course for Engineers and Scientists*. 1972, New York: Wiley-Interscience.
60. Holst, G.C., *Testing and Evaluation of Infrared Imaging Systems*. 1998, Belligha sm, WA: SPIE Press.
61. Vincent, J.D., *Fundamentals of Infrared Detector Operation and Testing*. 1989, New York: John Wiley and Sons.
62. Lloyd, J.M., *Thermal Imaging Systems*. 1975, New York: Plenum Press.
63. Gol'tsman, G.N., et al., *Picosecond superconducting single-photon optical detector.* Applied Physics Letters, 2001. **79**: p. 705.
64. Timoshenko, S., *Analysis of bi-metal thermostats.* Journal of the Optical Society of America, 1925. **11**(3): p. 233.
65. Shaver, P.J., *Bimetal Strip Hydrogen Gas Detectors.* Review of Scientific Instruments, 1969. **40**: p. 901.
66. Djuric, Z., et al., *A new approach to IR bimaterial detectors theory.* Infrared Physics & Technology, 2007. **50**: p. 51-57.
67. Corbeil, J.L., et al., *"Self-leveling" uncooled microcantilever thermal detector.* Applied Physics Letters, 2002. **81**(7): p. 1306-1308.
68. Callen, H.B. and R.F. Greene, *On a Theorem of Irreversible Thermodynamics.* Physical Review, 1952. **86**(5): p. 702-710.
69. Saulson, P.R., *Thermal noise in mechanical experiments.* Physical Review D, 1990. **42**(8): p. 2437-2445.
70. Cleland, A.N. and M.L. Roukes, *Noise processes in nanomechanical resonators.* Journal of Applied Physics, 2002. **92**(5): p. 2758-2769.
71. Zener, C., *Internal Friction in Solids. I. Theory of Internal Friction in Reeds.* Physical Review, 1937. **52**(3): p. 230-235.
72. Zener, C., *Elasticity and Anelasticity of Metals*. 1948, Chicago, IL: The University of Chicago Press.
73. Zener, C., W. Otis, and R. Nuckolls, *Internal Friction in Solids III. Experimental Demonstration of Thermoelastic Internal Friction.* Physical Review, 1938. **53**(1): p. 100-101.
74. Braginsky, V.B., *Systems with Small Dissipation*, ed. K.S. Thorne and C. Eller. 1985, Chicago, IL: The University of Chicago Press.
75. Lifshitz, R. and M.L. Roukes, *Thermoelastic damping in micro- and nanomechanical systems.* Physical Review B, 2000. **61**(8): p. 5600-5609.
76. Yasumura, K.Y., et al., *Quality factors in micron-and submicron-thick cantilevers.* Microelectromechanical Systems, Journal of, 2000. **9**(1): p. 117-125.

77. Houston, B.H., et al., *Thermoelastic loss in microscale oscillators.* Applied Physics Letters, 2002. **80**(7): p. 1300.
78. White Jr, B.E. and R.O. Pohl, *Internal Friction of Subnanometer a-SiO2 Films.* Physical Review Letters, 1995. **75**(24): p. 4437-4439.
79. Majorana, E. and Y. Ogawa, *Mechanical thermal noise in coupled oscillators.* Physics Letters A, 1997. **233**(3): p. 162-168.
80. Djuric, Z., *Mechanisms of noise sources in microelectromechanical systems.* Microelectronics Reliability, 2000. **40**(6): p. 919-932.
81. Kajima, M., et al., *Wide-band measurement of mechanical thermal noise using a laser interferometer.* Physics Letters A, 1999. **264**(4): p. 251-256.
82. Savran, C.A., et al., *Fabrication and Characterization of a Micromechanical Sensor for Differential Detection of Nanoscale Motions.* JOURNAL OF MICROELECTROMECHANICAL SYSTEMS, 2002. **11**(6): p. 703.
83. Harley, J.A. and T.W. Kenny, *Noise Considerations for the Design and Process Optimization of Piezoresistive Cantilevers.* JOURNAL OF MICROELECTROMECHANICAL SYSTEMS, 2000. **9**(2).
84. Hooge, F.N. and L.K.J. Vandamme, *Lattice scattering causes 1/f; noise.* Physics Letters A, 1978. **66**(4): p. 315-316.
85. Hansen, O. and A. Boisen, *Noise in piezoresistive atomic force microscopy.* Nanotechnology, 1999. **10**(1): p. 51-60.
86. Wu, J., G.K. Fedder, and L.R. Carley, *A low-noise low-offset capacitive sensing amplifier for a 50-μg/Hz-1/2 monolithic CMOS MEMS accelerometer.* Solid-State Circuits, IEEE Journal of, 2004. **39**(5): p. 722-730.
87. Palik, E.D., *Handbook of optical constants of solids*. 1985: Academic Press Orlando.
88. Ziegler, H. and J. Tiesmeyer, *Digital sensor for IR radiation.* Sensors and Actuators, 1983. **4**: p. 363-367.
89. Dong, F., et al., *An uncooled optically readable infrared imaging detector.* Sensors and Actuators A: Physical, 2007. **133**(1): p. 236-242.
90. Howard, P.E., et al., *DRS U6000 640x480 VOx uncooled IR focal plane.* Proceedings of SPIE: Infrared Detectors and Focal Plane Arrays VII, 2002. **4721**: p. 48-55.
91. Senesac, L.R., et al., *IR imaging using uncooled microcantilever detectors.* Ultramicroscopy, 2003. **97**: p. 451–458.
92. Wolfe, W.L. and G.J. Zissis, *The infrared handbook.* Arlington: Office of Naval Research, Department of the Navy, 1985, edited by Wolfe, William L.; Zissis, George J., 1985.
93. Senesac, L.R., et al., *IR imaging using uncooled microcantilever detectors.* Ultramicroscopy, 2003. **97**(1-4): p. 451-458.
94. Tipple, C.A., et al., *Nanostructured Microcantilevers with Functionalized Cyclodextrin Receptor Phases: Self-Assembled Monolayers and Vapor-Deposited Films.* Microelectron. Eng, 1999. **46**: p. 439-442.
95. Lavrik, N.V., *Femtogram mass detection using photothermally actuated nanomechanical resonators.* Applied Physics Letters, 2003. **82**(16): p. 2697.

96. Blech, I. and U. Cohen, *Effects of humidity on stress in thin silicon dioxide films.* Journal of Applied Physics, 1982. **53**: p. 4202.
97. Popova, A., et al., *AC and DC study of the temperature effect on mild steel corrosion in acid media in the presence of benzimidazole derivatives.* Corrosion Science, 2003. **45**(1): p. 33-58.
98. Eriksson, P., J.Y. Andersson, and G. Stemme, *Thermal characterization of surface-micromachined silicon nitridemembranes for thermal infrared detectors.* Microelectromechanical Systems, Journal of, 1997. **6**(1): p. 55-61.
99. Lecaruyer, P., et al., *Generalization of the Rouard method to an absorbing thin-film stack and application to surface plasmon resonance.* Applied Optics, 2006. **45**(33): p. 8419-8423.
100. Dong, L., R. Yue, and L. Liu, *Fabrication and Characterization of Integrated Uncooled Infrared Sensor Arrays Using a-Si Thin-Film Transistors as Active Elements.* Microelectromechanical Systems, Journal of, 2005. **14**(5): p. 1167-1177.
101. Huang, S. and X. Zhang, *Extension of the Stoney formula for film–substrate systems with gradient stress for MEMS applications.* J. Micromech. Microeng, 2006. **16**: p. 382-389.
102. Lavrik, N., et al., *Uncooled MEMS IR imagers with optical readout and image processing.* Proceedings of SPIE, 2007. **6542**: p. 65421E.

Appendix

Appendix

Calculation of Δz for Multifold Infrared Detectors

Figure 73 shows the deflection of a cantilever and associated angles. It is possible to do since the original Timoshenko equation [reference], from which Equation 12 has been derived, relates the radius of curvature with temperature increase

From Figure 73, we can see the following is true:

$$\alpha + \gamma = 90°$$
$$\beta + 2\gamma = 180°$$

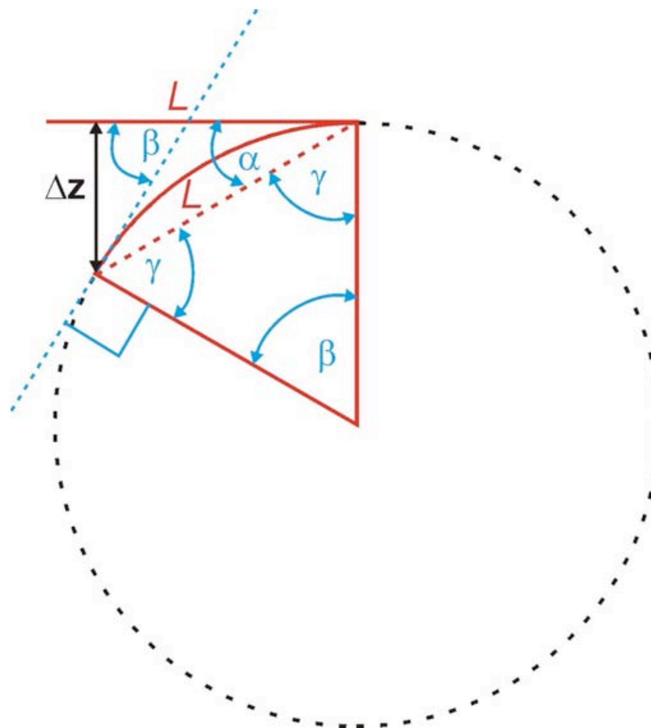

Figure 73 Angles associated with bimaterial cantilever deformations

Multiplying the first equation by 2 we and subtracting it from the second one we obtain

$$\beta - 2\alpha = 0°$$

or

$$\beta = 2\alpha$$

It can also be seen that for small angles of α, i.e. large radiuses of curvature, the dashed red line in Figure 73 would coincide with the deformed cantilever (curved red line) and we would have:

$$\sin\alpha \approx \alpha \approx \frac{\Delta z}{L}$$

We can verify that this is correct assumption based on the fact that for 1 K DT, we have measured and predicted deflections Δz of several hundred nm.

For the specific geometry discussed in this dissertation, in case of temperature increase, the bimaterial regions will deform. Figure 74 shows the angles of interest in further calculations.

Applying the expression obtained in above, i.e. $\theta = 2\frac{\Delta z_1}{L}$

$$\Delta z \approx \Delta z_1 + \Delta z_2 \cos\left(\frac{2\Delta z_1}{L}\right)$$

And since in our case, we deal with very small angles, $\cos\left(\frac{2\Delta z_1}{L}\right) \approx 1$, we can write:

$$\Delta z \approx \Delta z_1 + \Delta z_2$$

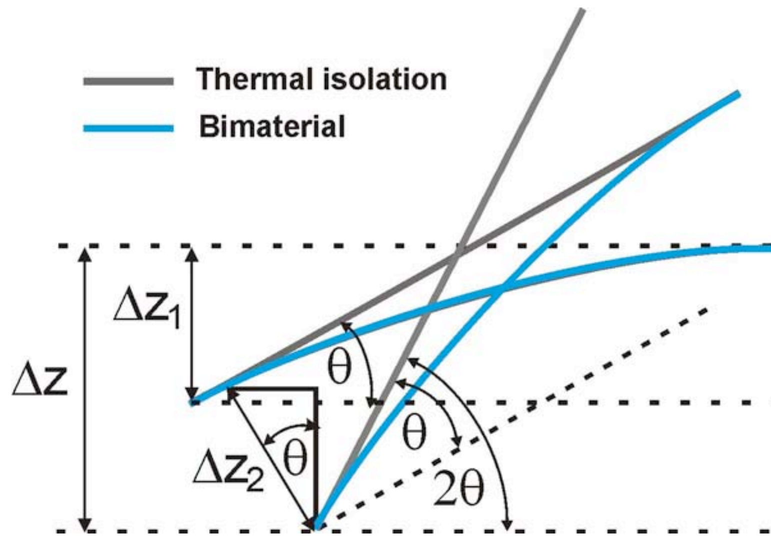

Figure 74 Deformation angles for multifold structure
Blue regions represent the deformable bimaterial regions whereas gray ones represent thermal isolation and absorber regions

In case temperature increase in both bimaterial regions is the same, the individual dip displacements from the plane will be equal

$$\Delta z_1 = \Delta z_2$$

and hence,

$$\Delta z \approx 2\Delta z_1$$

Vita

Dragoslav Grbovic was born in Belgrade, Serbia, on January 4, 1979. He attended the Petar Kočić elementary in Zemun, Serbia and Electrical Engineering high school Nikola Tesla in Belgrade. After two years at Electrical Engineering at the University of Belgrade, he transferred to Ramapo College of New Jersey as a recipient of merit-based Presidential Scholarship. He obtained a Bachelor's Degree in physics graduating with honors in 3.5 years and receiving the Outstanding Student Award. He is also a recipient of the Outstanding Student Service Award presented for active participation in college life and extracurricular activities. During his undergraduate studies he actively participated in research projects at Ramapo as well as in two summer research internships programs of University of Tennessee and worked on projects at Oak Ridge National Laboratory. He subsequently joined the group he worked with to continue his studies and pursue a graduate degeree. He enrolled into a Ph.D. program at Department of Physics and Astronomy at University of Tennessee in January of 2003. As a teaching assistant, he received the Robert W. Lide Citation for outstanding laboratory services. As a research assistant, he worked under direction of Dr. Panos Datskos at Oak Ridge National Laboratory. His main research interest was micro-electromechanical systems (MEMS) and he is a co-author of six publications in journals and conference proceedings. He obtained a M.S. degree in December of 2006. He obtained a Ph.D. degree in May of 2008. His Ph.D. committee consisted of Dr. Panos Datskos, Dr. Hanno Weitering, Dr. Adriana Moreo, Dr. Adolfo Eguiluz and Dr. Michael Sepaniak.